The Astrophysical Journal Supplement Series, 170:288–334, 2007 June

THREE-YEAR *WILKINSON MICROWAVE ANISOTROPY PROBE* (*WMAP*[1]) OBSERVATIONS: TEMPERATURE ANALYSIS

G. Hinshaw,[2] M. R. Nolta,[3] C. L. Bennett,[4] R. Bean,[5] O. Doré,[3,6] M. R. Greason,[7] M. Halpern,[8] R. S. Hill,[7] N. Jarosik,[9] A. Kogut,[2] E. Komatsu,[10] M. Limon,[7] N. Odegard,[7] S. S. Meyer,[11] L. Page,[9] H. V. Peiris,[11,12] D. N. Spergel,[6] G. S. Tucker,[13] L. Verde,[14] J. L. Weiland,[7] E. Wollack,[2] and E. L. Wright[15]
Received 2006 March 16; accepted 2006 November 30

ABSTRACT

We present new full-sky temperature maps in five frequency bands from 23 to 94 GHz, based on data from the first 3 years of the *WMAP* sky survey. The new maps are consistent with the first-year maps and are more sensitive. The 3 year maps incorporate several improvements in data processing made possible by the additional years of data and by a more complete analysis of the polarization signal. These include several new consistency tests as well as refinements in the gain calibration and beam response models. We employ two forms of multifrequency analysis to separate astrophysical foreground signals from the CMB, each of which improves on our first-year analyses. First, we form an improved "Internal Linear Combination" (ILC) map, based solely on *WMAP* data, by adding a bias-correction step and by quantifying residual uncertainties in the resulting map. Second, we fit and subtract new spatial templates that trace Galactic emission; in particular, we now use low-frequency *WMAP* data to trace synchrotron emission instead of the 408 MHz sky survey. The *WMAP* point source catalog is updated to include 115 new sources whose detection is made possible by the improved sky map sensitivity. We derive the angular power spectrum of the temperature anisotropy using a hybrid approach that combines a maximum likelihood estimate at low l (large angular scales) with a quadratic cross-power estimate for $l > 30$. The resulting multifrequency spectra are analyzed for residual point source contamination. At 94 GHz the unmasked sources contribute $128 \pm 27\ \mu\mathrm{K}^2$ to $l(l+1)C_l/2\pi$ at $l = 1000$. After subtracting this contribution, our best estimate of the CMB power spectrum is derived by averaging cross-power spectra from 153 statistically independent channel pairs. The combined spectrum is cosmic variance limited to $l = 400$, and the signal-to-noise ratio per l-mode exceeds unity up to $l = 850$. For bins of width $\Delta l/l = 3\%$, the signal-to-noise ratio exceeds unity up to $l = 1000$. The first two acoustic peaks are seen at $l = 220.8 \pm 0.7$ and $l = 530.9 \pm 3.8$, respectively, while the first two troughs are seen at $l = 412.4 \pm 1.9$ and $l = 675.2 \pm 11.1$. The rise to the third peak is unambiguous; when the *WMAP* data are combined with higher resolution CMB measurements, the existence of a third acoustic peak is well established. Spergel et al. use the 3 year temperature and polarization data to constrain cosmological model parameters. A simple six-parameter ΛCDM model continues to fit CMB data and other measures of large-scale structure remarkably well. The new polarization data produce a better measurement of the optical depth to reionization, $\tau = 0.089 \pm 0.03$. This new and tighter constraint on τ helps break a degeneracy with the scalar spectral index, which is now found to be $n_s = 0.960 \pm 0.016$. If additional cosmological data sets are included in the analysis, the spectral index is found to be $n_s = 0.947 \pm 0.015$.

Subject headings: cosmic microwave background — cosmology: observations — dark matter — early universe — instrumentation: detectors — space vehicles: instruments — telescopes

Online material: machine-readable table

1. INTRODUCTION

The *Wilkinson Microwave Anisotropy Probe* (*WMAP*) is a Medium-class Explorer (MIDEX) mission designed to elucidate cosmology by producing full-sky maps of the cosmic microwave background (CMB) anisotropy. Results from the first year of *WMAP* observations were reported in a suite of papers published in the *Astrophysical Journal Supplement Series* in September 2003 (Bennett et al. 2003a, 2003b, 2003c; Jarosik et al. 2003a, 2003b; Page et al. 2003a, 2003b, 2003c; Barnes et al. 2002, 2003; Hinshaw et al. 2003a, 2003b; Komatsu et al. 2003; Kogut et al. 2003; Spergel et al. 2003; Verde et al. 2003; Peiris et al. 2003; Nolta et al. 2004). The data were made available to the research community via the Legacy Archive for Microwave Background Data Analysis (LAMBDA), NASA's CMB Thematic Data Center, and were described in detail in the *WMAP* Explanatory Supplement (Limon et al. 2003).

[1] *WMAP* is the result of a partnership between Princeton University and the NASA Goddard Space Flight Center. Scientific guidance is provided by the *WMAP* Science Team.

[2] Code 665, NASA Goddard Space Flight Center, Greenbelt, MD 20771; Gary.F.Hinshaw@nasa.gov.
[3] Canadian Institute for Theoretical Astrophysics, University of Toronto, ON M5S 3H8, Canada.
[4] Department of Physics and Astronomy, The Johns Hopkins University, Baltimore, MD 21218-2686.
[5] Cornell University, Ithaca, NY 14853.
[6] Department of Astrophysical Sciences, Princeton University, Princeton, NJ 08544-1001.
[7] Science Systems and Applications, Inc. (SSAI), Lanham, MD 20706.
[8] Department of Physics and Astronomy, University of British Columbia, Vancouver, BC V6T 1Z1, Canada.
[9] Department of Physics, Princeton University, Princeton, NJ 08544-0708.
[10] Department of Astronomy, University of Texas, Austin, TX 78712.
[11] Departments of Astrophysics and Physics, University of Chicago, Chicago, IL 60637.
[12] Hubble Fellow.
[13] Department of Physics, Brown University, Providence, RI 02912-1843.
[14] Department of Physics and Astronomy, University of Pennsylvania, Philadelphia, PA 19104.
[15] UCLA Astronomy, Los Angeles, CA 90095-1562.

Papers based on the first-year *WMAP* results cover a wide range of topics, including constraints on inflation, the nature of the dark energy, the dark matter density, implications for supersymmetry, the CMB and *WMAP* as the premier baryometer, intriguing features in the large-scale data, the topology of the universe, deviations from Gaussian statistics, time-variable cosmic parameters, the Galactic interstellar medium, microwave point sources, the Sunyaev-Zeldovich effect, and the ionization history of the universe. The *WMAP* data have also been used to establish the calibration of other CMB data sets.

Our analysis of the first 3 years of *WMAP* data is now complete, and the results are presented here and in three companion papers (Jarosik et al. 2007; Page et al. 2007; Spergel et al. 2007). The 3 year *WMAP* results improve on the first-year set in many ways, the most important of which are the following. (1) A thorough analysis of the polarization data has produced full-sky polarization maps and power spectra, and an improved understanding of many aspects of the data. (2) Additional data reduce the instrument noise, producing power spectra that are 3 times more sensitive in the noise-limited regime. (3) Independent years of data enable cross-checks that were not previously possible. (4) The instrument calibration and beam response have been better characterized.

This paper presents the analysis of the 3 year temperature data, focusing on foreground modeling and removal, evaluation of the angular power spectrum, and selected topics beyond the power spectrum. Companion papers present the new polarization maps and polarization-specific scientific results (Page et al. 2007), and discuss the cosmological implications of the 3 year *WMAP* data (Spergel et al. 2007). Jarosik et al. (2007) present our new data-processing methods and place systematic error limits on the maps.

In § 2 we summarize the major changes we have made to the data processing since the first-year analysis, and § 3 presents a synopsis of the 3 year temperature maps. In § 4 we discuss Galactic foreground emission and our attempts to separate the emission components using a maximum entropy method (MEM) analysis. Section 5 illustrates two methods we employ to remove Galactic foreground emission from the maps in preparation for CMB analysis. Section 6 updates the *WMAP* point-source catalog and presents a search for the Sunyaev-Zeldovich effect in the 3 year maps. Section 7 evaluates the angular power spectrum and compares it to the previous *WMAP* spectrum and to other contemporary CMB results. In § 8 we survey the claims that have been made regarding odd features in the *WMAP* first-year sky maps, and we offer conclusions in § 9.

2. CHANGES IN THE 3 YEAR DATA ANALYSIS

The first-year data analysis was described in detail in the suite of first-year *WMAP* papers listed above. In large part, the 3 year analysis employs the same methods, with the following exceptions.

In the first-year analysis we subtracted the *COBE* dipole from the time-ordered data to minimize the effect of signal aliasing that arises from pixelizing a signal with a steep gradient. Since the *WMAP* gain-calibration procedure uses the Doppler effect induced by *WMAP*'s velocity with respect to the Sun to establish the absolute calibration scale, *WMAP* data may be used independently to determine the CMB dipole. Consequently, we subtract the *WMAP* first-year dipole (Bennett et al. 2003b) from the time-ordered data in the present analysis.

A small temperature-dependent pointing error ($\sim 1'$) was found during the course of the first-year analysis. The effect is caused by thermal stresses on the spacecraft structure that induce slight movement of the star tracker with respect to the instrument. While the error was small enough to ignore in the first-year data, it is now corrected with a temperature-dependent model of the relative motion (Jarosik et al. 2007).

The radiometer gain model described by Jarosik et al. (2003b) has been updated to include a dependence on the temperature of the warm-stage (RXB) amplifiers. While this term was not required by the first-year data, it is required now for the model to fit the full 3 year data with a single parameterization. The new model, and its residual errors, are discussed by Jarosik et al. (2007).

The *WMAP* beam response has now been measured with six independent "seasons" of Jupiter observations. In addition, we have now produced a physical model of one side of our symmetric optical system, the A-side, based on simultaneous fits to all 10 A-side beam pattern measurements (Jarosik et al. 2007). We use this model to augment the beam-response data at very low signal-to-noise ratio (S/N), which in turn allows us to better determine the total solid angle and window function of each beam.

The far-sidelobe response of the beam was determined from a combination of ground measurements and in-flight lunar data taken early in the mission (Barnes et al. 2003). In the first-year processing we applied a small far-sidelobe correction to the *K*-band sky map. For the current analysis, we have implemented a new far-sidelobe correction and gain recalibration that operates on the time-ordered data (Jarosik et al. 2007). These corrections have now been applied to data from all 10 differencing assemblies.

When producing polarization maps, we account for differences in the frequency passband between the two linear polarization channels in a differencing assembly (Page et al. 2007). If this difference is not accounted for, Galactic foreground signals would alias into linear polarization signals.

Due to a combination of $1/f$ noise and observing strategy, the noise in the *WMAP* sky maps is correlated from pixel to pixel. This results in certain low-l modes on the sky being less well measured than others. This effect can be completely ignored for temperature analysis, since the low-l S/N is so high, and the effect is not important at high-l (§ 7.1.2). However, it is very important for polarization analysis because the S/N is so much lower. In order to handle this complexity, the map-making procedure has been overhauled to produce genuine maximum likelihood solutions that employ optimal filtering of the time-ordered data and a conjugate-gradient algorithm to solve the linear map-making equations (Jarosik et al. 2007). In conjunction with this we have written code to evaluate the full pixel-to-pixel weight (inverse covariance) matrix at low pixel resolution. (The HEALPix convention is to denote pixel resolution by the parameter $N_{\rm side}$, with $N_{\rm pix} = 12N_{\rm side}^2$ (Gorski et al. 2005). We define a resolution parameter r such that $N_{\rm side} = 2^r$. The weight matrices have been evaluated at resolution r4, $N_{\rm side} = 16$, $N_{\rm pix} = 3072$. The full noise covariance information is propagated through the power spectrum analysis (Page et al. 2007).

When performing template-based Galactic foreground subtraction, we now use templates based on *WMAP* K- and Ka-band data in place of the 408 MHz synchrotron map (Haslam et al. 1981). As discussed in § 5.3, this substitution reduces errors caused by spectral index variations that change the spatial morphology of the synchrotron emission as a function of frequency. A similar model is used for subtracting polarized synchrotron emission from the polarization maps (Page et al. 2007).

We have performed an error analysis of the internal linear combination (ILC) map and have now implemented a bias correction as part of the algorithm. We believe that the map is now suitable for use in low-l CMB signal characterization, although we have not performed a full battery of non-Gaussian tests on this

TABLE 1
Data Flagging Summary

Category	K Band	Ka Band	Q Band	V Band	W Band
Lost or rejected data:					
Lost[a] (%)	0.43	0.43	0.43	0.43	0.43
Thermal disturbance[b] (%)	0.51	0.51	0.51	0.51	0.51
Gain/baseline step (%)	0.02	0.04	0.05	0.00	0.06
Total lost or rejected (%)	0.96	0.98	0.99	0.94	1.00
Data not used in maps:					
Planet in beam (%)	0.11	0.11	0.11	0.11	0.11

[a] Primarily due to one solar storm induced safehold.
[b] Primarily due to station-keeping maneuvers at L2.

map, so we must still advise users to exercise caution. Accordingly, we present full-sky multipole moments for $l = 2$ and 3, derived from the 3 year ILC map.

We have improved the final temperature power spectrum (C_l^{TT}) by using a maximum likelihood estimate for low-l and a pseudo-C_l estimate for $l > 30$ (see § 7). The pseudo-C_l estimate is simplified by using only V- and W-band data, and by reducing the number of pixel weighting schemes to two, "uniform" and "$N_{\rm obs}$" (§ 7.5). With three individual years of data and six V- and W-band differencing assemblies (DAs) to choose from, we can now form individual cross-power spectra from 15 DA pairs within a year and from 36 DA pairs across 3 year pairs, for a total of 153 independent cross-power spectra. In the first-year spectrum we included Q-band data, which gave us 8 DAs and 28 independent cross-power spectra. The arguments for dropping Q-band from the 3 year spectrum are given in § 7.2.

We have developed methods for estimating the polarization power spectra (C_l^{XX} for XX = TE, TB, EE, EB, BB) from temperature

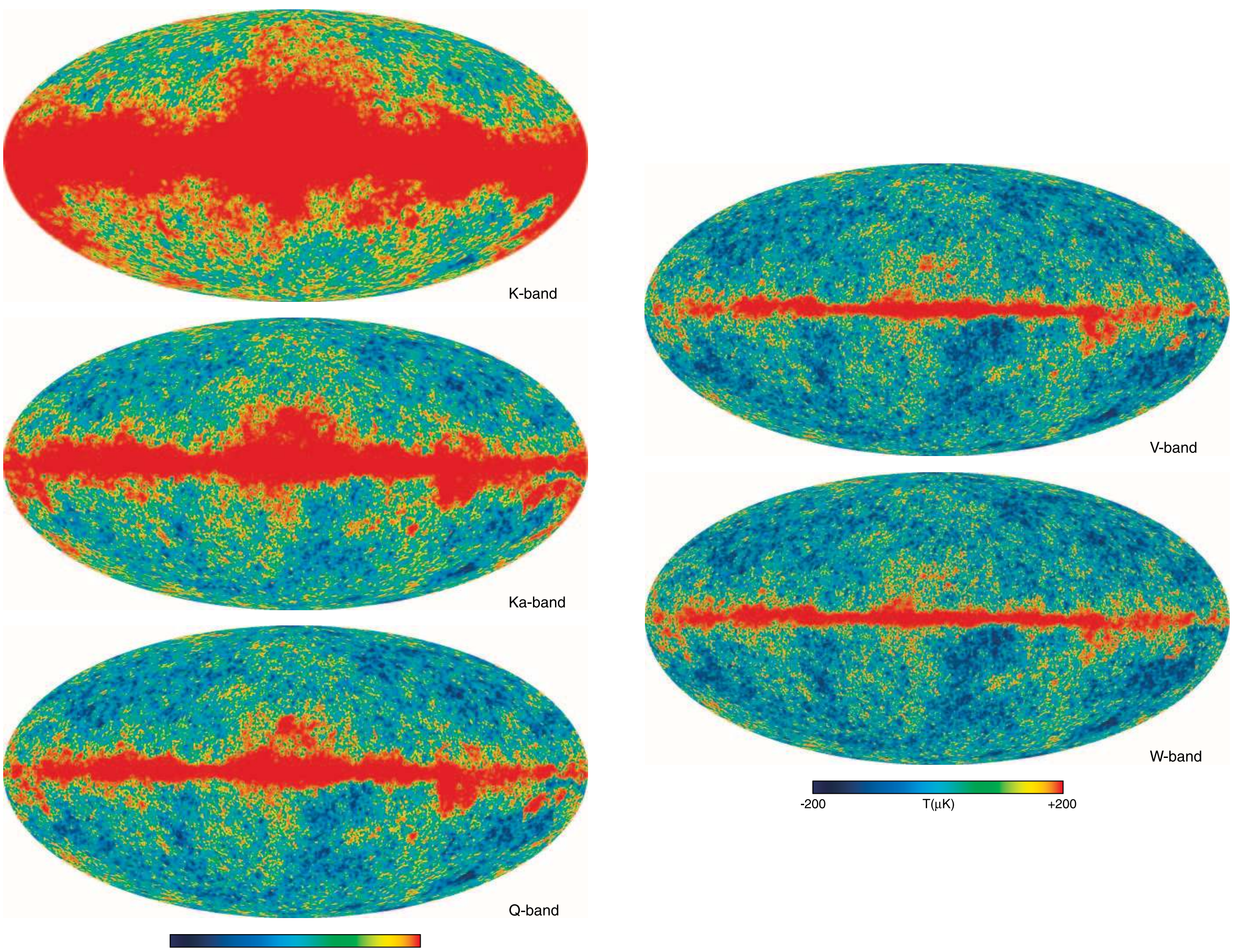

Fig. 1.—Full-sky maps in Galactic coordinates smoothed with a 0.2° Gaussian beam, shown in Mollweide projection. *Top left*: K band (23 GHz); *middle left*: Ka band (33 GHz); *bottom left*: Q band (41 GHz); *top right*: V band (61 GHz); *bottom right*: W band (94 GHz).

and polarization maps. The main technical hurdle we had to overcome in the process was the proper handling of low-S/N data with complex noise properties (Page et al. 2007). This step, in conjunction with the development of the new map-making process, was by far the most time-consuming aspect of the 3 year analysis.

We have improved the form of the likelihood function used to infer cosmological parameters from the Monte Carlo Markov Chains (Spergel et al. 2007). In addition to using an exact maximum likelihood form for the low-l TT data, we have developed a method to self-consistently evaluate the joint likelihood of temperature and polarization data given a theoretical model (described in Appendix D of Page et al. 2007). We also now account for Sunyaev-Zeldovich (SZ) fluctuations when estimating parameters. Within the *WMAP* frequency range, it is difficult to distinguish between a primordial CMB spectrum and a thermal SZ spectrum, so we adopt the Komatsu & Seljak (2002) model for the SZ power spectrum and marginalize over the amplitude as a nuisance parameter.

We now use the CAMB code (Lewis et al. 2000) to compute angular power spectra from cosmological parameters. CAMB is derived from CMBFAST (Seljak & Zaldarriaga 1996), but it runs faster on our Silicon Graphics (SGI) computers.

3. OBSERVATIONS AND MAPS

The 3 year *WMAP* data encompass the period from 00:00:00 UT, 2001 August 10 (day 222) to 00:00:00 UT, 2004 August 9 (day 222). The observing efficiency during this time is roughly 99%; Table 1 lists the fraction of data that was lost or flagged as suspect. The table also gives the fraction of data that is flagged due to potential contamination by thermal emission from Mars, Jupiter, Saturn, Uranus, and Neptune. These data are not used in map-making, but are useful for in-flight beam mapping (Limon et al. 2006).

Sky maps are created from the time-ordered data using the procedure described by Jarosik et al. (2007). For several reasons, we produce single-year maps for each year of the 3 year observing period (after performing an end-to-end analysis of the instrument calibration). We produce 3 year maps by averaging the annual maps. Figure 1 shows the 3 year maps at each of the five *WMAP* observing frequencies: 23, 33, 41, 61, and 94 GHz. The number of independent observations per pixel, $N_{\rm obs}$, is displayed in Figure 2. The noise per pixel, p, is given by $\sigma(p) = \sigma_0 N_{\rm obs}^{-1/2}(p)$, where σ_0 is the noise per observation, given in Table 2. To a very good approximation, the noise per pixel in the 3 year maps is a factor of $\sqrt{3}$ times lower than in the 1 year maps. The noise properties of the data are discussed in more detail in Jarosik et al. (2007).

The 3 year maps are compared to the previously released maps in Figure 3. Both set of maps have been smoothed to 1° resolution to minimize the noise difference between them. When viewed side by side they look indistinguishable. The right column of Figure 3 shows the difference of the maps at each frequency on a scale of ± 30 μK. Aside from the noise reduction and a few bright variable quasars, such as 3C 279, the main difference between the maps is in the large-scale (low-l) emission. This is largely due to improvements in our model of the instrument gain as a function of time, which is made possible by having a longer time span with which to fit the model (Jarosik et al. 2007). In the specific case of the K band, the improved far-sidelobe pickup correction produced an effective change in the absolute calibration scale by $\sim$1%. This in turn is responsible for the difference seen in the bright Galactic plane signal in the K band (Jarosik et al. 2007).

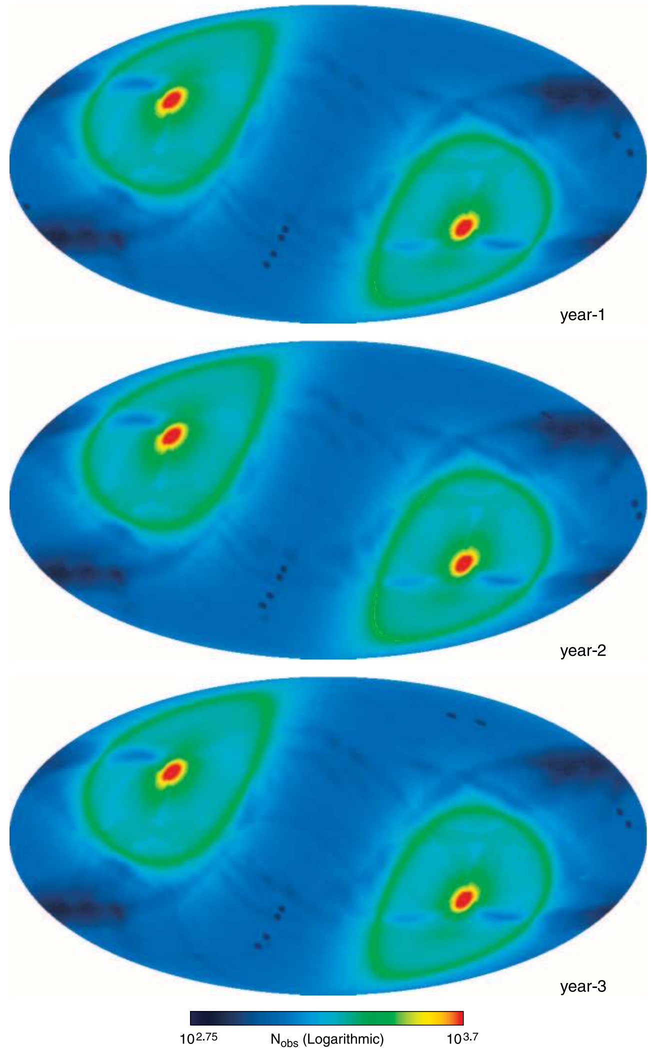

Fig. 2.—Number of independent W-band observations per pixel in Galactic coordinates for year 1 (*top*), year 2 (*middle*), and year 3 (*bottom*). The number of observations is greatest near the ecliptic poles and in rings approximately 141° from each pole (determined by the angular separation between the two boresight directions). The number of observations is least in the ecliptic plane. The small circular cuts in the ecliptic are where Mars, Saturn, Jupiter, Uranus, and Neptune are masked so as not to contaminate the CMB signal. The coverage is quite consistent from year to year, with the planet cuts being responsible for the largest fractional variation.

We discuss the low-l emission in detail in § 7.4 and § 8, but we stress here that the changes shown in Figure 3 are small, even compared to the low quadrupole moment seen in the first-year maps. Table 3 gives the amplitude of the dipole, quadrupole, and octopole moments in these difference maps. For comparison, we estimate the CMB power at $l = 2$ and 3 to be $\Delta T_l^2 = 236$ and 1053 μK^2, respectively (§ 7.4).

As discussed in § 8, several authors have noted unusual features in the large-scale signal recorded in the first-year maps. We have not attempted to reproduce the analyses presented in those papers, but based on the small fractional difference in the large-scale signal, we anticipate that most of the previously reported results will persist when the 3 year maps are analyzed.

4. GALACTIC FOREGROUND ANALYSIS

The CMB signal in the *WMAP* sky maps is contaminated by microwave emission from the Milky Way and from extragalactic

TABLE 2
Differencing Assembly (DA) Properties

DA	λ[a] (mm)	ν[a] (GHz)	$g(\nu)$[b]	$\theta_{\rm FWHM}$[c] (deg)	$\sigma_0(I)$[d]	$\sigma_0(Q, U)$[d] (mK)	ν_s[e] (GHz)	$\nu_{\rm ff}$[e] (GHz)	ν_d[e] (GHz)
K1	13.17	22.77	1.0135	0.807	1.439	1.455	22.47	22.52	22.78
Ka1	9.079	33.02	1.0285	0.624	1.464	1.483	32.71	32.76	33.02
Q1	7.342	40.83	1.0440	0.480	2.245	2.269	40.47	40.53	40.85
Q2	7.382	40.61	1.0435	0.475	2.135	2.156	40.27	40.32	40.62
V1	4.974	60.27	1.0980	0.324	3.304	3.330	59.65	59.74	60.29
V2	4.895	61.24	1.1010	0.328	2.946	2.970	60.60	60.70	61.27
W1	3.207	93.49	1.2480	0.213	5.883	5.918	92.68	92.82	93.59
W2	3.191	93.96	1.2505	0.196	6.532	6.571	93.34	93.44	94.03
W3	3.226	92.92	1.2445	0.196	6.885	6.925	92.34	92.44	92.98
W4	3.197	93.76	1.2495	0.210	6.744	6.780	93.04	93.17	93.84

[a] Effective wavelength and frequency for a thermodynamic spectrum.
[b] Conversion from antenna temperature to CMB thermodynamic temperature; $\Delta T = g(\nu)\Delta T_A$, $g(\nu) = [(e^x - 1)^2/x^2 e^x]$, $x = h\nu/kT_0$, $T_0 = 2.725$ K (Mather et al. 1999).
[c] Full width at half-maximum (FWHM) from radial profile of A- and B-side average beams. Note that the beams are not Gaussian.
[d] Noise per observation for resolution 9 and 10 I, Q, and U maps, to $\sim$0.1% uncertainty; $\sigma(p) = \sigma_0 N_{\rm obs}^{-1/2}(p)$.
[e] Effective frequency for synchrotron (s), free-free (ff), and dust (d) emission, assuming spectral indices of $\beta = -2.9$, -2.1, and +2.0, respectively, in antenna temperature units.

sources. In order to use the maps reliably for cosmological studies, the foreground signals must be understood and removed from the maps. In this section we present an overview of the mechanisms that produce significant diffuse microwave emission in the Milky Way, and we assess what can be learned about them using a maximum entropy method (MEM) analysis of the *WMAP* data. We discuss foreground removal in § 5.

4.1. *Free-Free Emission*

Free-free emission arises from electron-ion scattering which produces microwaves with a brightness spectrum $T_A \sim (\mathrm{EM}/1\ \mathrm{cm^{-6}\ pc})\nu^{-2.14}$ for frequencies $\nu > 10$ GHz, where EM is the emission measure, $\int n_e^2\,dl$, and we assume an electron gas temperature $T_e \sim 8000$ K. As discussed in Bennett et al. (2003c), high-resolution maps of Hα emission (Dennison et al. 1998; Haffner et al. 2003; Reynolds et al. 2002; Gaustad et al. 2001) can serve as approximate tracers of free-free emission. The intensity of Hα emission is given by

$$I(\mathrm{R}) = 0.44\xi(\tau_d)\left(\frac{\mathrm{EM}}{1\ \mathrm{cm^{-6}\ pc}}\right)\left(\frac{T_e}{8000\ \mathrm{K}}\right)^{-0.5} \times \left[1 - 0.34\ln\left(\frac{T_e}{8000\ \mathrm{K}}\right)\right], \qquad (1)$$

where I is in Rayleighs ($1\ \mathrm{R} = 2.42 \times 10^{-7}$ ergs cm^{-2} s^{-1} sr^{-1} at the Hα wavelength of 0.6563 μm), the helium contribution is assumed to be small, and $\xi(\tau_d)$ is an extinction factor that depends on the dust optical depth, τ_d, at the wavelength of Hα. If the emitting gas is coextensive with dust, then $\xi(\tau_d) = [1 - \exp(-\tau_d)]/\tau_d$. H$\alpha$ is in the R band, where the extinction is 0.75 times visible, $A_R = 0.75A_V$; thus, $A_R = 2.35E_{B-V}$, and $\tau_d = 2.2E_{B-V}$. Finkbeiner (2003) assembled a full-sky Hα map using data from several surveys: the Wisconsin H-Alpha Mapper (WHAM), the Virginia Tech Spectral-Line Survey (VTSS), and the Southern H-Alpha Sky Survey Atlas (SHASSA). We use this map, together with the Schlegel et al. (1998; SFD) extinction map, to predict a map of free-free emission in regions where $\tau_d < 1$, under the assumption that the dust and ionized gas are coextensive. As discussed in Bennett et al. (2003c) this template has known sources of uncertainty and error. We use it as a prior estimate in the MEM analysis (§ 4.5), and as a free-free estimate in the template-based foreground removal (§ 5.3).

4.2. *Synchrotron Emission*

Synchrotron emission arises from the acceleration of cosmic ray electrons in magnetic fields. In our Galaxy, discrete supernova remnants contribute only $\sim$10% of the total synchrotron emission at 1.5 GHz (Lisenfeld & Völk 2000; Biermann 1976; Ulvestad 1982), while $\sim$90% of the observed emission arises from a diffuse component. Hummel et al. (1991) present maps of synchrotron emission at 610 MHz and 1.49 GHz from the edge-on spiral galaxy NGC 891. They find that the synchrotron spectral index varies from $\beta_s \approx -2.6$ in most of the galactic plane to $\beta_s \approx -3.1$ in the halo. Similar spectral index variations are seen in the Milky Way at $\sim$1 GHz, where the synchrotron signal is complex. Variations of the synchrotron spectral index are both expected and observed. Moreover, the emission is dominated at low frequencies by components with steep spectra, whereas at higher frequencies it is dominated by components with flatter spectra, usually with a different spatial distribution. As a result, great care must be taken when using low-frequency maps, such as the 408 MHz map of Haslam et al. (1981), as tracers of the synchrotron emission at microwave frequencies.

Synchrotron emission can be highly polarized. Theoretically, the linear polarization fraction can be as high as $\sim$75%, although values $\lesssim$30% are more typically observed. See Page et al. (2007) for a discussion of the new full-sky observations of polarized synchrotron emission in the 3 year *WMAP* data.

4.3. *Thermal Dust Emission*

Thermal dust emission has been mapped over the full sky in several infrared bands by the *IRAS* and *COBE* missions. Schlegel et al. (1998) combined data from both missions to produce an absolutely calibrated full-sky map of the thermal dust emission. Finkbeiner et al. (1999; hereafter FDS99) extended this work to far-infrared and microwave frequencies using the *COBE* FIRAS and DMR data to constrain the low-frequency dust spectrum. They fit the data to a particular two-component model that gives power-law emissivity indices $\alpha_1 = 1.67$ and $\alpha_2 = 2.70$, and temperatures

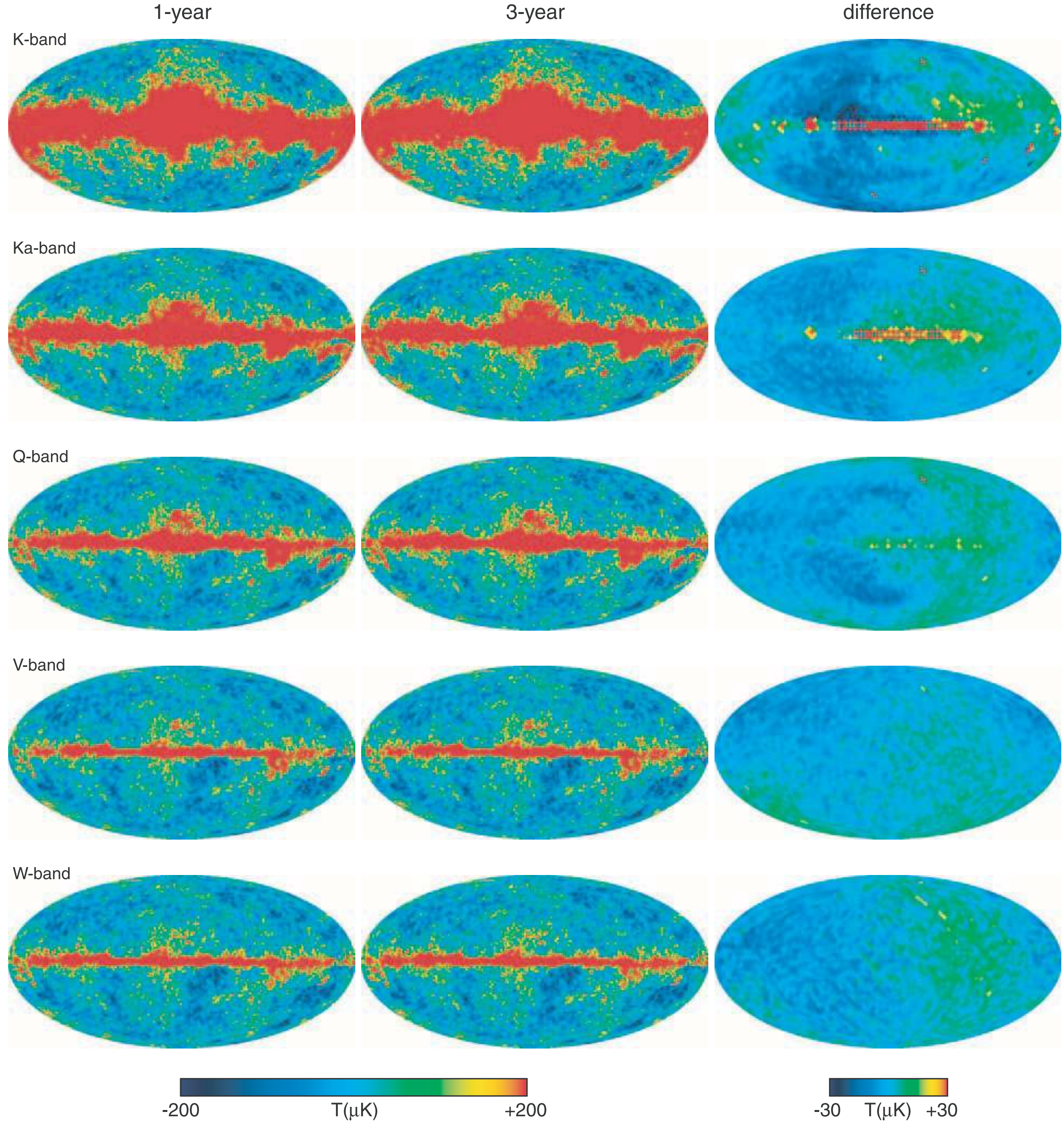

FIG. 3.—Comparison of the 3 year maps with the previously released 1 year maps. The data are smoothed to 1° resolution and are shown in Galactic coordinates. The frequency bands K through W are shown top to bottom. The first-year maps (*left*) and the 3 year maps (*middle*) are shown scaled to ± 200 μK. The difference maps (*right*) are degraded to pixel resolution 4 and scaled to ± 20 μK. The small difference in low-l power is mostly due to improvements in the gain model of the instrument as a function of time (Jarosik et al. 2007). See § 3 and Table 3.

of $T_1 = 9.4$ K and $T_2 = 16.2$ K. The fraction of power emitted by each component is $f_1 = 0.0363$ and $f_2 = 0.9637$, and the relative ratio of IR thermal emission to optical opacity of the two components is $q_1/q_2 = 13.0$. The cold component is potentially identified as emission from amorphous silicate grains, while the warm component is plausibly carbon based. Independent of the physical interpretation of the model, FDS99 found that it fit the data moderately well, with $\chi^2_\nu = 1.85$ for 118 degrees of freedom. Bennett et al. (2003a) noted that this model, called "Model 8" by FDS99, did well predicting the first-year *WMAP* dust emission.

It is reasonable to assume that the Milky Way is like other spiral galaxies and that the microwave properties of external galaxies should help to inform our understanding of the global properties of the Milky Way. It has long been known that a remarkably tight correlation exists between the broadband far-infrared and broadband synchrotron emission in external galaxies. This relation has been extensively studied and modeled (Dickey

TABLE 3
CHANGE IN LOW-l POWER

Band	$l = 1$[a] (μK)	$l = 2$[b] (μK^2)	$l = 3$[b] (μK^2)
K	10.1	38.8	9.1
Ka	7.3	2.7	3.4
Q	6.1	7.1	12.3
V	5.1	7.1	2.2
W	7.0	5.8	1.5

[a] $l = 1$: Amplitude in the difference map, in μK.
[b] $l > 1$: Power in the difference map, $l(l + 1)C_l/2\pi$, in μK^2.

& Salpeter 1984; de Jong et al. 1985; Helou et al. 1985; Sanders & Mirabel 1985; Gavazzi et al. 1986; Hummel 1986; Wunderlich et al. 1987; Wunderlich & Klein 1988, 1991; Beck & Golla 1988; Fitt et al. 1988; Hummel et al. 1988; Mirabel & Sanders 1988; Bicay et al. 1989; Devereux & Eales 1989; Unger et al. 1989; Voelk 1989; Chi & Wolfendale 1990; Condon 1992; Bressan et al. 2002). All theories attempting to explain this tight correlation are tied to the level of the star formation activity. During this cycle, stars form, heat, and destroy dust grains; create magnetic fields and relativistic electrons; and create the O- and B-stars that ionize the surrounding gas. However, it is not clear what these models predict on a "microscopic" (cloud by cloud) level within a galaxy.

Bennett et al. (2003c) showed that the synchrotron and dust emission in our own Galaxy are spatially correlated at *WMAP* frequencies. Many authors have argued that this correlation is actually due to radio emission from dust grains themselves, rather than from a tight dust-synchrotron correlation. We review the evidence for this more fully in the next section.

4.4. *"Anomalous" Microwave Emission from Dust?*

With the advent of high-quality diffuse microwave emission maps in the early 1990s, it became possible to study the high-frequency tail of the synchrotron spectrum and the low-frequency tail of the interstellar dust spectrum. Kogut et al. (1996a, 1996b) analyzed foreground emission in the *COBE* DMR maps and reported a signal that was significantly correlated with 240 μm dust emission (Arendt et al. 1998), but not with 408 MHz synchrotron emission (Haslam et al. 1981). The correlated signal was notably brighter at 31 GHz than at 53 GHz ($\beta \sim -2.2$); hence, they concluded that it was consistent with free-free emission that was spatially correlated with dust. The same conclusion was reached by de Oliveira-Costa et al. (1997), who found the Saskatoon 40 GHz data to be correlated with infrared dust, but not with radio synchrotron emission.

Leitch et al. (1997, 2000) and Leitch (1998) analyzed data from the "RING5m" experiment. A likelihood fit to their 14.5 GHz and 31.7 GHz data, assuming CMB anisotropy and a single foreground component, produced a foreground spectral index of $\beta = -2.58^{+0.53}_{-0.42}$. The data would have preferred a steeper value had it not been for an assumed prior limit of $\beta > -3$. This signal was fully consistent with synchrotron emission. However, a puzzle arose in comparing the RING5m data with a the Westerbork Northern Sky Survey (WENSS) (Rengelink et al. 1997) at 325 MHz: the WENSS data showed no detectable signal in the vicinity of the RING5m field. The 325 MHz limit implies that $\beta > -2.1$ and rules out conventional synchrotron emission as the dominant foreground. (Since the WENSS is an interferometric survey primarily designed to study discrete sources, the data are insensitive to zero-point flux from extended emission. It is not clear how much this affects the above conclusion.) As with the DMR and Saskatoon data, the 14.5 GHz foreground emission was correlated with dust, but it was difficult to attribute it to spatially correlated free-free emission because there was negligible Hα emission in the vicinity. To reconcile this, a gas temperature in excess of 1 million degrees would be needed to suppress the Hα. Flat-spectrum synchrotron was also suggested as a possible source; it had been previously observed in other sky regions and it would obviate the need for such a high temperature and pressure.

Draine & Lazarian (1998) dismissed the hot ionized gas explanation on energetic grounds and instead suggested that the emission (which they described as "anomalous") be attributed to electric dipole rotational emission from very small dust grains—a mechanism first proposed by Erickson (1957) in a different astrophysical context. One of the hallmarks of this mechanism is that it produces a frequency spectrum that peaks in the 10–60 GHz range and falls off fairly steeply on either side.

de Oliveira-Costa et al. (1998) analyzed the nearly full-sky 19 GHz sky map (Boughn et al. 1992) and found some correlation with the 408 MHz synchrotron emission, but found a stronger correlation with the *COBE* DIRBE 240 μm dust emission. They concluded that the 19 GHz data were consistent with either free-free or spinning dust emission.

Leitch (1998) commented that the preferred model of Draine & Lazarian (1998) could produce the RING5m foreground component at 31.7 GHz, but that it only accounted for at most 30% of the 14.5 GHz emission, even when adopting unlikely values of the grain dipole moment. Since Leitch et al. (2000) were primarily interested in studying the CMB anisotropy, they considered using the *IRAS* 100 μm map as a foreground template to remove the "anomalous" emission, regardless of its physical origin. They found, however, that fitting only a CMB component and a dust-correlated component produced an unacceptably high $\chi^2_\nu = 10$ per degree of freedom. Thus, while the radio foreground morphology correlates with dust, the correlation is not perfect.

Finkbeiner et al. (2002) used the Green Bank 140 foot (30.48 m) telescope to search for spinning dust emission in a set of dusty sources selected to be promising for detection. Ten infrared-selected dust clouds were observed at 5, 8, and 10 GHz. Eight of the 10 sources yielded negative results, one was marginal, and one (the only diffuse H II region of the 10, LPH 201.6) was claimed as a tentative detection based on its spectral index of $\beta > -2$. Recognizing that this spectrum does not necessarily imply spinning dust emission, Finkbeiner et al. (2002) offer three additional requirements to convincingly demonstrate the detection of spinning dust, and concluded that none of the three requirements was met by the existing data. The absence of a rising spectrum in most of the sources may be taken as evidence that spinning dust emission is not typically dominant in this spectral region, at least for this type of infrared-selected cloud. The tentative detection in LPH 201.6 has met with three criticisms: (1) lack of evidence for the premise that its radio emission is proportional to its far-infrared dust emission (Casassus et al. 2004), (2) the putative spinning dust emission is stronger than theory predicts (McCullough & Chen 2002), and (3) the positive spectral index may be accounted for by unresolved optically thick emission (McCullough & Chen 2002). On the latter point, follow-up observations failed to identify a compact H II region candidate (P. R. McCullough 2006, private communication).

Bennett et al. (2003c) fit the first-year *WMAP* foreground data to within $\sim$1% using a maximum entropy method (MEM) analysis (see also § 4.5). As with the above-cited results, *WMAP* found that the 22–33 GHz foregrounds are dominated by a component with a synchrotron-like spectrum, but a dustlike spatial morphology. Bennett et al. (2003c) suggested that this may be due to spatially varying synchrotron spectral indices acting over a large frequency range, significantly altering the synchrotron morphology with frequency. A spinning dust component with a thermal dust morphology and the Draine & Lazarian spectrum could not account for more than $\sim$5% of the emission at 33 GHz. Of course, the *WMAP* fit did not rule out spinning dust as a subdominant emission source (as it surely must be at some level), nor did it rule out spinning dust models with other spectra or spatial morphologies.

Casassus et al. (2004) report evidence for anomalous microwave emission in the Helix planetary nebula at 31 GHz, where at least 20% of the emission is correlated with 100 μm dust emission. They rejected several explanations. The observed features are not seen in Hβ, ruling out free-free emission as the source. Cold grains are also ruled out as the source by the absence of 250 GHz continuum emission. Very small grains are not expected to survive in planetary nebulae, and none have been detected in the Helix, but Fe is strongly depleted in the gas. Instead, Casassus et al. (2004) favor the notion of magnetic dipole emission (produced by variations in grain magnetization) from hot ferromagnetic classical grains (Draine & Lazarian 1999). Although the derived emissivity per nucleon in the Helix is a factor of $\sim$5 larger than the highest end of the range predicted by Draine & Lazarian (1999) this excess could be explained by a high dust temperature, since Draine & Lazarian (1999) assume an ISM temperature of 18 K instead of a typical planetary nebula dust temperature of $\sim$100 K. The fraction of 31 GHz Helix emission attributable to free-free is estimated to be in the range of 36%–80%. This low level of free-free emission implies an electron temperature of $T_e = 4600 \pm 1200$ K, which is much lower than the value $T_d \sim 9000$ K based on collisionally excited lines. This discrepancy may be due to strong temperature variations within the nebula. Casassus et al. (2004) suggest that the Finkbeiner et al. (2002) measurement of LPH 201.6 may also be produced by magnetic dipole emission from classical dust grains.

De Oliveira-Costa et al. (2004a) correlate the Tenerife 10 and 15 GHz data (Gutiérrez et al. 2000) with the *WMAP* nonthermal ("synchrotron") map that was produced as part of the first-year maximum entropy method (MEM) analysis of the *WMAP* foreground signal. They detect a low-frequency rolloff in the correlated emission, as shown below in Figure 6. We consider this result after discussing the 3 year MEM analysis in the next section.

Fernandez-Cerezo et al. (2006) report new measurements with the COSMOSOMAS experiment covering 9000 deg^2 with $\sim1^\circ$ resolution at frequencies of 12.7, 14.7, and 16.3 GHz. In addition to CMB signal and what is interpreted to be a population of unresolved radio sources, they find evidence for diffuse emission that is correlated with the DIRBE 100 μm and 240 μm bands. As with many of the above-mentioned results, they find that the correlated signal amplitude rises from 22 GHz (using *WMAP* data) to 16.3 GHz, and that it shows signs of flattening below 16.3 GHz "compatible with predictions for anomalous microwave emission related to spinning dust."

The topic of anomalous dust emission remains unsettled, and is likely to remain so until high-quality diffuse measurements are available over a modest fraction of sky in the 5–15 GHz frequency range. We offer some further comments after presenting the 3 year MEM results in the following section.

4.5. *Maximum Entropy Method* (*MEM*) *Foreground Analysis*

Bennett et al. (2003c) described a MEM-based approach to modeling the multifrequency *WMAP* sky maps on a pixel-by-pixel basis. Since the method is nonlinear, it produces maps with complicated noise properties that are difficult to propagate in cosmological analyses. As a result, it is not a promising method for foreground removal. However, the method is quite useful in helping to separate Galactic foreground components by emission mechanism, which in turn informs our understanding of the foregrounds.

We model the temperature map at each frequency, ν, and pixel, p, as

$$\begin{aligned} T_m(\nu, p) \equiv\ & T_{\rm cmb}(p) + S_s(\nu, p)T_s(p) \\ & + S_{\rm ff}(\nu, p)T_{\rm ff}(p) + S_d(\nu, p)T_d(p), \end{aligned} \quad (2)$$

where the subscripts cmb, s, ff, and d denote the CMB, synchrotron (including any anomalous dust component), free-free, and thermal dust components, respectively. The term $T_c(p)$ is the spatial distribution of emission component c in pixel p, and $S_c(\nu, p)$ is the spectrum of emission c, which is not assumed to be uniform across the sky. We normalize the spectra ($S \equiv 1$) at the K-band for the synchrotron and free-free components, and at the W-band for the dust component.

The model is fit in each pixel by minimizing the functional $H = A + \lambda B$ (Press et al. 1992), where $A = \sum_\nu [T(\nu, p) - T_m(\nu, p)]^2/\sigma_\nu^2$ is the standard χ^2 of the model fit, and $B = \sum_c T_c(p) \ln[T_c(p)/P_c(p)]$ is the MEM functional (see below). The parameter λ controls the relative weight of A (the data) and B (the prior information) in the fit. In the functional B, the sum over c is restricted to Galactic emission components, and $P_c(p)$ is a prior estimate of $T_c(p)$. The form of B ensures the positive value of the solution $T_c(p)$ for the Galactic components, which greatly alleviates degeneracy between the foreground components.

Throughout the MEM analysis, we smooth all maps to a uniform 1° angular resolution. To improve our ability to constrain and understand the foreground components, we first subtract a prior estimate of the CMB signal from the data rather than fit for it. We use the ILC map described in § 5.2 for this purpose and subtract it from all 5 frequency band maps. Since *WMAP* employs differential receivers, the zero level of each temperature map is unspecified. For the MEM analysis we adopt the following convention. In the limit that the Galactic emission is described by a plane-parallel slab, we have $T(|b|) = T_p \csc|b|$, where T_p is the temperature at the Galactic pole. For each of the five frequency band maps, we assign the zero level such that a fit of the form $T(|b|) = T_p \csc|b| + c$, over the range $-90^\circ < b < -15^\circ$, yields $c = 0$.

We construct a prior estimate for dust emission, $P_d(p)$, using Model 8 of Finkbeiner et al. (1999) evaluated at 94 GHz. The dust spectrum is modeled as a straight power law, $S_d(\nu) = (\nu/\nu_{\rm W})^{+2.0}$. For free-free emission, we estimate the prior, $P_{\rm ff}(p)$, using the extinction-corrected Hα map (Finkbeiner 2003). This is converted to a free-free signal using a conversion factor of 11.4 μK R^{-1} (units of antenna temperature at the K-band). We model the spectrum as a straight power law, $S_{\rm ff}(\nu) = (\nu/\nu_{\rm K})^{-2.14}$. As noted in § 4.1, the main source of uncertainty in this free-free estimate is the level of extinction correction (in addition to any Hα photometry errors). We reduce λ in regions of high dust optical depth to minimize the effect of errors in the prior.

For the synchrotron emission, we construct a prior estimate, $P_s(p)$, by subtracting an extragalactic brightness of 5.9 K from the Haslam 408 MHz map (Lawson et al. 1987) and scaling the result to K-band assuming $\beta_s = -2.9$. Since the synchrotron spectrum varies with position on the sky, this prior estimate is expected to be imperfect. We account for this in choosing λ, as described below. We construct an initial spectral model for the synchrotron, $S_s(\nu, p)$, using the spectral index map $\beta_s(p) \equiv \beta(408\ \mathrm{MHz}, 23\ \mathrm{GHz})$.

Specifically, we form $S_s(\nu, p) = (\nu/\nu_{\rm K})^{\beta_s - 0.25[\beta_s+3.5]}$ for the Ka-band, and $S_s(\nu, p) = S_s(\nu_{Ka}, p)(\nu/\nu_{Ka})^{\beta_s - 0.7[\beta_s+3.5]}$ for the Q-, V-, and W-bands ($S_s \equiv 1$ for the K-band). This allows for a β-dependent steepening of the synchrotron spectrum at microwave frequencies. In our first-year results, use of this initial spectral model produced solutions with zero synchrotron signal, $T_s(p)$, in a few low-latitude pixels for which the K–Ka spectrum is flatter than free-free emission. For the 3 year analysis, this problem is handled by setting the initial model, S_s, to be flatter than free-free emission in these pixels.

For all three emission components, the priors P_c and the spectra S_c are fixed during each minimization of H. As described below, we iteratively improve the synchrotron spectrum model based on the residuals of the fit.

The parameter λ controls the degree to which the solution follows the prior. In regions where the signal is strong, the data alone should constrain the model without the need for prior information, so λ can be small (although we maintain $\lambda > 0$ to naturally impose positive value on T_c and reduce degeneracy among the emission components). As in the first-year analysis, we base $\lambda(p)$ on the foreground signal strength: $\lambda(p) = 0.6[T_{\rm K}(p)/1\ {\rm mK}]^{-1.5}$, where $T_{\rm K}(p)$ is the K-band map (with the ILC map subtracted) in units of mK, antenna temperature. This gives $0.2 \lesssim \lambda \lesssim 3$.

After each minimization of H, we update S_s for the K- through V-band according to

$$S_s^{\rm new}(\nu, p)T_s(p) = S_s(\nu, p)T_s(p) + g\,R(\nu, p), \tag{3}$$

where $R(\nu, p) \equiv T(\nu, p) - T_m(\nu, p)$ is the solution residual, and g is a gain factor that we set to 0.5. For the W-band we update S_s by power-law extrapolation using the inferred Q- and V-band spectral index. For some low-S/N pixels, we occasionally find $\beta_s(\nu_{\rm Q}, \nu_{\rm V}) > 0$. In a change from our first-year analysis, we now extrapolate the synchrotron spectrum from V- to W-band using $\beta_s = -3.3$. This change affects only 7% of pixels.

We iterate the minimization of H and the update of S_s 11 times. At the end of this cycle, the residual, $R(\nu, p)$, is less than 1% of the total signal $T(\nu, p)$. However, there are still several sources of potential error in the component decomposition, including:

1. *Zero-level uncertainty.*—As noted above, we use a plane-parallel slab model to assign the sky map zero point at each frequency. We estimate the uncertainty in this convention by fitting the model separately in the northern and southern Galactic hemispheres. These separate fits change the zero levels by as much as 4 μK. When these differences are propagated into $T(\nu, p)$, the output maps, T_c, change by $\lesssim$15%, $\lesssim$5%, and $\lesssim$2% for the free-free, synchrotron, and dust components, respectively, at low Galactic latitudes.

2. *Dust spectrum uncertainty.*—Changing β_d by 0.2 changes the component maps by $\lesssim$10%, $\lesssim$3%, and $\lesssim$2% for the free-free, synchrotron, and dust components, respectively, at low Galactic latitudes.

3. *Dipole subtraction uncertainty.*—A 0.5% dipole error would result in a systematic 0.5% gain error in all bands. The dominant effect would be to rescale each component map by 0.5%.

4. *CMB signal subtraction uncertainty.*—Errors in the ILC estimate of the CMB signal will produce errors in the corrected Galactic data, $T(\nu, p) - T_{\rm ILC}(p)$, used in the MEM analysis. We quantify ILC errors in § 5.2, but note here that they are small compared to the total Galactic signal at low latitudes. However, they plausibly dominate the total uncertainty at high Galactic latitudes, where the *WMAP* data are (fortunately) dominated by CMB signal. Fractional uncertainties of $\sim$100% are not unlikely in the foreground model at high latitudes.

5. *Individual component degeneracy.*—While the total model residuals are small, there is still potentially significant uncertainty in the individual foreground components. The program outlined above produces three component maps, T_s, $T_{\rm ff}$, and T_d, and the synchrotron spectrum model $S_s(\nu, p)$. To illustrate the degeneracy between these outputs, we consider a simplified single-pixel model of the form

$$T_m(\nu) \equiv \langle S_s(\nu, p)\rangle T_s + S_{\rm ff}(\nu)T_{\rm ff} + S_d(\nu)T_d, \tag{4}$$

where the angle brackets indicate a full-sky average, and we explicitly evaluate the average MEM functional,

$$H = \sum_\nu \frac{[\langle T(\nu, p)\rangle - T_m(\nu)]^2}{\sigma_\nu^2} + \langle\lambda(p)\rangle \sum_c T_c \ln\left[\frac{T_c}{\langle P_c(p)\rangle}\right], \tag{5}$$

for selected pairs of parameters, while marginalizing over the rest. Contour plots of H are shown in Figure 4. For the panels that explore the shape of the synchrotron spectrum, S_s, we parameterize it as a power law with a steepening parameter, $\beta_s(\nu) = \beta_0 + (d\beta_s/d\log\nu)(\log\nu - \log\nu_{\rm K})$ and evaluate H as a function of $d\beta_s/d\log\nu$, while marginalizing over β_0. For the rest, we iteratively update S_s as per equation (3). For the most part, the output parameters are only weakly correlated; the most notable degeneracy is between the free-free amplitude and the synchrotron amplitude. *WMAP* data tightly constrain the *sum* of the two, but their difference is determined by the relative amplitude of the prior estimates for these two components, and by the initial synchrotron spectrum model. The synchrotron spectrum is found with modest significance to be steepening with increasing frequency. However, the dust index, β_d (not shown), is poorly constrained; thus our conclusion in the first-year analysis that $\langle\beta_d\rangle = 2.2$ was not well founded, on further investigation.

Figure 5 shows the three input prior maps, $P_c(p)$, and the corresponding output component maps, $T_c(p)$, obtained from the 3 year data. These maps are available on LAMBDA as part of the 3 year data release. The maps are displayed using a logarithmic color stretch to highlight a range of intensity levels. The morphology and amplitude of the thermal dust emission are well predicted by the prior (FDS99) dust map (see also § 5.3). The free-free emission is generally overpredicted by the prior discussed above, especially in regions of high extinction. But even in regions where the extinction is low, we find the mean free-free to Hα ratio at K-band to be closer to $\sim$8 μK R^{-1} than the value of 11.4 μK R^{-1} assumed in generating the prior. Moreover, we find considerable variation in this ratio (a factor of $\sim$2), depending on location.

The most notable discrepancy between prior and output maps is seen in the synchrotron emission. Specifically, the K-band signal has a much more extended Galactic longitude distribution than does the 408 MHz emission, and it is remarkably well correlated with the thermal dust emission. Is this K-band nonthermal component due to anomalous dust emission or to mostly flat-spectrum synchrotron emission that dominates at microwave frequencies and is well correlated with dusty active star-forming regions? We cannot answer this question with *WMAP* data alone because the frequency range of *WMAP* does not extend low enough to see the predicted rollover in the low-frequency anomalous dust spectrum. However, we note the following points.

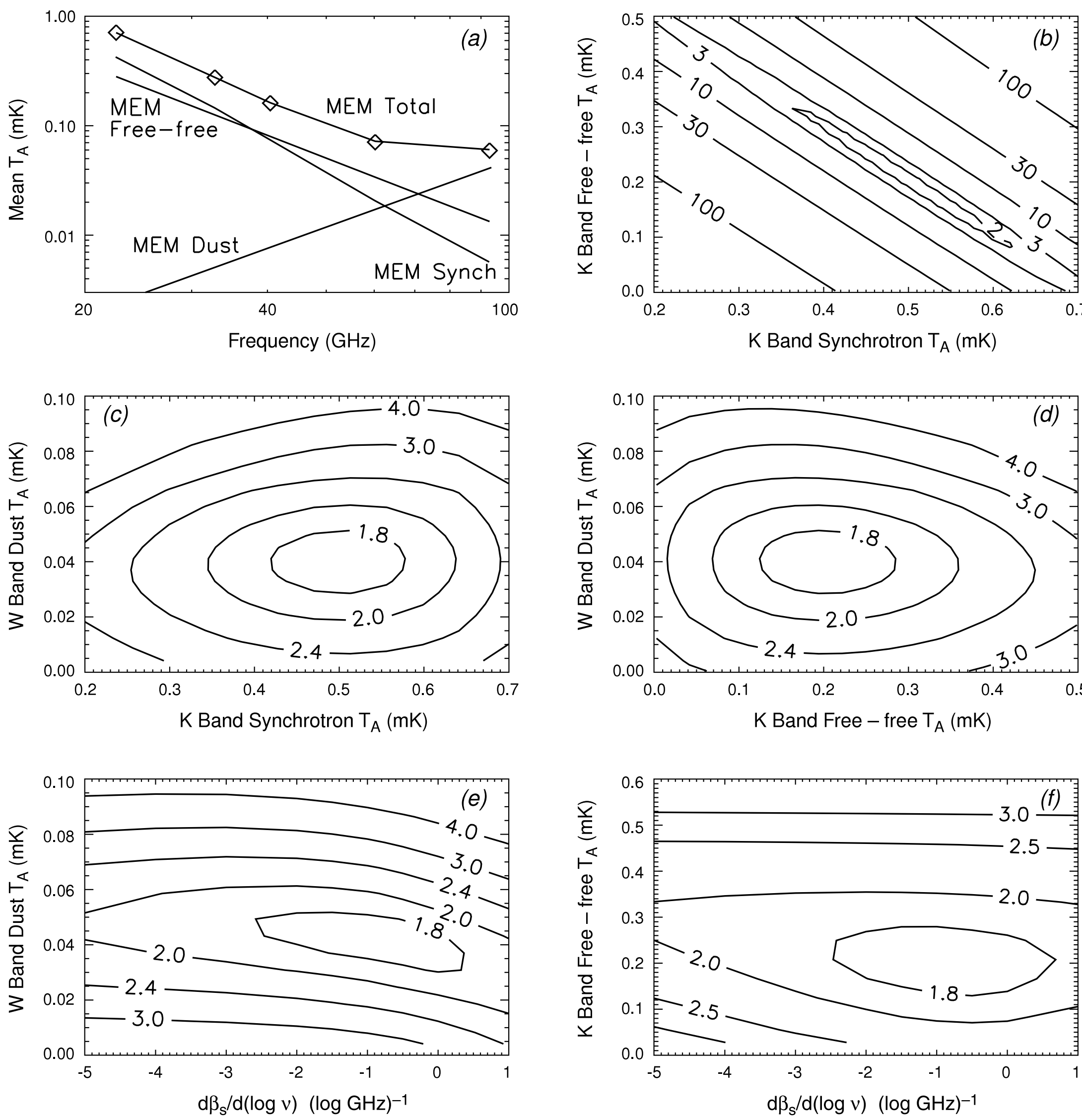

FIG. 4.—Results from the MEM foreground degeneracy analysis. (*a*) The spectrum of total foreground emission (*diamonds*) compared to the sum of the MEM components (*lines connecting the diamonds*), averaged over the full sky. The three component spectra of the model are also shown, as indicated. (*b–f*) The contour plots illustrate the degeneracy between selected components. The panels show the change in the MEM functional (in units of $\Delta\chi^2$) as a function of two global model parameters. For example, panel *b* shows the change in the MEM functional that results from adding a constant value to the synchrotron and/or free-free solutions, while panel *f* shows the dependence of the functional on a global steepening of the synchrotron spectrum, modeled as $\beta_s = \beta_0 + d\beta_s/d\log\nu(\log\nu - \log\nu_{\rm K})$. The only strong degeneracy is between the synchrotron and free-free amplitudes in (*b*). This effect is mitigated by the prior distributions assumed for each component (see text). The dust spectral index, β_d, was found to be essentially unconstrained, so contour plots for that quantity are not shown.

In Figure 6 we show the mean spectra of the three Galactic emission components observed by *WMAP*, in addition to the sum of the three. For comparison, we also show the signal observed at 408 MHz and we infer the signals at 10 and 15 GHz based on correlation analyses of the Tenerife CMB data by de Oliveira-Costa et al. (2004c, 1999). The curves show the mean signal in the range $20^\circ < |b| < 50^\circ$, as computed from the output MEM component maps: blue is dust, green is free-free, red is the nonthermal signal, and black is the sum of the three. The total intensity of the 408 MHz emission is remarkably well matched to a simple power-law extrapolation of the total *WMAP* signal measured from K-band to V-band. The spectral index of the dashed black curve is -2.65 between 408 MHz and the K-band, and -2.69 between 408 MHz and the Q-band. If we interpret the nonthermal emission as synchrotron, the implied spectral index between 408 MHz and the K-band nonthermal component is -2.73.

As noted in § 4.4, de Oliveira-Costa et al. (2004a) correlate the Tenerife 10 and 15 GHz data with the first-year *WMAP* nonthermal MEM map. We infer the nonthermal signal at 10 and 15 GHz (shown in red in Fig. 6) by scaling the 3 year nonthermal map using the reported correlation coefficients. We find a frequency rollover consistent with de Oliveira-Costa et al. (2004a). Using the same scaling method, we also infer the 10 and 15 GHz signals derived from correlations with Hα emission (*green arrows*) and the Haslam 408 MHz (synchrotron) map (*gray points*). The derived free-free emission is lower than the extrapolation of the free-free emission inferred from *WMAP*—which is not physically tenable. Similarly, the Haslam-correlated emission at 15 GHz is substantially lower than it is at either 10 or 23 GHz. Thus, the sum of all correlated components in the 10 and 15 GHz data requires a substantial dip in the spectrum of the total emission (*filled black squares*), which is not hinted at by the Haslam or *WMAP* data (*dashed black line*). This may be a sign of substantial anomalous emission, but one must be cautious interpreting the spectra of correlation coefficients.

Page et al. (2007) have used the 3 year *WMAP* polarization data to construct a novel decomposition of the intensity foreground

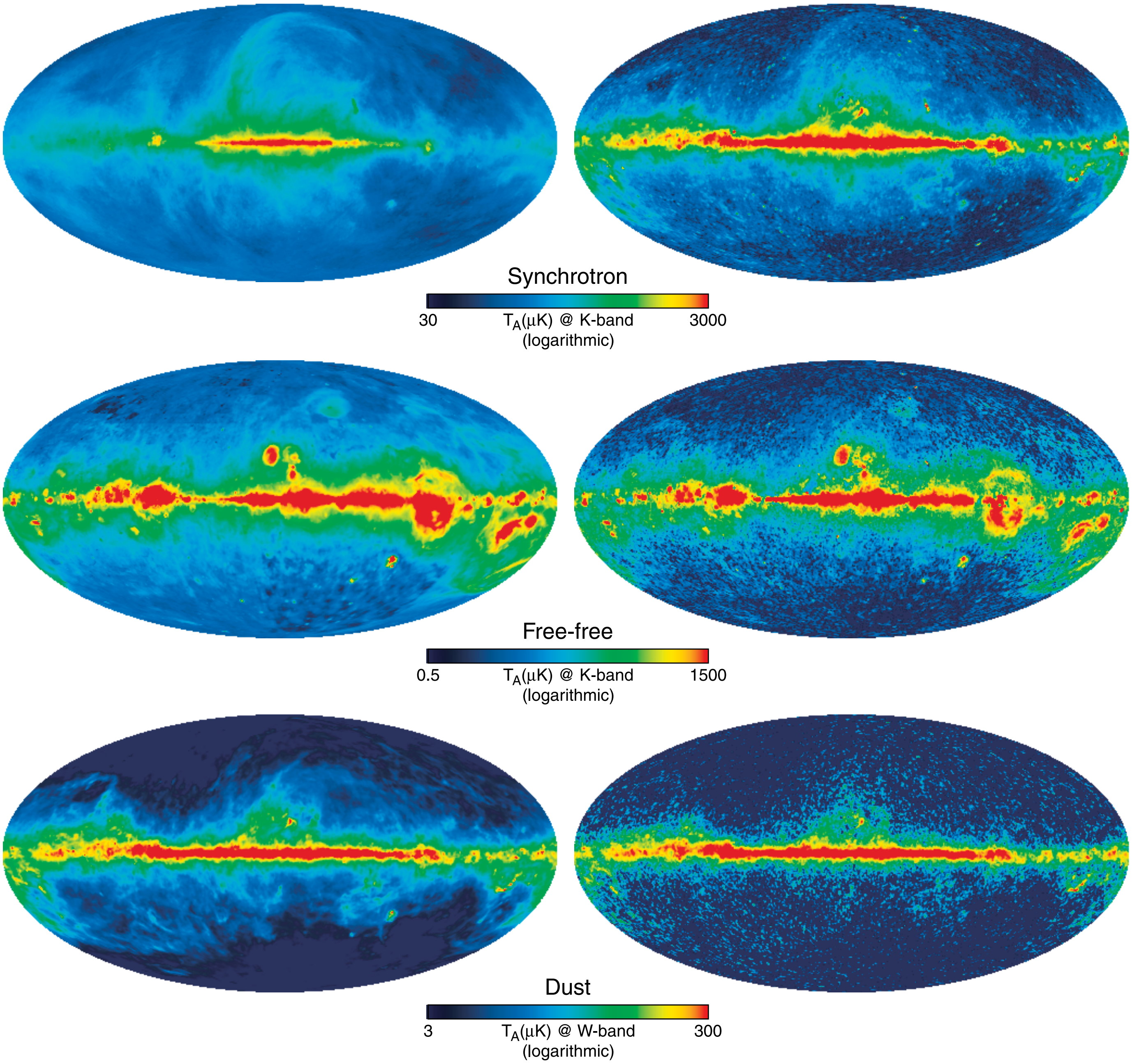

Fig. 5.—Galactic signal component maps from the maximum entropy method (MEM) analysis (§ 4.5). *Top to bottom*: Synchrotron, free-free, and dust emission with logarithmic temperature scales, as indicated. *Left*: Input prior maps for each component. *Right*: Output maps based on 3 year *WMAP* data for each component. See text for discussion.

signal at each *WMAP* frequency band. In brief, they predict a synchrotron polarization fraction from a model of the Galaxy's magnetic field strength and electron density. This fraction is derated by an empirical factor to account for missing structure in the model, then a "high-polarization fraction" component of the intensity signal is formed as $T_{\rm high}(\nu, p) \equiv P(\nu, p)/f(p)$, where $P(\nu, p)$ is the polarization intensity at frequency ν, in mK, and $f(p)$ is the model polarization fraction. After subtracting an estimate of the CMB and free-free signal from the intensity maps, the remaining nonthermal signal is attributed to a "low-polarization fraction" component, $T_{\rm low}(\nu, p) \equiv T'(\nu, p) - T_{\rm high}(\nu, p)$, where T' is the temperature map corrected for CMB and free-free emission. The high-fraction component has a morphology similar to the 408 MHz emission (Fig. 9 in Page et al. 2007), while low-fraction component has a very dustlike morphology (Fig. 13 in Page et al. 2007). While the accuracy of this decomposition depends on the model fraction, $f(p)$, the basic picture should inform future studies of anomalous emission.

5. GALACTIC FOREGROUND REMOVAL

The primary goal of foreground removal is to provide a clean map of the CMB for cosmological analysis; an improved understanding of foreground astrophysics is a secondary goal. Removal techniques typically rely on the fact that the foreground signals have spatial and spectral distributions that are quite different from the CMB. In this section we describe two-and-a-half approaches to foreground removal that use complementary information. The first is an update of the Internal Linear Combination (ILC) method we employed in the first-year analysis (Bennett et al. 2003c). The second is an updated approach to fitting Galactic emission templates to each *WMAP* frequency band map. The remaining strategy is to mask regions of the sky that are

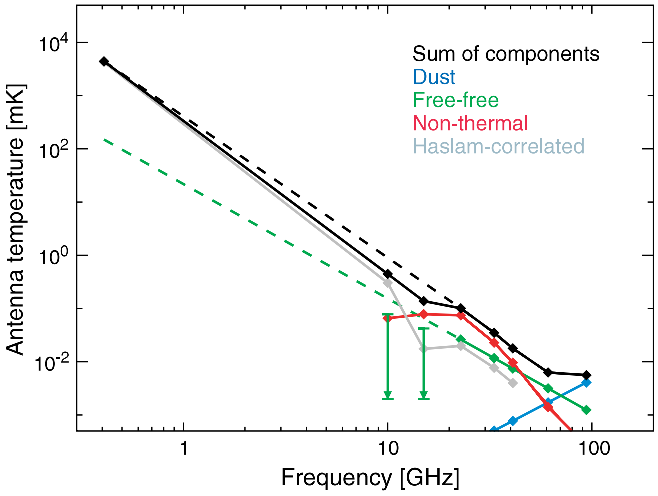

FIG. 6.—Mean Galaxy spectrum from 408 MHz to 94 GHz, based on data from Haslam, Tenerife, and *WMAP*. Each point is the mean signal in the Galactic latitude range $20° < |b| < 50°$ with the mean at the Galactic poles subtracted. The *WMAP* values (23–94 GHz) were derived from the MEM dust model (*blue*), the MEM free-free model (*green*), and the MEM nonthermal component (*red*), and the sum of the three (*black*). The Haslam (408 MHz) value is computed directly from the map (*black*). The dashed black curve is the interpolation of the total signal between 408 MHz and 23 GHz. The dashed green curve is the extrapolation of the *WMAP* MEM free-free result to 408 MHz assuming $\beta_{\rm ff} = -2.14$. The Tenerife values were obtained by taking the template correlation coefficients reported by de Oliveira-Costa et al. (2002, 2004a) (fit to $|b| > 20°$ data), scaling the templates to obtain model emission maps, then evaluating the mean signal in the same way as with the *WMAP* and Haslam data. The Tenerife correlation with Hα provided only upper limits for the free-free signal. See § 4.5 for more detail.

too contaminated to be reliably cleaned. Extragalactic sources are treated in § 6. For our primary CMB results, we analyze the masked, template-subtracted maps, but for some low-l applications we also analyze the ILC map as a consistency check.

5.1. *Temperature Masks*

Many regions of the sky are so strongly contaminated by foreground signals that reliable cleaning cannot be assured. These regions are masked for cosmological analysis, although the extent of the masking required depends on the type of analysis being done. Bennett et al. (2003c) defined a set of pixel masks based on the first-year K-band temperature map. Since these masks were based on high-S/N Galactic signal contours in the K-band data, we have not modified the diffuse emission masks for the 3 year analysis.

In addition to diffuse Galactic emission, point sources also contaminate the *WMAP* data. A point source mask was constructed for the first-year analysis that included all of the sources from Stickel et al. (1994); sources with 22 GHz fluxes ≥0.5 Jy from Hirabayashi et al. (2000); flat spectrum objects from Teräsranta et al. (2001); and sources from the blazar survey of Perlman et al. (1998) and Landt et al. (2001). The mask contained nearly 700 objects, including all 208 of the sources directly detected by *WMAP* in the first-year data. Each source was masked to a radius of 0.6°. For the 3 year analysis, we have supplemented the source mask with objects from the 3 year *WMAP* source catalog discussed in § 6.1. Of the newly detected sources, 81 were not included in the previous mask and have been added to the 3 year mask. Weaker, undetected sources still contribute to the high-l angular power spectrum. As discussed in § 7.2, we fit and subtract a residual source contribution to the multifrequency power spectrum data.

Figure 7 gives an overview of the microwave sky and indicates the extent of the various foreground masks. The yellow, salmon, and red shaded bands indicate the diffuse masks defined in Bennett et al. (2003c). The violet shading shows the "P06" polarization analysis mask described in Page et al. (2007). The small blue dots indicate point sources detected by *WMAP* (to alleviate crowding, the full source mask described above is not shown). In addition, some well-known sources and regions are specifically called out.

5.2. *The Internal Linear Combination (ILC) Method*

Linear combinations of the multifrequency *WMAP* sky maps can be formed using coefficients that approximately cancel Galactic signals while preserving the CMB signal. This approach exploits the fact that the frequency spectrum of foreground emission is different from that of the CMB. The method is "internal"

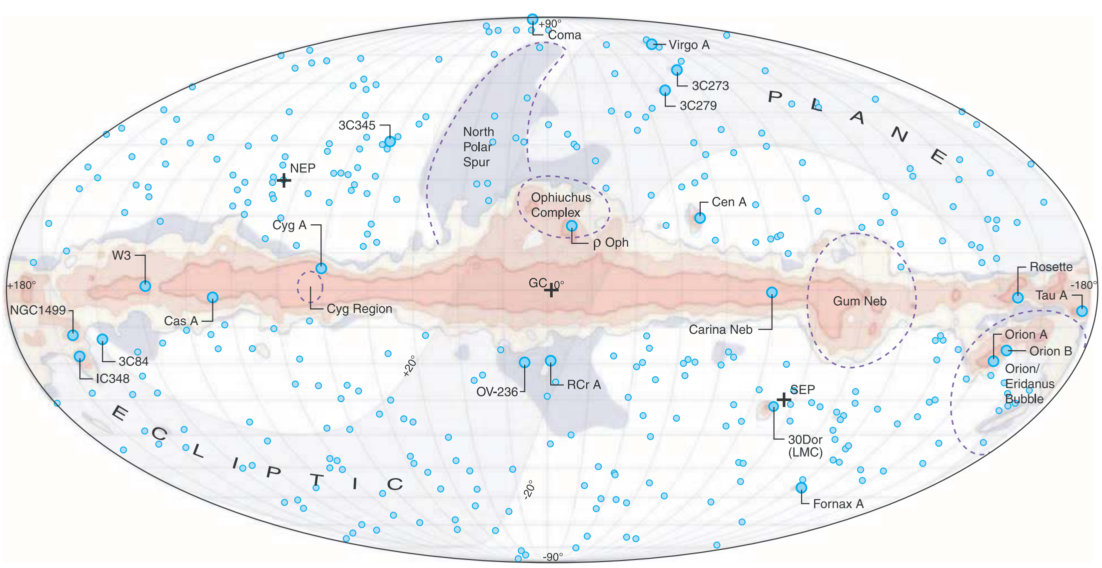

FIG. 7.—Overview of the microwave sky. The yellow, salmon, and red shaded regions indicate the Kp0, Kp2, and Kp8 diffuse emission masks, where the Galactic foreground signal is especially strong. See Bennett et al. (2003c) for a discussion of how these masks were constructed. The Kp0 and Kp2 masks are useful for cosmological analysis, and the Kp8 mask closely follows the "processing" mask described in Jarosik et al. (2007), which is used for reducing systematic errors in the sky maps. The violet shading shows the "P06" polarization analysis mask described in Page et al. (2007). The small blue dots indicate the position of point sources detected by *WMAP*. Some well-known sources and regions are specifically labeled.

in that it relies only on *WMAP* data, so the calibration and systematic errors of other experiments do not enter. There are a number of ways the coefficients can be determined, some of which require only minimal assumptions about the nature of the foreground signals. In the first year *WMAP* papers we introduced a method in which the coefficients were determined by minimizing the variance of the resulting map subject to the constraint that the coefficients sum to unity, in order to preserve the CMB signal. We called the resulting map the "ILC" map. In this section we elaborate on the strengths and limitations of the ILC method and quantify the uncertainties in the ILC map.

Eriksen et al. (2004a) have also analyzed the method as an approach to foreground removal. They devised an approach to variance minimization that employed a Lagrange multiplier to linearize the problem and dubbed the resulting map the "LILC" map, where the first L denotes Lagrange. They found their LILC map differed somewhat from the ILC map in certain regions of the sky. We have since verified that the two minimization methods produce identical results for a given set of inputs and that the differences were due to an ambiguity in the way the regions were defined in the original ILC description. Because the linearized algorithm is considerably faster than our original nonlinear minimization, we have adopted it in the present work.

5.2.1. *Uniform Foreground Spectra*

In order to better understand how errors arise in the ILC map, we first consider a simple scenario in which instrument noise is negligible and the spectrum of the foreground emission is uniform across the sky, or within a defined region of the sky. In this case, a frequency map, $T_i(p) \equiv T(\nu_i, p)$, may be written as a superposition of a CMB term, $T_c(p)$, and a foreground term, $S_i T_f(p)$, where $S_i \equiv S(\nu_i)$ describes the composite frequency spectrum of the foreground emission, and $T_f(p)$ describes the spatial distribution, so that $T_i(p) = T_c(p) + S_i T_f(p)$. A linear combination map has the form

$$\begin{aligned} T_{\rm ILC}(p) = \sum_i \zeta_i T_i(p) &= \sum_i \zeta_i \left[T_c(p) + S_i T_f(p) \right] \\ &= T_c(p) + \Gamma T_f(p), \end{aligned} \tag{6}$$

where we have imposed the constraint $\sum_i \zeta_i = 1$, and have defined $\Gamma \equiv \sum_i \zeta_i S_i$.

Suppose we choose to determine the coefficients ζ_i by minimizing the variance of $T_{\rm ILC}$. Then,

$$\sigma_{\rm ILC}^2 = \langle T_{\rm ILC}^2(p) \rangle - \langle T_{\rm ILC}(p) \rangle^2 \tag{7}$$

$$\begin{aligned} &= \langle T_c^2 \rangle - \langle T_c \rangle^2 + 2\Gamma \left[\langle T_c T_f \rangle - \langle T_c \rangle \langle T_f \rangle \right] \\ &\quad + \Gamma^2 \left[\langle T_f^2 \rangle - \langle T_f \rangle^2 \right] \end{aligned} \tag{8}$$

$$= \sigma_c^2 + 2\Gamma\sigma_{cf} + \Gamma^2 \sigma_f^2 \tag{9}$$

where the angle brackets indicate an average over pixels, and we have defined the variance and covariance in terms of these averages. Note that this expression would still hold if we added an arbitrary constant to each frequency map, $T_i \rightarrow T_i + T_{0,i}$. The ILC variance will be minimized when

$$0 = \frac{\partial \sigma_{\rm ILC}^2}{\partial \zeta_i} = 2 \frac{\partial \Gamma}{\partial \zeta_i} \sigma_{cf} + 2\Gamma \frac{\partial \Gamma}{\partial \zeta_i} \sigma_f^2. \tag{10}$$

Thus the coefficients ζ_i that minimize $\sigma_{\rm ILC}^2$ give $\Gamma = -\sigma_{cf}/\sigma_f^2$, and in the absence of noise, the corresponding ILC solution is

$$T_{\rm ILC}(p) = T_c(p) - \left(\sigma_{cf}/\sigma_f^2 \right) T_f(p), \tag{11}$$

with

$$\sigma_{\rm ILC}^2 = \sigma_c^2 - \sigma_{cf}^2/\sigma_f^2. \tag{12}$$

In this ideal case, the frequency maps combine in such a way as to maximize the cancellation between CMB signal and foreground signal, producing a biased CMB map with $\sigma_{\rm ILC}^2 \leq \sigma_c^2$. We have tested this result with ideal simulations in which we generate five frequency maps, T_i, which include a Galaxy signal with a constant spectrum, S_i, and random realizations of CMB signal and instrument noise. We then generate ILC maps from each realization and compare the residual map, $T_{\rm ILC} - T_c$, to the bias prediction, $-(\sigma_{cf}/\sigma_f^2)T_f$. The results confirm that the above description is correct, and that instrument noise is not a significant concern in this situation. The level of the bias is typically $\sim$10 μK in the Galactic plane.

5.2.2. *Nonuniform Foreground Spectra*

To minimize the anticorrelation bias we should choose regions that minimize the covariance between the CMB and the foreground, $\langle T_c T_f \rangle$. However, in the previous analysis we assumed that the spectra of the foreground signals were constant over the sky. In reality these will vary as the ratio of synchrotron, free-free, and dust emission varies across the sky (and as the intrinsic synchrotron and dust spectra vary). In this case, the bias analysis becomes more complex. Specifically, the foreground component at each frequency may be written as $S_i(p)T_f(p)$, and the ILC map takes the form

$$T_{\rm ILC}(p) = T_c(p) + \Gamma(p) T_f(p), \tag{13}$$

where $\Gamma(p) \equiv \sum_i \zeta_i S_i(p)$. The ILC variance then generalizes to

$$\begin{aligned} \sigma_{\rm ILC}^2 = \langle T_c^2 \rangle - \langle T_c \rangle^2 &+ 2\left[\langle T_c \Gamma T_f \rangle - \langle T_c \rangle \langle \Gamma T_f \rangle \right] \\ &+ \left[\langle \Gamma^2 T_f^2 \rangle - \langle \Gamma T_f \rangle^2 \right]. \end{aligned} \tag{14}$$

Using the same reasoning that led to equation (10), we obtain the following result for the minimum variance solution

$$\langle \Gamma T_f \, S_i T_f \rangle = -\langle T_c \, S_i T_f \rangle. \tag{15}$$

This has the same interpretation as equation (10), in the sense that it relates the foreground variance to the CMB-foreground covariance. We can solve this equation for $\Gamma(p)$ by noting that $\Gamma(p) \equiv \sum_i \zeta_i S_i(p)$, so that

$$\sum_j \langle S_i T_f \, S_j T_f \rangle \zeta_j = -\langle T_c \, S_i T_f \rangle. \tag{16}$$

Now define $F_{ij} \equiv \langle S_i T_f \, S_j T_f \rangle$ and $C_i \equiv \langle T_c \, S_i T_f \rangle$, whereby

$$\Gamma = \sum_i \zeta_i S_i = -\sum_{ij} S_i (F^{-1})_{ij} C_j, \tag{17}$$

which is the multifrequency analog of equation (11). Once again, however, the bias in the ILC solution is proportional to (minus) the CMB-foreground covariance.

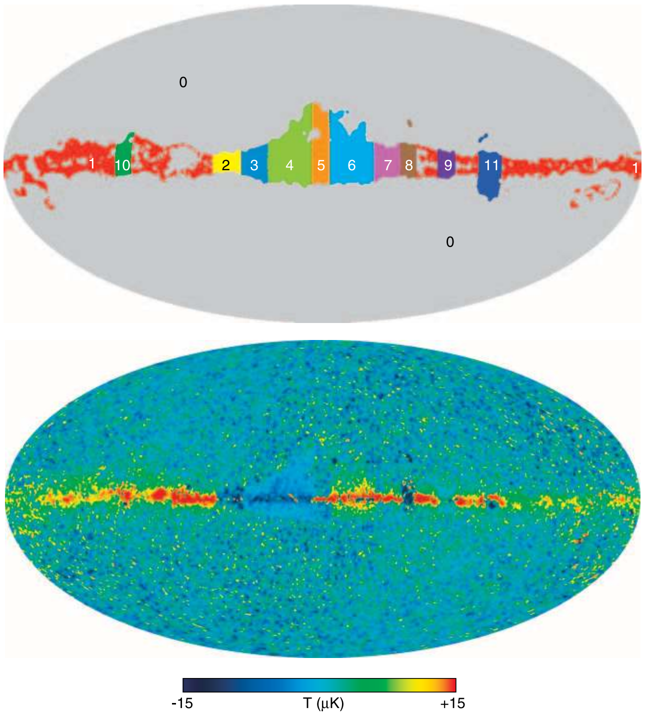

FIG. 8.— *Top*: Full-sky map color-coded to show the 12 regions that were used to generate the 3 year ILC map (see § 5.2). *Bottom*: Mean ILC residual map from 100 Monte Carlo simulations of CMB signal, Galactic foreground signal, and instrument noise. The CMB signal was drawn from a ΛCDM power spectrum that was modified to reproduce the power measured in the first-year spectrum at $l = 2$ and 3. The first-year MEM foreground model was used to generate the (fixed) Galactic maps. In the simulations, systematic errors arose in the recovered ILC maps due to a combination of effects: (1) a tendency for the minimum variance method to exploit (anti)alignments between the CMB and foreground signal, and (2) variations in the spectra of the foreground signal, due mostly to changes in the admixture of synchrotron, free-free, and dust emission (see § 5.2). This bias map was used to correct the 3 year ILC map (Fig. 9).

We have tested this expression with simulations like the ones described above, except this time we employ a three-component Galaxy model with variable spectra, $S(\nu_i, p)$, based on the first-year MEM model. As we discuss in more detail below, the simulations verify that the output ILC map is biased, $T_{\rm ILC}(p) - T_c(p) = \Gamma(p)T_f(p)$, with Γ as given in equation (17). Unfortunately, we do not know T_f and T_c a priori, and it has proven difficult to relate this bias expression to the frequency band maps, T_i, in a way the can be used to minimize the bias. As a result, we have primarily resorted to correcting the bias with Monte Carlo simulations, as we describe below.

Given the results above, and our previous experience with the ILC method, it is clear that one should subdivide the sky into regions selected by foreground spectra, in order to reduce bias prior to correcting it. We have carried out such a program for the 3 year analysis and have found it very difficult to improve on the region selection made in the first-year analysis (Bennett et al. 2003c). Nonetheless, we have adopted a few changes: (1) we eliminate the Taurus A region, as it is too small to ensure a reliable CMB-foreground separation (Eriksen et al. 2004a); (2) we add a new region to minimize dust residuals in the Galactic plane. This region is based on a $T_{\rm V} - T_{\rm W}$ color selection and encompasses the outer Galactic plane within the Kp2 cut. The new ILC region map is shown in Figure 8. The region designated 1, shown in red, replaces the old Taurus A region; the remaining regions are unchanged. This map is available on LAMBDA as part of the 3 year data release.

TABLE 4
ILC WEIGHTS BY REGION

Region[a]	K Band	Ka Band	Q Band	V Band	W Band
0	0.1559	−0.8880	0.0297	2.0446	−0.3423
1	−0.0862	−0.4737	0.7809	0.7631	0.0159
2	0.0358	−0.4543	−0.1173	1.7245	−0.1887
3	−0.0807	0.0230	−0.3483	1.3943	0.0118
4	−0.0781	0.0816	−0.3991	0.9667	0.4289
5	0.1839	−0.7466	−0.3923	2.4184	−0.4635
6	−0.0910	0.1644	−0.4983	0.9821	0.4428
7	0.0718	−0.4792	−0.2503	1.9406	−0.2829
8	0.1829	−0.5618	−0.8002	2.8464	−0.6674
9	−0.0250	−0.3195	−0.0728	1.4570	−0.0397
10	0.1740	−0.9532	0.0073	2.7037	−0.9318
11	0.2412	−1.0328	−0.2142	2.5579	−0.5521

[a] See Fig. 8 for the region definitions. See § 5.2 for notes on the handling of regions 0 and 1.

For each region n, we determine a set of band weights, $\zeta_{n,i}$, by minimizing the variance of the linear combination map $T_n(p) = \sum_{i=1}^{5} \zeta_{n,i} T_i(p)$ in that region, subject to the constraint $\sum_i \zeta_{n,i} = 1$. There are two exceptions to note. The coefficients for region 0 were derived from a subset of the data in that region, specifically pixels inside the Kp2 cut with $|l| > 60°$. The coefficients for region 1 were derived from a slightly larger region of data, specifically pixels inside the Kp2 cut with $|l| > 50°$, that pass the $T_{\rm V} - T_{\rm W}$ color cut. To ensure uniformity, the band maps have been smoothed to a common resolution of 1° FWHM. The coefficients $\zeta_{n,i}$ are given in Table 4.

We form a full-sky map by combining the N region maps, T_n; but to minimize edge effects, we blend the region maps as follows. We create a set of N full-sky weight maps, w_n such that $w_n(p) = 1$ for $p \in R_n$ and $w_n(p) = 0$ otherwise. We smooth these maps (which contain only ones and zeros) with a 1.5° smoothing kernel, to get smoothed weight maps, $\tilde{w}_n(p)$. The final full-sky map is then given by

$$T(p) = \frac{\sum_n \tilde{w}_n(p) T_n(p)}{\sum_n \tilde{w}_n(p)}, \tag{18}$$

where the sum is over the twelve sky regions.

In order to obtain the final bias correction, we generate multi-region Monte Carlo simulations, using the variable spectrum, MEM-based Galaxy model as input. We evaluate the error, $T_{\rm ILC} - T_c$, for each realization and compute a bias from the mean error averaged over 100 realizations. The result, shown in Figure 8, is roughly 20–30 μK in the Galactic plane, but substantially less off the plane. This map was used to correct the 3 year ILC map, which is shown in the middle panel of Figure 9. This Figure also shows the first-year ILC map (*top panel*) for comparison. The difference between the two (*bottom panel*) is primarily due to the new bias correction, but a small quadrupole difference, due to the changes noted in Figure 3, is also visible.

Based on the Monte Carlo simulations carried out for this ILC study, we estimate that residual Galactic removal errors in the 3 year ILC map are less than 5 μK on angular scales greater than $\sim$10°. But we caution that on smaller scales there is significant structure in the bias correction map that is still uncertain. On larger scales, we believe the 3 year ILC map provides a reliable estimate of the CMB signal, with negligible instrument noise, over the full sky. We analyze the low-l multipole moments of this map in § 7.3.

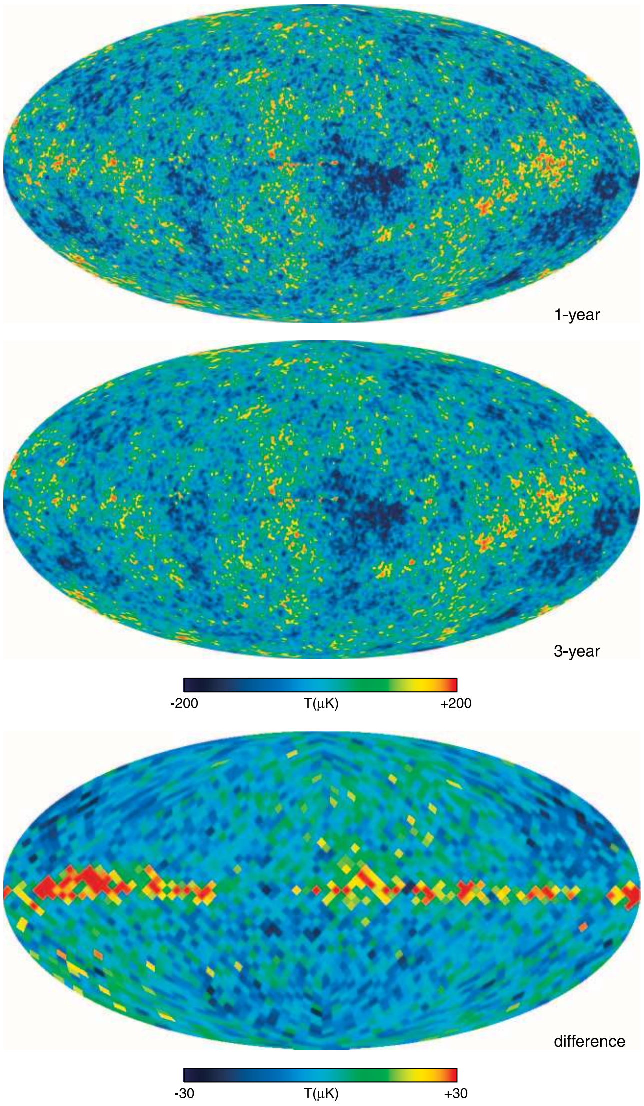

FIG. 9.—*Top*: First-year ILC map reproduced from Bennett et al. (2003c). *Middle*: 3 year ILC map produced following the steps outlined in § 5.2. *Bottom*: Difference between the two (1 yr − 3 yr). The primary reason for the difference is the new bias correction (Fig. 8). The low-l change noted in § 3 and shown in Fig. 3 is also apparent.

5.3. *Foreground Template Subtraction*

The ILC method discussed above produces a CMB map with complicated noise properties, while the MEM method discussed in § 4.5 is primarily used to identify and separate foreground components from each other. For most cosmological analyses one must retain the well-defined noise properties of the *WMAP* frequency band maps. To achieve this we form low-noise model templates of each foreground emission component and fit them to the *WMAP* sky maps at each frequency. After subtracting the best-fit model, we mask regions that cannot be reliably cleaned because of limitations in the template models. In this section we describe the model templates we use for synchrotron, free-free, and dust emission, and we estimate the residual foreground uncertainties that remain after these templates have been fit and subtracted. The *WMAP* band maps are calibrated in thermodynamic temperature units; where appropriate, we convert Galactic signals to units of antenna temperature using the factors g_ν given in Table 2.

In our first-year model we used the Haslam 408 MHz map as a template for synchrotron emission. We now use the *WMAP* K- and Ka-band data to provide a synchrotron template, as described below. This is preferable because: (1) the intrinsic systematic measurement errors are smaller in the *WMAP* data than in the Haslam data, and (2) the nonuniform synchrotron spectrum produces morphological changes in the brightness as a function of frequency (Bennett et al. 2003c), so that the low frequency Haslam map is less reliable at tracing microwave synchrotron emission than the *WMAP* data.

There are two potential pitfalls associated with using the K- and Ka-band data for cleaning: (1) the data are somewhat noisy, and since the template subtraction will be common to all cleaned channels, there can be a noise bias introduced in the inferred angular power spectrum. (But note that we use separate templates for each year of data, so the correlation only acts across frequency bands within a single year.) (2) Since the K- and Ka-band data are contaminated with point sources, this signal could interfere with the primary goal of cleaning the diffuse emission. Using the fitting coefficients obtained below and the known noise properties of the K- and Ka-band data, we estimate the noise bias in the final power spectrum to be $<5\ \mu\mathrm{K}^2$ near the first acoustic peak (<0.1% of the CMB signal), and even smaller at lower and higher multipoles. Furthermore, assuming the point source model given in equation (43), and the fact that the template has been smoothed to an effective resolution of 1°.0 FWHM, we estimate that sources contribute $<1\ \mu\mathrm{K}^2$ to the power spectrum at $l = 400$ in the $T_\mathrm{K} - T_\mathrm{Ka}$ template, and thus may be safely ignored. In the end, these pitfalls are not a source of concern for the 3 year analysis.

The difference map $T_\mathrm{K} - T_\mathrm{Ka}$, in thermodynamic units, cancels CMB signal, while it contains a specific linear combination of synchrotron and free-free emission (and a minimal level of thermal dust emission). We use this map as the first template in the model. For the second template we use the full-sky Hα map compiled by Finkbeiner (2003) with a correction for dust extinction (Bennett et al. 2003c). This template independently traces free-free emission, allowing the model to produce an arbitrary ratio of synchrotron to free-free emission at a given frequency (the limitations of Hα as a proxy for free-free are discussed below). For dust emission, we adopt "Model 8" from the Finkbeiner et al. (1999) analysis of *IRAS* and *COBE* data, evaluated at 94 GHz (see § 4.3). The full model has the form

$$M(\nu, p) = b_1(\nu)(T_\mathrm{K} - T_\mathrm{Ka}) + b_2(\nu) I_{\mathrm{H}\alpha} + b_3(\nu) M_d, \qquad (19)$$

where $b_i(\nu)$ are the fit coefficients for each template at frequency ν, and M_d is the dust map. As discussed below, this model is simultaneously fit to the Q-, V-, and W-band maps, and we constrain the coefficients b_2 and b_3 to follow the specified frequency spectra to minimize component degeneracy.

To clarify the physical interpretation of b_1 and b_2, we first note that $T_\mathrm{K} - T_\mathrm{Ka}$ may be rewritten in terms of synchrotron and free-free emission as

$$T_\mathrm{K} - T_\mathrm{Ka} = R_s T_s + R_\mathrm{ff} T_\mathrm{ff}, \qquad (20)$$

where T_s and T_ff are the synchrotron and free-free maps in antenna temperature at K-band, $R_c \equiv g_\mathrm{K} S_c(\nu_\mathrm{K}, p) - g_\mathrm{Ka} S_c(\nu_\mathrm{Ka}, p)$ is the surviving fraction of emission component c (synchrotron or free-free) in $T_\mathrm{K} - T_\mathrm{Ka}$, and S_c is the spectrum of component c, in antenna temperature, relative to K-band. To a very good approximation, the spectrum of free-free emission is $S_\mathrm{ff} = (\nu/\nu_\mathrm{K})^{-2.14}$ (§ 4.1), so that $R_\mathrm{ff} = 0.552$. For synchrotron emission, variations in the spectrum as a function of position will produce variations in R_s. For spectral indices in the range $\beta_s = -2.9 \pm 0.2$ we have $R_s = 0.667 \pm 0.026$. In the remainder of this section we assume $R_s \equiv 0.67$ and neglect the $\sim$2.5% error introduced by spectral index variations between K and Ka bands. Note that this value of R_s is only used to estimate the level of synchrotron emission in the template $T_{\rm K} - T_{\rm Ka}$; we do *not* constrain the fit coefficients b_1 to follow a specified frequency spectrum.

By adding the Hα map to the model, we allow the synchrotron to free-free ratio to vary as a function of frequency, but we must be cognizant of potential errors introduced by the use of Hα as a proxy for the free-free emission. Nominally we have $T_{\rm ff} = h_{\rm ff} I_{\rm H\alpha}$, where $I_{\rm H\alpha}$ is the Hα intensity in Rayleighs and $h_{\rm ff}$ is the free-free to Hα ratio. At the K-band, $h_{\rm ff}$ is predicted to be $\sim$11.4 μK R^{-1} (Bennett et al. 2003c), but the actual ratio is both uncertain and dependent locally on extinction and reflection. These effects make the Hα proxy unacceptable in the Galactic plane, and force one to mask these regions for CMB analysis. Outside the masked regions the variations in $h_{\rm ff}$ are primarily due to residual extinction and to variations in the temperature of the emitting gas. Here higher fractional errors can be tolerated because the total free-free signal is fainter.

Due to the uncertainties in the free-free to Hα ratio, and the fact that $T_{\rm K} - T_{\rm Ka}$ contains a mixture of synchrotron and free-free emission, care must be taken to interpret the model correctly. Let the combined synchrotron and free-free emission in the data at frequency ν be

$$T(\nu, p) = g(\nu)[S_s(\nu)T_s(p) + S_{\rm ff}(\nu)T_{\rm ff}(p)], \tag{21}$$

where the terms are as defined above. The synchrotron and free-free terms in the model may be written as

$$\begin{aligned} b_1(\nu)\,(T_{\rm K} - T_{\rm Ka}) + b_2(\nu) I_{\rm H\alpha} \\ &= b_1(\nu)[R_s T_s + R_{\rm ff} T_{\rm ff}] + [b_2(\nu)/h_{\rm ff}] T_{\rm ff} && (22) \\ &= [b_1(\nu) R_s] T_s + [b_1(\nu) R_{\rm ff} + b_2(\nu)/h_{\rm ff}] T_{\rm ff}. && (23) \end{aligned}$$

Comparing the synchrotron terms in equations (23) and (21), we can infer the mean synchrotron spectral index returned by the fit

$$\beta_s(\nu_{\rm K}, \nu) = \frac{\log\,[S_s(\nu)]}{\log\,(\nu/\nu_{\rm K})} = \frac{\log\,[b_1(\nu) R_s / g(\nu)]}{\log\,(\nu/\nu_{\rm K})}. \tag{24}$$

Comparing the free-free terms, and assuming $S_{\rm ff}$ is known, we can solve for the free-free to Hα ratio at the K-band,

$$h_{\rm ff} = \frac{b_2(\nu)}{g(\nu) S_{\rm ff}(\nu) - b_1(\nu) R_{\rm ff}}. \tag{25}$$

We fit the template model, equation (19), simultaneously to each of the eight Q- through W-band differencing assembly (DA) maps (the 3 year maps smoothed to 1° resolution) by minimizing χ^2

$$\chi^2 = \sum_{i,p} \frac{[T(\nu_i, p) - b_1(\nu)(T_{\rm K} - T_{\rm Ka}) - b_2(\nu) I_{\rm H\alpha} - b_3(\nu) M_d]^2}{\sigma_i^2}, \tag{26}$$

where $T(\nu_i, p)$ is the *WMAP* sky map from DA i (in thermodynamic units), σ_i^2 is the mean noise variance per pixel for DA i, and the second sum is over pixels outside the Kp2 sky cut. To regularize the model, we impose the following constraints on the fit coefficients: (1) all coefficients must be positive-definite, (2) the dust coefficients must follow a spectrum $b_3(\nu_i) \equiv b_3 g(\nu_i)(\nu_i/\nu_{\rm W1})^{+2.0}$, and (3) the free-free coefficients for each DA must follow a free-free spectrum, which leads to the form

$$b_2(\nu_i) \equiv b_2\left[g(\nu_i)(\nu_i/\nu_{\rm K})^{-2.14} - b_1(\nu_i) R_{\rm ff}\right]. \tag{27}$$

TABLE 5

Galactic Template Fit Coefficients

DA	b_1	b_2[a]	b_3[b]	β_s[c]	$h_{\rm ff}$
Q1	0.243	1.020	0.195	−3.15	6.28
Q2	0.242	1.046	0.193	−3.19	6.28
V1	0.054	0.700	0.448	−3.50	6.57
V2	0.052	0.678	0.463	−3.48	6.57
W1	0.000	0.405	1.226	...	6.72
W2	0.000	0.400	1.240	...	6.72
W3	0.003	0.397	1.207	...	6.71
W4	0.000	0.402	1.234	...	6.72

[a] Units of μK R^{-1}. Coefficients constrained to follow a free-free spectrum. See text for details.

[b] Dimensionless amplitude relative to FDS99 model 8 evaluated at 94 GHz. Coefficients forced to follow $\beta_d = +2.0$. See text for details.

[c] Synchrotron spectral index computed from eq. (24). The W-band fits imply $\beta_s(\nu_{\rm K}, \nu_{\rm W}) < -4$.

The synchrotron coefficients are fit separately for each differencing assembly. Given the 10 coefficients from the 3 year fit, we subtract the model from each single-year DA map to produce a set of cleaned maps. In doing so, we form separate single-year maps of $T_{\rm K} - T_{\rm Ka}$ to maintain rigorously independent noise between separate years of data.

The fit coefficients b_i are given in Table 5, along with derived values for β_s and $h_{\rm ff}$. To facilitate model subtraction, we tabulate values for b_2 and b_3 for each DA using the above constraints. Note that the FDS99 dust model, which predates *WMAP* by a few years, predicts the 94 GHz dust signal remarkably well. The synchrotron emission shows a steady steepening with increasing frequency, as seen in the first-year data (Bennett et al. 2003c). Also, the free-free to Hα ratio is seen to be $\sim$6.5 μK R^{-1}, which is roughly half of the 11.4 μK R^{-1} prediction. Taken together, this fit finds a remarkably low total Galactic foreground amplitude at the V-band.

Figure 10 shows the 3 year band maps before and after subtracting the above model. For comparison, the figure also shows the same 3 year maps after subtracting the first-year template-based model (Bennett et al. 2003c). In all panels an estimate of the CMB signal (the ILC map) has been subtracted to better show residual foreground errors. The main visible difference between the first-year and 3 year residual maps is the synchrotron subtraction error in the first-year model due to the use of the Haslam 408 MHz map. This is especially visible in the region of the North Polar Spur and around the inner Galaxy. Note also the significant model errors visible inside the Kp2 sky cut. This is presumably caused by a combination of synchrotron spectral index variations and errors in the extinction correction applied to the Hα template. Indeed, errors of up to 30 μK are also clearly visible in isolated regions outside the cut, especially in the vicinity of the Gum Nebula and the Ophiuchus complex. In § 7.2 we compare the foreground signal to the CMB and assess the

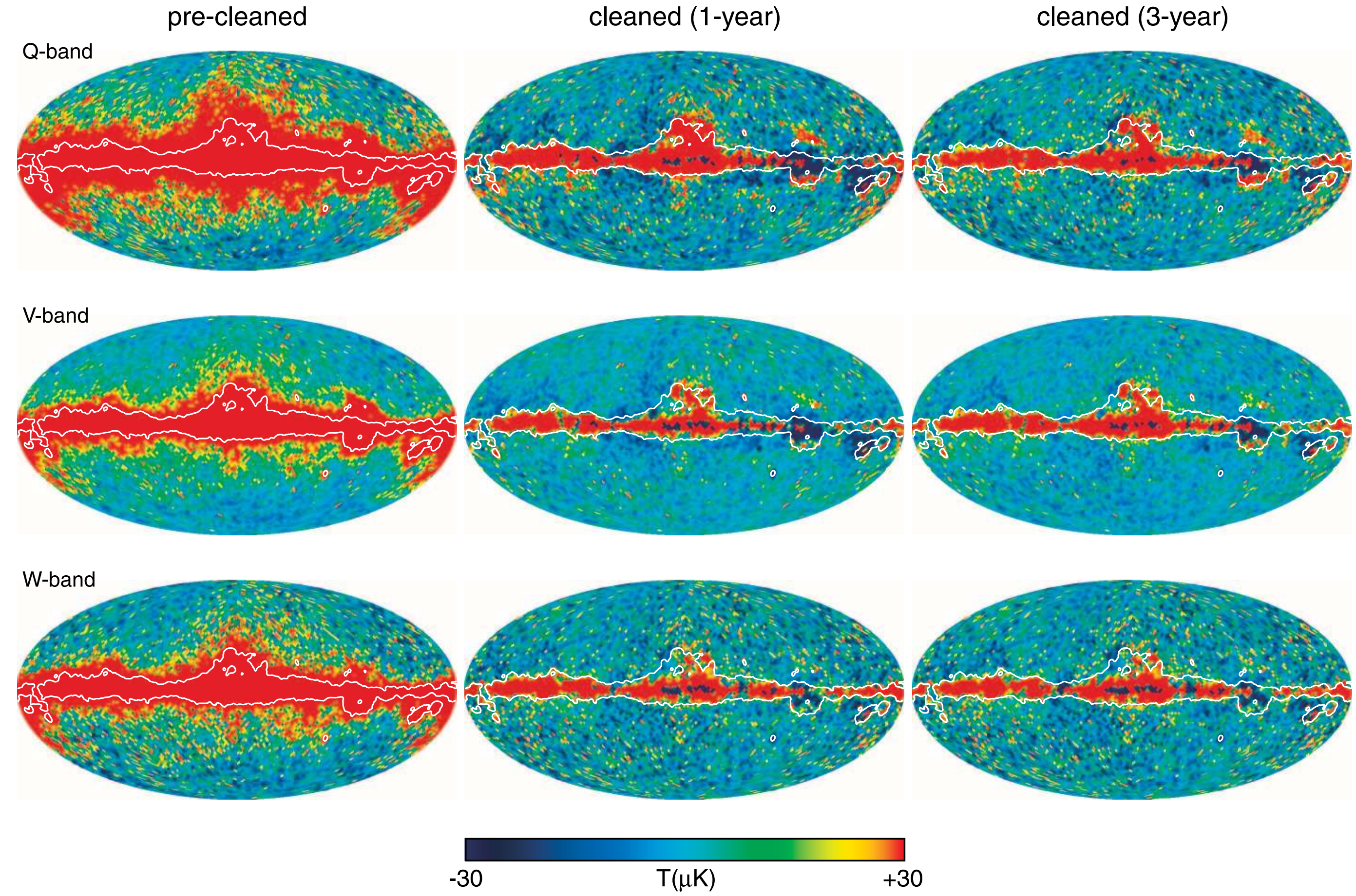

FIG. 10.—Galactic foreground removal with spatial templates. All maps in this figure are 3 year maps that have had the ILC estimate of the CMB signal subtracted off to highlight the foreground emission. The maps have been degraded to pixel resolution 5, are displayed in Galactic coordinates, and are scaled to ± 30 μK. The white contour indicates the perimeter of the Kp2 sky cut, outside of which the template fits were evaluated. The frequency bands Q through W are shown top to bottom. *Left*: Sky maps prior to the subtraction of the best-fit foreground model (§ 5.3). *Middle*: The same sky maps with the first-year template-based model subtracted. Note the high-latitude residuals in the vicinity of the North Polar Spur and around the inner Galaxy due to the use of the Haslam 408 MHz map as a synchrotron template. *Right*: The same sky maps with the 3 year template-based model subtracted. This model substitutes K- and Ka-band data for the Haslam data, which produces lower residuals outside the Kp2 sky cut. There are still isolated spots with residual emission of order 30 μK in the vicinity of the Gum Nebula and the Ophiuchus Complex (see Fig. 7). Note also that substantial errors ($\geq$30 μK) remain inside the Kp2 cut due to limitations in the template model.

degree to which these residual errors contaminate the CMB power spectrum.

6. EXTRAGALACTIC FOREGROUNDS

6.1. *Point Sources*

Extragalactic point sources contaminate the *WMAP* anisotropy data, and a few hundred of them are strong enough that they should be masked and discarded prior to undertaking any CMB analysis. In this section we describe a new direct search for sources in the 3 year *WMAP* band maps. Based on this search, we update the source mask that was used in the first-year analysis. In § 7.2 we describe our approach to fitting and subtracting residual sources in the data. Page et al. (2007) discuss the treatment of polarized sources.

For the first-year analysis, we constructed a catalog of sources surveyed at 4.85 GHz using the northern hemisphere GB6 catalog (Gregory et al. 1996) and the southern hemisphere PMN catalog (Griffith et al. 1994, 1995; Wright et al. 1994, 1996). The GB6 catalog covers the declination range $0^\circ < \delta < +75^\circ$ to a flux limit of 18 mJy, while the PMN catalog covers $-87^\circ < \delta < +10^\circ$ to a flux limit between 20 and 72 mJy. Combined, these catalogs contain 119,619 sources, with 93,799 in the region $|b| > 10^\circ$. We have examined the 3 year *WMAP* sky maps for evidence of these sources as follows: we bin the catalog by source brightness and, for each bin, we cull the corresponding sky map pixels that contain those sources. The data show a clear correlation between source strength and mean sky map temperature that disappears if the sky map pixels are randomized. The multifrequency *WMAP* data suggest that the detected sources are primarily flat-spectrum, with $\alpha \sim 0$.

In the first-year analysis, we produced a catalog of bright point sources in the *WMAP* sky maps, independent of their presence in external surveys. This process has been repeated with the 3 year maps as follows. We filter the weighted maps, $N_{\rm obs}^{1/2}T$ ($N_{\rm obs}$ is the number of observations per pixel) in harmonic space by $b_l/(b_l^2 C_l^{\rm cmb} + C_l^{\rm noise})$ (Tegmark & de Oliveira-Costa 1998; Refregier et al. 2000), where b_l is the transfer function of the *WMAP* beam response (Page et al. 2003a; Jarosik et al. 2007), $C_l^{\rm cmb}$ is the CMB angular power spectrum, and $C_l^{\rm noise}$ is the noise power. Peaks that are >5 σ in the filtered maps are fit in the unfiltered maps to a Gaussian profile plus a planar baseline. The Gaussian amplitude is converted to a source flux density using the conversion factors given in Table 5 of Page et al. (2003a). When a source is identified with >5 σ confidence in any band, the flux densities for other bands are given if they are >2 σ and the fit source width is

TABLE 6

WMAP Source Catalog

R.A.	Decl.	ID	K (Jy)	Ka (Jy)	Q (Jy)	V (Jy)	W (Jy)	α	5 GHz ID	Notes
00 06 05	−06 22	060	2.4 ± 0.08	2.2 ± 0.1	2.3 ± 0.2	2.3 ± 0.3	...	−0.0 ± 0.2	PMN J0006−0623	
00 12 56	−39 53	202	1.4 ± 0.06	1.3 ± 0.1	1.0 ± 0.1	1.5 ± 0.3	...	−0.2 ± 0.3	PMN J0013−3954	
00 19 32	26 02		1.1 ± 0.08	1.1 ± 0.2	0.9 ± 0.2	0.8 ± 0.2	...	−0.3 ± 0.5	GB6 J0019+2602	
00 19 33	20 19		1.1 ± 0.07	1.1 ± 0.1	0.9 ± 0.1	1.9 ± 0.4	...	0.2 ± 0.4	GB6 J0019+2021	
00 25 26	−26 04		1.0 ± 0.08	0.8 ± 0.1	...	...	...	−0.4 ± 1	PMN J0025−2602	a
00 26 03	−35 11		1.0 ± 0.08	1.0 ± 0.1	1.2 ± 0.1	1.2 ± 0.3	...	0.3 ± 0.4	PMN J0026−3512	
00 29 35	05 55		1.0 ± 0.07	1.4 ± 0.1	1.2 ± 0.1	...	...	0.4 ± 0.4	GB6 J0029+0554B	a
00 42 57	52 08		0.9 ± 0.05	0.6 ± 0.08	...	...	...	−0.9 ± 0.8	GB6 J0043+5203	
00 47 20	−25 15	062	1.1 ± 0.07	...	1.1 ± 0.1	...	...	−0.0 ± 0.5	PMN J0047−2517	
00 49 50	−57 40	179	1.3 ± 0.07	1.2 ± 0.1	1.0 ± 0.09	1.2 ± 0.2	0.9 ± 0.4	−0.3 ± 0.3	PMN J0050−5738	
00 50 45	−06 47		1.0 ± 0.07	1.2 ± 0.1	0.8 ± 0.1	1.1 ± 0.2	1.9 ± 0.6	0.1 ± 0.3	PMN J0051−0650	
00 50 47	−42 23		1.2 ± 0.05	1.2 ± 0.07	0.9 ± 0.09	0.8 ± 0.2	...	−0.3 ± 0.3	PMN J0051−4226	
00 51 06	−09 27	077	1.0 ± 0.08	0.9 ± 0.1	0.8 ± 0.1	...	...	−0.4 ± 0.6	PMN J0050−0928	
01 06 42	−40 35	171	1.8 ± 0.05	2.0 ± 0.09	1.8 ± 0.1	1.4 ± 0.2	1.3 ± 0.3	−0.1 ± 0.2	PMN J0106−4034	
01 08 26	13 20	079	1.4 ± 0.07	1.1 ± 0.2	1.0 ± 0.2	...	...	−0.7 ± 0.7	GB6 J0108+1319	
01 08 40	01 35	081	2.5 ± 0.08	2.5 ± 0.1	2.3 ± 0.2	2.4 ± 0.3	...	−0.1 ± 0.2	GB6 J0108+0135	a
01 15 11	−01 26		1.0 ± 0.07	1.2 ± 0.1	0.8 ± 0.2	0.5 ± 0.2	...	0.1 ± 0.6	PMN J0115−0127	
01 16 21	−11 37		1.3 ± 0.07	1.1 ± 0.1	1.2 ± 0.2	1.4 ± 0.3	...	−0.1 ± 0.4	PMN J0116−1136	
01 21 44	11 50		1.2 ± 0.07	1.1 ± 0.1	1.2 ± 0.2	...	...	−0.1 ± 0.5	GB6 J0121+1149	
01 25 20	−00 10	086	1.2 ± 0.07	1.3 ± 0.1	1.3 ± 0.1	1.2 ± 0.2	...	0.1 ± 0.3	PMN J0125−0005	a
01 32 35	−16 53	097	1.7 ± 0.07	1.8 ± 0.1	1.9 ± 0.1	...	...	0.2 ± 0.3	PMN J0132−1654	
01 37 01	47 52	080	4.2 ± 0.07	4.4 ± 0.1	4.2 ± 0.1	3.7 ± 0.2	2.2 ± 0.4	−0.1 ± 0.1	GB6 J0136+4751	
01 37 35	−24 28		1.0 ± 0.07	1.1 ± 0.1	1.7 ± 0.1	1.4 ± 0.2	1.0 ± 0.4	0.5 ± 0.3	PMN J0137−2430	
01 52 34	22 08		1.2 ± 0.1	1.5 ± 0.2	1.2 ± 0.2	1.4 ± 0.3	...	0.2 ± 0.4	GB6 J0152+2206	
02 04 51	15 13	092	1.4 ± 0.09	1.6 ± 0.2	1.5 ± 0.1	1.7 ± 0.4	...	0.1 ± 0.4	GB6 J0204+1514	
02 04 58	32 13	085	1.5 ± 0.09	1.4 ± 0.1	1.2 ± 0.2	0.7 ± 0.3	...	−0.4 ± 0.4	GB6 J0205+3212	
02 10 51	−51 00	158	2.6 ± 0.06	2.8 ± 0.1	2.8 ± 0.1	2.6 ± 0.2	3.0 ± 1	0.1 ± 0.1	PMN J0210−5101	
02 20 54	35 58		1.1 ± 0.08	1.1 ± 0.1	1.0 ± 0.2	...	...	−0.1 ± 0.6	GB6 J0221+3556	
02 22 45	−34 41	137	0.9 ± 0.04	1.0 ± 0.06	...	0.8 ± 0.2	...	0.0 ± 0.4	PMN J0222−3441	
02 23 16	43 04	084	1.8 ± 0.07	1.4 ± 0.1	1.4 ± 0.2	1.2 ± 0.3	1.7 ± 0.6	−0.4 ± 0.3	GB6 J0223+4259	a
02 31 40	13 18		1.4 ± 0.08	1.2 ± 0.1	1.3 ± 0.1	...	...	−0.2 ± 0.4	GB6 J0231+1323	
02 37 58	28 48	093	3.5 ± 0.08	3.1 ± 0.1	3.5 ± 0.2	2.9 ± 0.3	1.8 ± 0.6	−0.1 ± 0.2	GB6 J0237+2848	
02 38 53	16 36		1.3 ± 0.1	1.4 ± 0.2	1.4 ± 0.2	1.7 ± 0.3	...	0.2 ± 0.4	GB6 J0238+1637	
02 53 31	−54 41	155	2.5 ± 0.06	2.8 ± 0.09	2.8 ± 0.1	2.3 ± 0.2	2.5 ± 0.3	0.1 ± 0.1	PMN J0253−5441	
03 03 31	−62 12	162	1.4 ± 0.07	1.4 ± 0.1	1.4 ± 0.1	1.4 ± 0.2	...	0.0 ± 0.2	PMN J0303−6211	
03 08 25	04 04	102	1.3 ± 0.08	1.3 ± 0.1	1.4 ± 0.1	0.9 ± 0.2	...	−0.0 ± 0.4	GB6 J0308+0406	
03 09 47	−61 03	160	1.0 ± 0.07	1.3 ± 0.1	0.9 ± 0.08	1.0 ± 0.2	...	−0.0 ± 0.4	PMN J0309−6058	
03 12 08	−76 47	174	1.1 ± 0.06	1.2 ± 0.08	1.1 ± 0.09	1.1 ± 0.2	1.2 ± 0.4	0.0 ± 0.3	PMN J0311−7651	
03 19 45	41 31	094	10.8 ± 0.07	8.4 ± 0.1	7.0 ± 0.1	4.8 ± 0.3	3.0 ± 0.5	−0.7 ± 0.06	GB6 J0319+4130	
03 22 25	−37 11	138	18.5 ± 3.6	12.6 ± 1.9	10.5 ± 2.5	8.3 ± 2.1	...	−0.8 ± 0.2	1Jy 0320−37	b
03 25 11	22 24		1.0 ± 0.1	1.2 ± 0.2	1.1 ± 0.2	...	...	0.3 ± 0.7	GB6 J0325+2223	
03 29 46	−23 53	123	1.1 ± 0.05	1.3 ± 0.09	1.2 ± 0.1	1.0 ± 0.2	...	0.1 ± 0.3	PMN J0329−2357	
03 34 18	−40 07	146	1.6 ± 0.06	1.7 ± 0.09	1.6 ± 0.1	1.5 ± 0.2	...	0.0 ± 0.2	PMN J0334−4008	
03 36 49	−12 58		1.0 ± 0.07	...	1.2 ± 0.1	...	...	0.2 ± 0.5	PMN J0336−1302	
03 39 24	−01 44	106	2.6 ± 0.09	2.6 ± 0.1	2.7 ± 0.2	1.5 ± 0.3	3.4 ± 0.5	0.0 ± 0.2	PMN J0339−0146	
03 40 27	−21 21		1.1 ± 0.07	1.1 ± 0.1	1.2 ± 0.1	1.4 ± 0.2	...	0.1 ± 0.3	PMN J0340−2119	
03 48 51	−27 47	129	1.1 ± 0.04	1.0 ± 0.07	0.8 ± 0.09	1.4 ± 0.2	...	−0.2 ± 0.3	PMN J0348−2749	
03 58 43	10 29		1.2 ± 0.1	0.8 ± 0.2	...	...	...	−1.0 ± 1	GB6 J0358+1026	
04 03 57	−36 04	136	4.0 ± 0.06	4.6 ± 0.1	4.5 ± 0.1	4.3 ± 0.2	3.9 ± 0.4	0.1 ± 0.08	PMN J0403−3605	
04 05 37	−13 05	114	2.0 ± 0.07	2.1 ± 0.1	1.8 ± 0.1	1.6 ± 0.3	...	−0.2 ± 0.2	PMN J0405−1308	
04 07 01	−38 24	141	1.1 ± 0.06	1.1 ± 0.1	1.0 ± 0.1	...	...	−0.2 ± 0.5	PMN J0406−3826	
04 08 49	−75 03		0.8 ± 0.05	0.4 ± 0.07	0.6 ± 0.2	...	...	−1.2 ± 0.8	PMN J0408−7507	
04 11 24	76 55	082	1.0 ± 0.06	0.7 ± 0.1	0.8 ± 0.1	...	...	−0.4 ± 0.6	1Jy 0403+76	
04 23 17	−01 20	110	10.0 ± 0.08	10.4 ± 0.1	10.1 ± 0.2	9.4 ± 0.3	6.4 ± 0.5	−0.0 ± 0.05	PMN J0423−0120	
04 23 58	02 19		1.2 ± 0.07	1.0 ± 0.1	...	...	...	−0.4 ± 0.8	GB6 J0424+0226	
04 24 48	−37 57	140	1.6 ± 0.06	1.2 ± 0.2	1.3 ± 0.1	1.4 ± 0.2	0.8 ± 0.3	−0.3 ± 0.3	PMN J0424−3756	
04 24 51	00 36	109	1.6 ± 0.09	1.8 ± 0.1	1.8 ± 0.2	1.4 ± 0.2	...	0.0 ± 0.3	GB6 J0424+0036	
04 28 32	−37 57		2.2 ± 0.2	1.5 ± 0.1	1.3 ± 0.1	1.3 ± 0.2	1.7 ± 0.4	−0.5 ± 0.3	PMN J0428−3756	a
04 33 12	05 21	108	2.5 ± 0.08	2.7 ± 0.1	2.6 ± 0.2	2.5 ± 0.3	3.4 ± 0.6	0.1 ± 0.2	GB6 J0433+0521	
04 40 18	−43 33	147	3.0 ± 0.07	2.9 ± 0.1	2.8 ± 0.1	2.2 ± 0.2	...	−0.2 ± 0.1	PMN J0440−4332	
04 42 49	−00 18		1.0 ± 0.08	1.0 ± 0.1	1.2 ± 0.2	...	...	0.3 ± 0.6	PMN J0442−0017	
04 49 21	−81 00	175	1.8 ± 0.06	1.8 ± 0.09	1.7 ± 0.09	1.7 ± 0.2	1.2 ± 0.3	−0.1 ± 0.2	PMN J0450−8100	
04 53 27	−28 06	131	1.5 ± 0.06	1.6 ± 0.09	...	1.3 ± 0.2	1.0 ± 0.3	−0.1 ± 0.3	PMN J0453−2807	
04 55 53	−46 17	151	3.7 ± 0.06	4.1 ± 0.1	4.0 ± 0.1	3.8 ± 0.2	1.8 ± 0.4	0.1 ± 0.1	PMN J0455−4616	
04 57 00	−23 22	128	2.7 ± 0.05	2.7 ± 0.09	2.6 ± 0.1	2.2 ± 0.2	1.6 ± 0.4	−0.1 ± 0.1	PMN J0457−2324	

TABLE 6—*Continued*

R.A.	Decl.	ID	K (Jy)	Ka (Jy)	Q (Jy)	V (Jy)	W (Jy)	α	5 GHz ID	Notes
05 01 16.............	−01 58		1.2 ± 0.08	1.2 ± 0.1	1.3 ± 0.2	1.1 ± 0.2	1.5 ± 0.5	0.1 ± 0.3	PMN J0501−0159	
05 06 57.............	−61 08	154	2.2 ± 0.05	1.9 ± 0.08	1.7 ± 0.09	1.2 ± 0.2	0.8 ± 0.2	−0.5 ± 0.2	PMN J0506−6109	a
05 13 44.............	−20 15		0.8 ± 0.05	1.1 ± 0.2	0.8 ± 0.1	0.5 ± 0.2	...	−0.1 ± 0.5	PMN J0513−2016	
05 13 58.............	−21 55	127	1.0 ± 0.05	1.0 ± 0.07	1.0 ± 0.09	0.7 ± 0.3	0.9 ± 0.3	0.0 ± 0.3	PMN J0513−2159	
05 15 05.............	−45 58		...	0.4 ± 0.1	0.9 ± 0.1	1.2 ± 0.3	...	1.4 ± 1	PMN J0515−4556	a
05 19 14.............	−05 40	116	2.3 ± 0.07	2.3 ± 0.3	1.8 ± 0.2	1.1 ± 0.3	...	−0.4 ± 0.4	...	c
05 19 42.............	−45 46	150	6.5 ± 0.06	5.2 ± 0.1	4.2 ± 0.1	2.9 ± 0.2	2.0 ± 0.4	−0.7 ± 0.08	PMN J0519−4546	a
05 23 02.............	−36 27	139	3.9 ± 0.06	3.7 ± 0.1	3.4 ± 0.1	3.4 ± 0.2	2.6 ± 0.3	−0.2 ± 0.1	PMN J0522−3628	
05 25 37.............	−48 26		1.0 ± 0.06	1.4 ± 0.09	1.5 ± 0.1	1.4 ± 0.3	...	0.7 ± 0.3	PMN J0526−4830	a
05 27 32.............	−12 40	122	1.4 ± 0.07	1.7 ± 0.1	1.4 ± 0.2	1.2 ± 0.2	...	0.0 ± 0.3	PMN J0527−1241	
05 38 52.............	−44 05	148	5.4 ± 0.06	5.7 ± 0.1	5.7 ± 0.1	5.0 ± 0.2	4.6 ± 0.4	0.0 ± 0.06	PMN J0538−4405	
05 40 46.............	−54 16	152	1.4 ± 0.06	1.5 ± 0.09	1.8 ± 0.1	1.4 ± 0.2	...	0.1 ± 0.2	PMN J0540−5418	
05 42 24.............	49 51	095	1.5 ± 0.08	1.1 ± 0.1	1.1 ± 0.2	0.6 ± 0.3	...	−0.7 ± 0.5	GB6 J0542+4951	
05 50 23.............	−57 32	153	1.3 ± 0.05	...	1.2 ± 0.1	0.8 ± 0.2	0.8 ± 0.4	−0.3 ± 0.3	PMN J0550−5732	
05 55 58.............	39 44	100	2.9 ± 0.07	2.1 ± 0.1	1.1 ± 0.2	...	...	−1.0 ± 0.4	GB6 J0555+3948	
06 00 11.............	−45 28		0.6 ± 0.07	1.1 ± 0.09	0.9 ± 0.09	0.9 ± 0.2	1.2 ± 0.4	0.4 ± 0.4	PMN J0559−4529	
06 07 08.............	67 22	091	1.1 ± 0.04	...	0.7 ± 0.1	...	...	−0.8 ± 0.7	GB6 J0607+6720	a
06 08 44.............	−22 19		1.0 ± 0.04	1.0 ± 0.07	1.0 ± 0.1	...	...	0.0 ± 0.4	PMN J0608−2220	
06 09 38.............	−15 41	126	3.7 ± 0.07	3.5 ± 0.1	3.4 ± 0.1	2.5 ± 0.3	...	−0.2 ± 0.1	PMN J0609−1542	
06 23 11.............	−64 36		0.8 ± 0.04	0.8 ± 0.05	0.9 ± 0.06	0.9 ± 0.1	0.9 ± 0.2	0.1 ± 0.2	PMN J0623−6436	
06 29 26.............	−19 57	130	1.5 ± 0.05	1.4 ± 0.08	1.6 ± 0.1	1.5 ± 0.3	...	0.0 ± 0.3	PMN J0629−1959	
06 33 47.............	−22 17	135	0.6 ± 0.07	0.8 ± 0.07	0.9 ± 0.1	1.1 ± 0.2	...	0.6 ± 0.5	PMN J0633−2223	
06 35 50.............	−75 17	167	4.7 ± 0.05	4.4 ± 0.08	4.0 ± 0.09	3.0 ± 0.2	2.6 ± 0.5	−0.3 ± 0.07	PMN J0635−7516	
06 36 29.............	−20 32	134	1.1 ± 0.06	1.1 ± 0.07	0.9 ± 0.1	...	...	−0.2 ± 0.4	PMN J0636−2041	a
06 39 46.............	73 26	087	0.8 ± 0.05	0.8 ± 0.1	1.1 ± 0.1	...	1.2 ± 0.3	0.4 ± 0.4	GB6 J0639+7324	
06 46 30.............	44 49	099	3.1 ± 0.08	2.5 ± 0.1	2.2 ± 0.1	1.8 ± 0.3	...	−0.6 ± 0.2	GB6 J0646+4451	
07 21 00.............	04 01		0.9 ± 0.08	...	0.7 ± 0.1	...	...	−0.5 ± 0.7	GB6 J0721+0406	
07 21 54.............	71 22		1.8 ± 0.06	2.0 ± 0.09	2.2 ± 0.1	1.9 ± 0.2	1.7 ± 0.2	0.2 ± 0.1	GB6 J0721+7120	
07 25 49.............	−00 49		0.9 ± 0.1	1.0 ± 0.2	1.2 ± 0.1	0.8 ± 0.3	...	0.3 ± 0.6	PMN J0725−0054	
07 27 05.............	67 48		0.6 ± 0.05	0.5 ± 0.08	0.7 ± 0.1	0.7 ± 0.3	...	0.0 ± 0.6	GB6 J0728+6748	
07 34 15.............	50 21		1.1 ± 0.07	1.3 ± 0.1	1.2 ± 0.1	1.1 ± 0.2	...	0.1 ± 0.3	GB6 J0733+5022	a
07 38 15.............	17 44	113	1.4 ± 0.08	1.4 ± 0.1	1.3 ± 0.1	1.3 ± 0.3	...	−0.1 ± 0.3	GB6 J0738+1742	
07 39 14.............	01 36	124	2.0 ± 0.07	2.1 ± 0.1	2.5 ± 0.1	2.7 ± 0.3	3.1 ± 0.7	0.3 ± 0.2	GB6 J0739+0136	
07 41 13.............	31 11	107	1.3 ± 0.07	...	0.9 ± 0.2	1.3 ± 0.4	...	−0.3 ± 0.5	GB6 J0741+3112	
07 43 38.............	−67 27	161	1.3 ± 0.05	0.8 ± 0.08	0.7 ± 0.09	1.1 ± 0.3	...	−0.8 ± 0.4	PMN J0743−6726	a
07 45 27.............	10 12	118	1.1 ± 0.09	1.0 ± 0.1	0.8 ± 0.2	...	...	−0.5 ± 0.6	GB6 J0745+1011	
07 46 02.............	−00 45		1.2 ± 0.08	1.1 ± 0.1	0.8 ± 0.1	...	...	−0.6 ± 0.6	PMN J0745−0044	
07 50 53.............	12 30	117	2.6 ± 0.08	2.5 ± 0.1	2.6 ± 0.2	1.9 ± 0.2	...	−0.1 ± 0.2	GB6 J0750+1231	
07 53 31.............	53 54		1.0 ± 0.08	0.8 ± 0.1	1.0 ± 0.3	1.0 ± 0.2	...	−0.1 ± 0.5	GB6 J0753+5353	a
07 57 00.............	09 57	120	1.5 ± 0.09	1.6 ± 0.1	1.6 ± 0.2	1.3 ± 0.4	1.2 ± 0.6	0.1 ± 0.3	GB6 J0757+0956	
08 08 18.............	−07 50	133	1.4 ± 0.07	1.5 ± 0.1	1.4 ± 0.1	1.9 ± 0.2	1.2 ± 0.4	0.1 ± 0.2	PMN J0808−0751	
08 13 30.............	48 17		1.0 ± 0.08	1.0 ± 0.1	...	1.1 ± 0.3	...	0.1 ± 0.6	GB6 J0813+4813	
08 16 23.............	−24 25	145	1.0 ± 0.06	1.1 ± 0.08	1.2 ± 0.1	0.9 ± 0.2	...	0.2 ± 0.3	PMN J0816−2421	
08 24 56.............	39 14		1.1 ± 0.09	...	1.0 ± 0.2	1.1 ± 0.4	...	−0.1 ± 0.5	GB6 J0824+3916	a
08 25 48.............	03 11	125	1.4 ± 0.08	1.6 ± 0.1	1.5 ± 0.2	1.6 ± 0.2	...	0.2 ± 0.3	GB6 J0825+0309	
08 30 58.............	24 10	112	1.5 ± 0.09	1.5 ± 0.1	1.6 ± 0.2	2.0 ± 0.3	...	0.2 ± 0.3	GB6 J0830+2410	
08 36 46.............	−20 15	144	2.8 ± 0.07	2.5 ± 0.1	2.3 ± 0.1	2.1 ± 0.2	1.1 ± 0.5	−0.3 ± 0.2	PMN J0836−2017	
08 38 12.............	58 20		...	1.1 ± 0.09	1.0 ± 0.1	...	...	−0.6 ± 2	GB6 J0837+5825	a
08 40 38.............	13 12	121	1.8 ± 0.08	2.2 ± 0.1	1.8 ± 0.2	1.3 ± 0.3	...	−0.0 ± 0.3	GB6 J0840+1312	
08 41 23.............	70 53	089	1.7 ± 0.06	1.8 ± 0.1	1.8 ± 0.1	1.5 ± 0.2	...	0.0 ± 0.2	GB6 J0841+7053	
08 54 46.............	20 05	115	3.8 ± 0.09	4.5 ± 0.1	4.2 ± 0.2	4.2 ± 0.3	3.6 ± 0.5	0.1 ± 0.1	GB6 J0854+2006	
09 02 16.............	−14 14		1.1 ± 0.07	1.2 ± 0.1	1.3 ± 0.1	...	1.8 ± 0.4	0.3 ± 0.3	PMN J0902−1415	
09 07 54.............	−20 17		1.2 ± 0.06	1.0 ± 0.1	...	...	...	−0.5 ± 0.7	PMN J0907−2026	
09 09 17.............	01 18	132	1.9 ± 0.08	1.9 ± 0.1	1.8 ± 0.2	1.6 ± 0.3	...	−0.1 ± 0.3	GB6 J0909+0121	
09 09 56.............	42 52		0.9 ± 0.1	1.1 ± 0.2	1.2 ± 0.2	1.0 ± 0.2	...	0.2 ± 0.6	GB6 J0909+4253	
09 14 42.............	02 49		1.3 ± 0.07	1.6 ± 0.1	1.4 ± 0.2	...	1.6 ± 0.6	0.2 ± 0.4	GB6 J0914+0245	
09 18 11.............	−12 03	143	2.0 ± 0.08	1.1 ± 0.2	1.0 ± 0.2	...	...	−1.4 ± 0.7	PMN J0918−1205	
09 20 40.............	44 40		1.2 ± 0.09	1.1 ± 0.2	1.3 ± 0.1	1.4 ± 0.4	...	0.2 ± 0.4	GB6 J0920+4441	
09 21 07.............	62 16		0.9 ± 0.06	...	0.9 ± 0.2	...	1.3 ± 0.6	0.2 ± 0.6	GB6 J0921+6215	
09 21 40.............	−26 19		1.2 ± 0.08	1.3 ± 0.1	1.2 ± 0.1	1.2 ± 0.2	1.8 ± 0.7	0.0 ± 0.3	PMN J0921−2618	
09 27 05.............	39 01	105	6.5 ± 0.09	5.5 ± 0.1	5.2 ± 0.1	4.4 ± 0.3	2.4 ± 0.4	−0.4 ± 0.09	GB6 J0927+3902	
09 48 58.............	40 37	104	1.4 ± 0.07	1.7 ± 0.1	1.4 ± 0.1	1.1 ± 0.2	...	0.0 ± 0.3	GB6 J0948+4039	
09 55 53.............	69 36	088	1.3 ± 0.07	1.1 ± 0.09	1.1 ± 0.1	1.0 ± 0.2	0.8 ± 0.4	−0.3 ± 0.3	GB6 J0955+6940	
09 57 24.............	55 26		0.9 ± 0.08	0.8 ± 0.1	1.0 ± 0.1	...	...	0.0 ± 0.5	GB6 J0957+5522	a
09 58 07.............	47 21	098	1.5 ± 0.07	1.5 ± 0.1	1.4 ± 0.1	...	...	−0.1 ± 0.3	GB6 J0958+4725	
10 14 19.............	23 04	119	1.2 ± 0.08	1.0 ± 0.1	0.9 ± 0.2	...	...	−0.4 ± 0.6	GB6 J1014+2301	

TABLE 6—*Continued*

R.A.	Decl.	ID	K (Jy)	Ka (Jy)	Q (Jy)	V (Jy)	W (Jy)	α	5 GHz ID	Notes
10 18 50	−31 29		0.9 ± 0.06	. . .	. . .	1.0 ± 0.4	. . .	0.1 ± 0.9	PMN J1018−3123	
10 32 38	41 18	103	1.1 ± 0.07	1.0 ± 0.1	0.9 ± 0.2	1.5 ± 0.6	. . .	−0.1 ± 0.5	GB6 J1033+4115	
10 37 20	−29 34		1.3 ± 0.07	1.3 ± 0.1	1.1 ± 0.1	1.5 ± 0.3	1.0 ± 0.4	−0.0 ± 0.3	PMN J1037−2934	
10 38 42	05 11	142	1.8 ± 0.08	1.8 ± 0.1	1.5 ± 0.2	1.6 ± 0.3	. . .	−0.2 ± 0.3	GB6 J1038+0512	
10 41 25	06 11		1.2 ± 0.1	1.5 ± 0.2	1.4 ± 0.2	1.1 ± 0.3	. . .	0.1 ± 0.5	GB6 J1041+0610	
10 41 37	−47 40	163	1.1 ± 0.06	0.8 ± 0.1	0.3 ± 0.1	. . .	. . .	−1.2 ± 0.8	PMN J1041−4740	
10 47 24	71 43	083	1.0 ± 0.08	0.9 ± 0.1	0.8 ± 0.1	0.7 ± 0.3	. . .	−0.3 ± 0.5	GB6 J1048+7143	
10 47 53	−19 11		1.1 ± 0.07	1.0 ± 0.1	0.8 ± 0.2	1.1 ± 0.3	. . .	−0.3 ± 0.5	PMN J1048−1909	
10 58 28	01 34	149	4.5 ± 0.07	4.5 ± 0.1	4.5 ± 0.2	4.3 ± 0.3	3.1 ± 1	−0.0 ± 0.1	GB6 J1058+0133	
10 59 28	−80 03	176	1.9 ± 0.06	2.2 ± 0.09	2.2 ± 0.1	2.5 ± 0.2	. . .	0.3 ± 0.2	PMN J1058−8003	
11 02 03	−44 00		0.6 ± 0.05	0.9 ± 0.08	. . .	0.5 ± 0.2	. . .	0.5 ± 0.6	PMN J1102−4404	
11 07 13	−44 46	166	1.6 ± 0.05	1.5 ± 0.07	1.2 ± 0.09	1.5 ± 0.2	1.0 ± 0.4	−0.2 ± 0.2	PMN J1107−4449	
11 17 47	−46 35		1.0 ± 0.04	0.7 ± 0.07	0.6 ± 0.1	. . .	. . .	−1.0 ± 0.5	PMN J1118−4634	
11 18 50	12 38		1.0 ± 0.08	. . .	1.1 ± 0.2	1.0 ± 0.3	. . .	0.1 ± 0.5	GB6 J1118+1234	
11 27 03	−18 58	159	1.5 ± 0.07	1.4 ± 0.1	1.3 ± 0.1	. . .	. . .	−0.2 ± 0.4	PMN J1127−1857	
11 30 14	−14 52	157	1.5 ± 0.08	1.5 ± 0.1	1.5 ± 0.2	1.3 ± 0.3	. . .	−0.1 ± 0.3	PMN J1130−1449	
11 30 45	38 13	101	1.3 ± 0.07	1.2 ± 0.1	1.1 ± 0.1	1.0 ± 0.2	. . .	−0.3 ± 0.4	GB6 J1130+3815	a
11 46 15	−48 38		0.7 ± 0.05	0.6 ± 0.1	. . .	. . .	. . .	−0.4 ± 1	PMN J1145−4836	a
11 46 40	40 01		0.9 ± 0.07	0.9 ± 0.1	1.1 ± 0.1	. . .	1.5 ± 0.5	0.4 ± 0.4	GB6 J1146+3958	a
11 47 09	−38 11	169	1.9 ± 0.07	2.1 ± 0.1	1.9 ± 0.1	1.8 ± 0.2	. . .	−0.0 ± 0.2	PMN J1147−3812	
11 49 45	−79 32		1.2 ± 0.05	. . .	0.7 ± 0.3	. . .	. . .	−0.9 ± 2	PMN J1147−7936	
11 53 16	49 31	090	2.0 ± 0.05	2.0 ± 0.08	2.2 ± 0.1	1.9 ± 0.2	1.6 ± 0.3	0.0 ± 0.2	GB6 J1153+4931	a
11 54 46	81 04	078	1.0 ± 0.07	0.9 ± 0.1	. . .	1.2 ± 0.5	. . .	0.0 ± 0.7	1Jy 1150+81	
11 59 37	29 14	111	2.0 ± 0.07	2.2 ± 0.1	2.0 ± 0.1	2.0 ± 0.3	1.5 ± 0.6	0.0 ± 0.2	GB6 J1159+2914	
12 03 21	48 06		0.8 ± 0.05	0.8 ± 0.07	0.7 ± 0.1	0.6 ± 0.2	. . .	−0.3 ± 0.4	GB6 J1203+4803	a
12 08 59	−24 05	172	1.3 ± 0.07	. . .	0.9 ± 0.1	. . .	. . .	−0.7 ± 0.7	PMN J1209−2406	
12 15 54	−17 30	173	1.5 ± 0.08	1.4 ± 0.1	1.2 ± 0.1	. . .	. . .	−0.4 ± 0.4	PMN J1215−1731	
12 18 55	48 32		0.8 ± 0.04	0.8 ± 0.06	0.8 ± 0.09	0.8 ± 0.2	. . .	−0.1 ± 0.4	GB6 J1219+4830	
12 19 20	05 48	164	2.6 ± 0.07	2.2 ± 0.1	2.0 ± 0.2	1.5 ± 0.3	. . .	−0.5 ± 0.2	GB6 J1219+0549A	a
12 22 54	−83 07	178	1.0 ± 0.05	1.0 ± 0.1	0.9 ± 0.09	0.9 ± 0.3	. . .	−0.1 ± 0.4	PMN J1224−8312	
12 27 51	11 24		. . .	. . .	0.5 ± 0.2	0.5 ± 0.2	. . .	−0.0 ± 4	GB6 J1228+1124	
12 29 06	02 03	170	19.1 ± 0.08	17.3 ± 0.1	15.7 ± 0.1	13.1 ± 0.3	8.5 ± 0.4	−0.4 ± 0.03	GB6 J1229+0202	
12 30 50	12 23	165	19.1 ± 0.07	15.5 ± 0.1	13.1 ± 0.1	9.3 ± 0.3	5.9 ± 0.5	−0.6 ± 0.03	GB6 J1230+1223	
12 31 09	13 51		0.2 ± 0.1	. . .	. . .	0.7 ± 0.3	. . .	1.1 ± 1	GB6 J1231+1344	
12 46 52	−25 47	177	1.3 ± 0.08	1.5 ± 0.2	1.8 ± 0.2	1.1 ± 0.2	1.3 ± 0.5	0.2 ± 0.3	PMN J1246−2547	
12 56 11	−05 47	181	17.1 ± 0.08	17.9 ± 0.1	18.0 ± 0.1	16.6 ± 0.3	13.1 ± 0.5	0.0 ± 0.03	PMN J1256−0547	
12 58 06	−31 58	180	1.5 ± 0.07	1.2 ± 0.1	1.3 ± 0.2	. . .	. . .	−0.4 ± 0.4	PMN J1257−3154	
12 58 55	−22 23		1.0 ± 0.08	0.9 ± 0.1	1.0 ± 0.2	. . .	. . .	−0.1 ± 0.7	PMN J1258−2219	
13 02 49	48 56		. . .	. . .	0.9 ± 0.07	. . .	1.1 ± 0.4	0.2 ± 0.9	. . .	
13 05 54	−49 28		1.1 ± 0.06	1.1 ± 0.1	. . .	0.9 ± 0.2	. . .	−0.1 ± 0.5	PMN J1305−4928	
13 09 25	11 55		1.0 ± 0.07	0.9 ± 0.1	1.0 ± 0.1	1.2 ± 0.3	. . .	0.1 ± 0.4	GB6 J1309+1154	
13 10 35	32 21	052	2.9 ± 0.07	3.0 ± 0.1	2.7 ± 0.1	2.4 ± 0.2	2.1 ± 0.6	−0.1 ± 0.1	GB6 J1310+3220	
13 16 05	−33 37	182	1.5 ± 0.07	1.6 ± 0.1	1.7 ± 0.1	1.7 ± 0.2	1.7 ± 0.4	0.1 ± 0.2	PMN J1316−3339	
13 24 29	−10 46		0.9 ± 0.09	0.9 ± 0.1	1.0 ± 0.1	1.4 ± 0.3	1.5 ± 0.6	0.4 ± 0.4	PMN J1324−1049	
13 27 25	22 12		1.0 ± 0.07	1.0 ± 0.09	0.8 ± 0.1	1.4 ± 0.5	1.1 ± 0.4	0.1 ± 0.4	GB6 J1327+2210	a
13 29 15	32 01	040	0.8 ± 0.06	. . .	0.8 ± 0.3	. . .	. . .	−0.0 ± 1	GB6 J1329+3154	
13 30 55	25 04		1.1 ± 0.07	1.1 ± 0.1	1.1 ± 0.1	. . .	. . .	−0.0 ± 0.5	GB6 J1330+2509	a
13 31 19	30 31	026	2.1 ± 0.07	1.8 ± 0.1	1.4 ± 0.1	. . .	. . .	−0.6 ± 0.3	GB6 J1331+3030	
13 32 54	02 00		1.3 ± 0.07	1.3 ± 0.1	1.1 ± 0.1	1.2 ± 0.3	0.9 ± 0.4	−0.2 ± 0.3	GB6 J1332+0200	
13 33 33	27 23		0.8 ± 0.07	0.9 ± 0.1	0.9 ± 0.1	0.7 ± 0.2	. . .	0.1 ± 0.5	GB6 J1333+2725	a
13 36 49	−33 58	185	1.9 ± 0.07	1.4 ± 0.1	1.1 ± 0.1	1.7 ± 0.4	. . .	−0.6 ± 0.3	PMN J1336−3358	
13 37 39	−12 57	188	5.9 ± 0.08	6.3 ± 0.1	6.4 ± 0.1	6.1 ± 0.2	4.1 ± 0.4	0.0 ± 0.07	PMN J1337−1257	
13 43 57	66 01		0.8 ± 0.08	0.4 ± 0.1	0.6 ± 0.1	. . .	1.4 ± 0.3	0.2 ± 0.4	GB6 J1344+6606	a
13 54 51	−10 41	197	1.7 ± 0.08	1.4 ± 0.1	1.6 ± 0.2	1.5 ± 0.3	. . .	−0.1 ± 0.3	PMN J1354−1041	
13 56 56	19 19	004	1.3 ± 0.07	1.4 ± 0.1	1.2 ± 0.1	1.5 ± 0.3	0.9 ± 0.4	−0.0 ± 0.3	GB6 J1357+1919	
13 57 04	76 44		0.7 ± 0.07	0.9 ± 0.2	0.8 ± 0.1	0.8 ± 0.2	1.3 ± 0.4	0.3 ± 0.4	. . .	d
13 57 06	−15 29		0.9 ± 0.1	. . .	1.0 ± 0.2	1.1 ± 0.3	. . .	0.1 ± 0.6	PMN J1357−1527	
14 08 53	−07 49	203	1.2 ± 0.09	1.0 ± 0.1	1.1 ± 0.2	. . .	0.9 ± 0.4	−0.2 ± 0.5	1Jy 1406−076	
14 11 16	52 16		0.8 ± 0.05	0.5 ± 0.1	. . .	. . .	. . .	−1.2 ± 1	GB6 J1411+5212	
14 19 34	54 25		0.9 ± 0.07	0.8 ± 0.1	0.9 ± 0.1	1.5 ± 0.3	1.6 ± 0.4	0.4 ± 0.3	GB6 J1419+5423	a
14 19 38	38 23	042	0.9 ± 0.05	1.1 ± 0.08	1.0 ± 0.08	1.1 ± 0.1	. . .	0.1 ± 0.3	GB6 J1419+3822	
14 20 00	27 02		0.9 ± 0.07	1.0 ± 0.09	1.1 ± 0.1	1.1 ± 0.3	. . .	0.3 ± 0.4	GB6 J1419+2706	a
14 27 31	−33 03	193	1.0 ± 0.07	1.5 ± 0.1	1.7 ± 0.2	1.6 ± 0.2	. . .	0.6 ± 0.3	PMN J1427−3306	
14 27 50	−42 06	191	3.2 ± 0.07	3.0 ± 0.1	2.9 ± 0.1	2.4 ± 0.3	. . .	−0.2 ± 0.2	PMN J1427−4206	
14 40 05	49 58		. . .	. . .	. . .	0.8 ± 0.2	1.8 ± 0.8	2.0 ± 3	GB6 J1439+4958	
14 42 56	51 56		0.9 ± 0.06	1.0 ± 0.08	0.8 ± 0.09	1.1 ± 0.2	. . .	0.1 ± 0.4	GB6 J1443+5201	
14 58 39	71 40	071	1.4 ± 0.07	1.4 ± 0.1	1.1 ± 0.1	0.9 ± 0.3	1.0 ± 0.3	−0.4 ± 0.3	GB6 J1459+7140	

TABLE 6—*Continued*

R.A.	Decl.	ID	K (Jy)	Ka (Jy)	Q (Jy)	V (Jy)	W (Jy)	α	5 GHz ID	Notes
15 04 34	10 29	006	1.8 ± 0.07	1.8 ± 0.1	1.6 ± 0.1	...	...	−0.2 ± 0.3	GB6 J1504+1029	
15 06 52	−16 44		1.4 ± 0.08	1.5 ± 0.2	1.0 ± 0.1	...	...	−0.3 ± 0.5	PMN J1507−1652	a
15 10 32	−05 48		1.1 ± 0.08	...	1.4 ± 0.2	...	...	0.4 ± 0.6	PMN J1510−0543	
15 12 46	−09 05	207	1.7 ± 0.08	1.8 ± 0.1	1.8 ± 0.2	1.9 ± 0.3	1.3 ± 0.4	0.1 ± 0.3	1Jy 1510−08	
15 14 00	−10 13		0.9 ± 0.1	0.9 ± 0.2	1.1 ± 0.2	0.8 ± 0.3	...	0.1 ± 0.6	PMN J1513−1012	
15 16 38	00 13	002	1.6 ± 0.07	1.9 ± 0.1	1.7 ± 0.1	1.5 ± 0.2	...	0.1 ± 0.2	GB6 J1516+0015	
15 17 44	−24 21	205	1.8 ± 0.08	1.8 ± 0.1	1.9 ± 0.2	1.8 ± 0.3	2.3 ± 1	0.0 ± 0.3	PMN J1517−2422	
15 40 51	14 47		1.1 ± 0.07	...	0.8 ± 0.2	1.0 ± 0.2	...	−0.2 ± 0.4	GB6 J1540+1447	
15 49 27	50 37		1.0 ± 0.07	0.8 ± 0.1	0.9 ± 0.1	0.8 ± 0.2	1.1 ± 0.3	−0.1 ± 0.3	GB6 J1549+5038	
15 49 31	02 36	005	2.2 ± 0.08	2.4 ± 0.1	2.1 ± 0.1	1.9 ± 0.3	1.9 ± 0.5	−0.1 ± 0.2	GB6 J1549+0237	
15 50 38	05 26	007	2.4 ± 0.07	2.4 ± 0.1	2.0 ± 0.1	1.9 ± 0.2	1.9 ± 0.4	−0.2 ± 0.2	GB6 J1550+0527	
15 56 13	−79 12		0.8 ± 0.07	0.4 ± 0.1	0.5 ± 0.1	...	...	−1.1 ± 1	PMN J1556−7914	
16 01 56	33 29		0.9 ± 0.06	0.8 ± 0.08	0.9 ± 0.08	0.7 ± 0.2	...	−0.1 ± 0.4	GB6 J1602+3326	
16 08 50	10 28	009	2.3 ± 0.07	2.4 ± 0.1	2.2 ± 0.1	1.9 ± 0.2	2.1 ± 0.7	−0.1 ± 0.2	GB6 J1608+1029	
16 13 41	34 12	023	3.9 ± 0.06	3.4 ± 0.1	3.3 ± 0.1	2.8 ± 0.2	1.8 ± 0.4	−0.3 ± 0.1	GB6 J1613+3412	
16 17 55	−77 16	183	2.4 ± 0.06	2.2 ± 0.09	2.0 ± 0.1	1.7 ± 0.2	...	−0.3 ± 0.2	PMN J1617−7717	
16 33 15	82 27	076	1.3 ± 0.05	1.5 ± 0.08	1.4 ± 0.1	1.4 ± 0.3	...	0.3 ± 0.3	...	e
16 35 16	38 07	033	4.2 ± 0.06	4.9 ± 0.1	4.9 ± 0.1	4.5 ± 0.2	3.9 ± 0.4	0.1 ± 0.07	GB6 J1635+3808	
16 37 27	47 14		0.8 ± 0.06	...	0.9 ± 0.1	0.7 ± 0.2	...	0.1 ± 0.4	GB6 J1637+4717	
16 38 12	57 22	056	1.3 ± 0.05	1.4 ± 0.1	1.5 ± 0.1	1.6 ± 0.2	1.2 ± 0.3	0.1 ± 0.2	GB6 J1638+5720	
16 42 39	68 53	069	1.0 ± 0.06	1.0 ± 0.1	0.9 ± 0.1	1.0 ± 0.2	0.8 ± 0.3	−0.2 ± 0.3	GB6 J1642+6856	a
16 42 56	39 48	035	6.9 ± 0.06	6.5 ± 0.1	6.0 ± 0.1	5.3 ± 0.2	4.0 ± 0.4	−0.3 ± 0.06	GB6 J1642+3948	
16 43 19	−77 12		0.8 ± 0.08	0.9 ± 0.1	0.8 ± 0.1	0.6 ± 0.2	...	0.0 ± 0.5	PMN J1644−7715	
16 48 26	41 14		...	0.8 ± 0.1	1.2 ± 0.2	...	...	1.6 ± 2	GB6 J1648+4104	
16 51 06	04 57	010	1.6 ± 0.09	1.0 ± 0.1	1.1 ± 0.2	1.0 ± 0.3	...	−0.7 ± 0.4	GB6 J1651+0459	
16 54 12	39 39	036	1.1 ± 0.05	1.2 ± 0.09	...	...	1.0 ± 0.4	0.0 ± 0.4	GB6 J1653+3945	a
16 56 57	57 06		0.6 ± 0.07	0.8 ± 0.1	0.6 ± 0.1	0.9 ± 0.2	1.0 ± 0.4	0.3 ± 0.4	GB6 J1657+5705	
16 57 54	47 49		1.0 ± 0.05	...	0.6 ± 0.09	...	...	−1.0 ± 0.6	...	f
16 58 08	07 42	013	1.1 ± 0.07	1.2 ± 0.09	1.0 ± 0.1	1.5 ± 0.5	1.2 ± 0.6	−0.0 ± 0.4	GB6 J1658+0741	
16 59 40	68 29		...	...	0.7 ± 0.09	1.0 ± 0.2	0.8 ± 0.3	0.4 ± 0.9	GB6 J1700+6830	a
17 03 40	−62 13	198	1.8 ± 0.06	1.9 ± 0.1	2.0 ± 0.1	1.7 ± 0.2	...	0.0 ± 0.2	PMN J1703−6212	
17 07 39	01 47		0.9 ± 0.08	0.9 ± 0.1	0.9 ± 0.1	0.7 ± 0.2	...	−0.0 ± 0.5	GB6 J1707+0148	
17 16 02	68 40		0.6 ± 0.05	0.6 ± 0.07	0.7 ± 0.07	0.6 ± 0.1	...	0.1 ± 0.4	GB6 J1716+6836	
17 24 00	−65 00	196	2.3 ± 0.06	2.0 ± 0.09	1.7 ± 0.1	1.2 ± 0.2	1.2 ± 0.4	−0.5 ± 0.2	PMN J1723−6500	
17 27 17	45 30	043	1.2 ± 0.06	1.3 ± 0.09	1.1 ± 0.1	1.4 ± 0.2	1.5 ± 0.4	0.1 ± 0.2	GB6 J1727+4530	
17 34 13	38 56	038	1.1 ± 0.06	1.3 ± 0.1	1.2 ± 0.1	1.3 ± 0.2	1.1 ± 0.4	0.2 ± 0.3	GB6 J1734+3857	
17 37 11	−79 34	186	0.9 ± 0.05	1.1 ± 0.08	1.1 ± 0.09	...	...	0.3 ± 0.4	PMN J1733−7935	
17 40 11	47 39		0.8 ± 0.06	0.9 ± 0.08	1.1 ± 0.1	0.8 ± 0.2	...	0.2 ± 0.4	GB6 J1739+4738	
17 40 33	52 12	048	1.3 ± 0.06	1.2 ± 0.08	1.3 ± 0.1	1.5 ± 0.2	...	0.1 ± 0.2	GB6 J1740+5211	
17 48 57	70 06	068	0.6 ± 0.05	0.7 ± 0.06	0.9 ± 0.06	1.2 ± 0.1	...	0.7 ± 0.3	GB6 J1748+7005	
17 53 18	44 05		0.8 ± 0.07	0.6 ± 0.1	0.8 ± 0.1	...	...	−0.2 ± 0.6	GB6 J1753+4410	a
17 53 34	28 48	022	2.2 ± 0.06	2.3 ± 0.09	2.4 ± 0.1	2.6 ± 0.2	1.8 ± 0.4	0.1 ± 0.1	GB6 J1753+2847	
17 58 52	66 32	064	0.6 ± 0.02	0.6 ± 0.03	0.6 ± 0.08	0.4 ± 0.1	...	0.0 ± 0.3	GB6 J1758+6638	a
17 59 53	38 52		0.9 ± 0.06	0.9 ± 0.1	0.8 ± 0.1	...	...	−0.2 ± 0.6	GB6 J1800+3848	a
18 00 24	78 28	072	1.8 ± 0.06	1.7 ± 0.08	1.7 ± 0.1	1.6 ± 0.2	1.0 ± 0.2	−0.2 ± 0.2	1Jy 1803+78	
18 01 33	44 04		1.2 ± 0.06	1.3 ± 0.08	1.4 ± 0.1	1.3 ± 0.2	1.1 ± 0.3	0.2 ± 0.2	GB6 J1801+4404	
18 03 02	−65 07	199	1.3 ± 0.06	1.3 ± 0.09	1.5 ± 0.1	1.2 ± 0.3	0.9 ± 0.4	0.1 ± 0.3	PMN J1803−6507	
18 06 47	69 49	067	1.4 ± 0.04	1.4 ± 0.07	1.2 ± 0.08	1.5 ± 0.1	1.3 ± 0.4	−0.0 ± 0.2	GB6 J1806+6949	
18 20 04	−55 21		0.9 ± 0.08	0.6 ± 0.1	...	...	...	−0.9 ± 2	PMN J1819−5521	
18 20 05	−63 43	200	1.5 ± 0.06	1.4 ± 0.1	1.2 ± 0.1	1.2 ± 0.2	1.5 ± 0.4	−0.2 ± 0.3	PMN J1819−6345	
18 24 07	56 50	053	1.5 ± 0.05	1.4 ± 0.09	1.4 ± 0.09	1.5 ± 0.2	1.3 ± 0.4	−0.1 ± 0.2	GB6 J1824+5650	
18 29 41	48 44	046	2.6 ± 0.06	2.5 ± 0.09	2.5 ± 0.1	1.8 ± 0.2	1.6 ± 0.3	−0.2 ± 0.1	GB6 J1829+4844	
18 35 00	32 46		0.8 ± 0.07	0.9 ± 0.08	0.7 ± 0.09	...	...	−0.0 ± 0.6	GB6 J1835+3241	
18 37 29	−71 06	192	1.9 ± 0.05	1.8 ± 0.07	1.5 ± 0.08	1.2 ± 0.1	...	−0.4 ± 0.2	PMN J1837−7108	
18 40 29	79 46	073	1.2 ± 0.05	0.9 ± 0.09	1.0 ± 0.2	0.5 ± 0.2	...	−0.6 ± 0.4	1Jy 1845+79	
18 42 47	68 07	066	1.0 ± 0.04	1.2 ± 0.06	1.2 ± 0.06	0.9 ± 0.1	...	0.1 ± 0.2	GB6 J1842+6809	a
18 48 30	32 21		0.7 ± 0.06	0.9 ± 0.1	0.8 ± 0.1	1.3 ± 0.3	...	0.5 ± 0.5	GB6 J1848+3219	
18 49 34	67 05	065	1.3 ± 0.05	1.4 ± 0.08	1.4 ± 0.06	1.3 ± 0.1	1.5 ± 0.2	0.1 ± 0.2	GB6 J1849+6705	a
18 50 40	28 23	028	1.4 ± 0.05	1.2 ± 0.08	0.9 ± 0.08	0.7 ± 0.2	1.0 ± 0.5	−0.6 ± 0.3	GB6 J1850+2825	
19 02 56	31 53	034	1.3 ± 0.05	1.1 ± 0.08	0.8 ± 0.08	0.8 ± 0.2	...	−0.6 ± 0.3	GB6 J1902+3159	
19 23 30	−21 06	008	2.1 ± 0.08	2.2 ± 0.1	2.1 ± 0.1	2.5 ± 0.3	2.0 ± 0.8	0.1 ± 0.2	PMN J1923−2104	
19 27 27	61 18	059	1.1 ± 0.05	1.0 ± 0.09	1.1 ± 0.1	1.0 ± 0.2	...	−0.1 ± 0.3	GB6 J1927+6117	
19 27 37	73 57	070	3.5 ± 0.05	3.4 ± 0.08	2.9 ± 0.08	2.8 ± 0.2	2.0 ± 0.4	−0.3 ± 0.09	GB6 J1927+7357	
19 37 05	−39 56		0.7 ± 0.08	0.9 ± 0.2	1.1 ± 0.2	1.3 ± 0.3	...	0.6 ± 0.5	PMN J1937−3957	
19 38 11	−63 45		0.8 ± 0.06	0.8 ± 0.09	...	...	...	−0.1 ± 0.8	PMN J1939−6342	a
19 52 17	02 33		0.9 ± 0.09	0.6 ± 0.1	0.6 ± 0.1	...	...	−0.8 ± 0.8	GB6 J1952+0230	
19 55 35	51 32	051	...	1.1 ± 0.1	0.8 ± 0.1	1.1 ± 0.3	...	−0.3 ± 1	GB6 J1955+5131	a

TABLE 6—*Continued*

R.A.	Decl.	ID	K (Jy)	Ka (Jy)	Q (Jy)	V (Jy)	W (Jy)	α	5 GHz ID	Notes
19 58 00	−38 45	003	3.1 ± 0.08	3.3 ± 0.1	3.0 ± 0.1	2.8 ± 0.2	2.7 ± 1	−0.1 ± 0.1	PMN J1957−3845	
20 00 56	−17 49	011	1.6 ± 0.08	1.5 ± 0.1	1.6 ± 0.1	1.6 ± 0.2	2.5 ± 1	−0.0 ± 0.3	PMN J2000−1748	
20 05 57	77 55		0.7 ± 0.06	...	...	0.9 ± 0.3	1.0 ± 0.3	0.3 ± 0.4	1Jy 2007+77	
20 10 23	72 30		0.7 ± 0.08	0.9 ± 0.1	0.8 ± 0.09	1.1 ± 0.2	...	0.4 ± 0.5	GB6 J2009+7229	
20 11 17	−15 47	014	1.5 ± 0.07	1.6 ± 0.1	1.5 ± 0.2	1.1 ± 0.3	...	−0.1 ± 0.4	PMN J2011−1546	
20 22 30	61 36	063	1.5 ± 0.07	1.4 ± 0.09	1.3 ± 0.1	0.9 ± 0.2	...	−0.3 ± 0.3	GB6 J2022+6137	
20 35 03	−68 45	194	0.8 ± 0.06	0.9 ± 0.1	0.8 ± 0.1	0.7 ± 0.2	...	−0.0 ± 0.5	PMN J2035−6846	
20 35 22	10 58		0.7 ± 0.08	1.2 ± 0.2	...	1.0 ± 0.2	0.9 ± 0.4	0.3 ± 0.4	GB6 J2035+1055	
20 56 07	−47 17	208	1.7 ± 0.06	1.9 ± 0.09	1.9 ± 0.1	1.9 ± 0.2	2.4 ± 0.9	0.2 ± 0.2	PMN J2056−4714	
21 09 26	−41 14	001	1.5 ± 0.06	1.7 ± 0.1	1.2 ± 0.1	0.9 ± 0.2	1.2 ± 0.5	−0.2 ± 0.3	PMN J2109−4110	
21 09 37	35 37	049	1.0 ± 0.07	0.8 ± 0.1	0.7 ± 0.1	...	1.1 ± 0.3	−0.2 ± 0.4	GB6 J2109+3532	a
21 23 43	05 36	027	2.2 ± 0.07	1.8 ± 0.1	1.7 ± 0.1	1.5 ± 0.3	...	−0.4 ± 0.3	GB6 J2123+0535	
21 31 33	−12 06	017	2.7 ± 0.08	2.4 ± 0.1	2.3 ± 0.1	1.9 ± 0.2	...	−0.3 ± 0.2	PMN J2131−1207	
21 34 05	−01 54	020	1.9 ± 0.08	1.8 ± 0.1	1.7 ± 0.1	1.5 ± 0.3	1.1 ± 0.4	−0.2 ± 0.3	PMN J2134−0153	
21 36 37	00 42	025	4.3 ± 0.08	3.5 ± 0.1	3.0 ± 0.2	1.4 ± 0.2	1.3 ± 0.4	−0.7 ± 0.2	GB6 J2136+0041	
21 39 17	14 24	041	2.3 ± 0.07	2.2 ± 0.1	1.9 ± 0.1	1.6 ± 0.2	...	−0.3 ± 0.2	GB6 J2139+1423	
21 43 25	17 40	044	1.2 ± 0.06	1.4 ± 0.09	...	...	...	0.5 ± 0.5	GB6 J2143+1743	
21 48 05	06 57	037	7.8 ± 0.07	7.5 ± 0.1	7.2 ± 0.1	6.6 ± 0.2	5.1 ± 0.5	−0.2 ± 0.06	GB6 J2148+0657	
21 48 49	−77 57	184	1.4 ± 0.05	1.3 ± 0.09	...	...	...	−0.3 ± 0.5	PMN J2146−7755	
21 51 45	−30 26		1.0 ± 0.07	1.2 ± 0.1	1.2 ± 0.1	1.5 ± 0.2	1.0 ± 0.5	0.3 ± 0.3	PMN J2151−3028	
21 57 05	−69 42	190	3.6 ± 0.06	2.9 ± 0.1	2.6 ± 0.1	2.1 ± 0.2	1.5 ± 0.7	−0.6 ± 0.1	PMN J2157−6941	
21 58 07	−15 02	018	2.0 ± 0.08	2.0 ± 0.1	1.7 ± 0.1	1.5 ± 0.3	...	−0.2 ± 0.3	PMN J2158−1501	
22 02 49	42 17	058	2.9 ± 0.06	3.0 ± 0.09	3.1 ± 0.09	2.7 ± 0.2	...	0.1 ± 0.1	GB6 J2202+4216	
22 03 20	31 46	054	2.8 ± 0.06	2.7 ± 0.1	2.2 ± 0.1	1.8 ± 0.3	1.8 ± 0.4	−0.4 ± 0.2	GB6 J2203+3145	
22 03 26	17 24	045	1.5 ± 0.08	1.7 ± 0.1	1.7 ± 0.1	1.7 ± 0.2	...	0.2 ± 0.3	GB6 J2203+1725	
22 06 09	−18 39	016	1.7 ± 0.07	1.7 ± 0.1	1.3 ± 0.1	1.5 ± 0.4	...	−0.3 ± 0.3	PMN J2206−1835	
22 07 08	−53 49		1.0 ± 0.06	0.9 ± 0.09	0.8 ± 0.1	...	...	−0.3 ± 0.6	PMN J2207−5346	
22 11 33	23 51	050	1.0 ± 0.07	...	1.4 ± 0.1	1.0 ± 0.3	...	0.5 ± 0.4	GB6 J2212+2355	
22 18 52	−03 35	030	2.4 ± 0.08	2.0 ± 0.1	2.0 ± 0.2	1.7 ± 0.2	...	−0.4 ± 0.2	PMN J2218−0335	
22 25 46	−04 56	029	4.9 ± 0.07	4.6 ± 0.1	4.1 ± 0.1	3.8 ± 0.3	5.4 ± 2	−0.2 ± 0.1	PMN J2225−0457	
22 29 41	−08 32	024	2.3 ± 0.08	2.7 ± 0.1	2.6 ± 0.2	3.2 ± 0.3	2.2 ± 0.4	0.2 ± 0.2	PMN J2229−0832	
22 29 46	−20 51		0.9 ± 0.08	0.8 ± 0.1	0.8 ± 0.1	1.1 ± 0.4	...	−0.1 ± 0.6	PMN J2229−2049	
22 32 38	11 44	047	3.0 ± 0.08	3.3 ± 0.1	3.4 ± 0.1	3.7 ± 0.3	2.8 ± 0.3	0.1 ± 0.1	GB6 J2232+1143	
22 35 12	−48 34	206	1.7 ± 0.06	1.9 ± 0.1	1.8 ± 0.1	1.9 ± 0.2	2.1 ± 0.5	0.1 ± 0.2	PMN J2235−4835	
22 36 18	28 25	057	1.2 ± 0.08	1.3 ± 0.1	1.1 ± 0.1	...	...	−0.0 ± 0.4	GB6 J2236+2828	
22 39 39	−57 00	201	1.1 ± 0.05	1.3 ± 0.07	...	...	...	0.5 ± 0.4	PMN J2239−5701	
22 46 13	−12 10	021	1.2 ± 0.07	1.2 ± 0.2	1.1 ± 0.2	1.0 ± 0.4	...	−0.2 ± 0.6	PMN J2246−1206	
22 54 00	16 08	055	7.0 ± 0.07	6.7 ± 0.1	6.8 ± 0.1	6.3 ± 0.2	5.6 ± 0.5	−0.1 ± 0.06	GB6 J2253+1608	
22 55 36	42 02		1.1 ± 0.05	0.8 ± 0.07	0.9 ± 0.2	0.5 ± 0.2	...	−0.6 ± 0.5	GB6 J2255+4202	
22 56 18	−20 11	019	0.9 ± 0.08	0.7 ± 0.1	0.8 ± 0.1	1.1 ± 0.4	...	−0.2 ± 0.6	PMN J2256−2011	
22 58 06	−27 57	012	6.7 ± 0.07	6.7 ± 0.1	6.6 ± 0.1	5.9 ± 0.3	5.2 ± 0.5	−0.1 ± 0.06	PMN J2258−2758	
23 15 57	−50 17	204	1.2 ± 0.05	1.2 ± 0.08	0.9 ± 0.09	...	...	−0.2 ± 0.3	PMN J2315−5018	
23 22 54	51 07		0.8 ± 0.06	0.7 ± 0.09	0.8 ± 0.1	...	...	−0.3 ± 0.6	GB6 J2322+5057	a
23 27 42	09 39		0.8 ± 0.08	1.3 ± 0.2	1.2 ± 0.2	0.9 ± 0.3	1.1 ± 0.5	0.5 ± 0.5	GB6 J2327+0940	
23 29 10	−47 32		1.4 ± 0.05	1.2 ± 0.1	1.4 ± 0.1	1.3 ± 0.2	1.2 ± 0.3	−0.1 ± 0.2	PMN J2329−4730	
23 30 52	10 56		1.0 ± 0.07	1.2 ± 0.1	1.0 ± 0.1	1.3 ± 0.5	...	0.1 ± 0.4	GB6 J2330+1100	
23 31 19	−15 59	032	1.3 ± 0.08	0.9 ± 0.1	0.8 ± 0.2	1.1 ± 0.5	...	−0.5 ± 0.6	PMN J2331−1556	
23 33 43	−23 40		0.9 ± 0.06	0.9 ± 0.1	1.2 ± 0.2	1.2 ± 0.2	...	0.3 ± 0.4	PMN J2333−2343	a
23 34 11	07 34		1.1 ± 0.08	1.0 ± 0.1	1.1 ± 0.1	0.8 ± 0.2	...	−0.2 ± 0.4	GB6 J2334+0736	
23 35 05	−01 29		0.7 ± 0.08	1.2 ± 0.1	1.3 ± 0.1	0.7 ± 0.2	...	0.7 ± 0.6	PMN J2335−0131	
23 35 30	−52 42	195	1.0 ± 0.04	0.7 ± 0.07	0.5 ± 0.1	0.9 ± 0.3	...	−0.8 ± 0.5	PMN J2336−5236	
23 46 42	09 27		1.1 ± 0.07	1.0 ± 0.1	0.7 ± 0.1	1.0 ± 0.4	1.1 ± 0.5	−0.3 ± 0.4	GB6 J2346+0930	a
23 48 16	−16 31	039	1.8 ± 0.08	1.8 ± 0.1	2.0 ± 0.1	1.6 ± 0.2	...	0.1 ± 0.2	PMN J2348−1631	
23 54 25	45 50	074	1.6 ± 0.06	1.2 ± 0.1	1.3 ± 0.1	1.2 ± 0.2	...	−0.4 ± 0.3	GB6 J2354+4553	
23 56 21	49 52	075	0.9 ± 0.04	0.8 ± 0.07	...	...	...	−0.3 ± 0.6	...	g
23 57 54	−53 13	189	1.3 ± 0.05	1.1 ± 0.09	1.1 ± 0.1	...	0.8 ± 0.3	−0.4 ± 0.3	PMN J2357−5311	
23 58 08	−10 13		1.0 ± 0.07	1.2 ± 0.1	...	1.1 ± 0.2	...	0.2 ± 0.4	PMN J2358−1020	
23 58 52	−60 50	187	1.8 ± 0.06	1.4 ± 0.09	1.2 ± 0.09	...	...	−0.7 ± 0.3	PMN J2358−6054	

Note.—Units of right ascension are hours, minutes, and seconds, and units of declination are degrees, arcminutes, and arcseconds. Table 6 is also available in machine-readable form in the electronic edition of the *Astrophysical Journal Supplement*.

[a] Indicates the source has multiple possible identifications.

[b] Source J0322−3711 (Fornax A) is extended, and the fluxes listed were obtained by aperture photometry.

[c] Source J0519−0540 is a blend of the Lynds Bright Nebulae LBN 207.65−23.11 and LBN 207.29−22.66.

[d] Source J1357+7644 is outside of the declination range of the GB6 and PMN catalogs. Identified as QSO NVSS J135755+764320 by S. A. Trushkin (2006, private communication).

[e] Source J1633+8227 is outside of the declination range of the GB6 and PMN catalogs. It was identified as NGC 6251 by Trushkin (2003).

[f] Source J1657+4749 is identified as QSO GB6 J1658+4737 by S. A. Trushkin (2006, private communication). Offset from the *WMAP* position is 11.6′.

[g] Source J2356+4952 is identified as GB6 J2355+4950 by Trushkin (2003). Offset from the *WMAP* position is 11.9′.

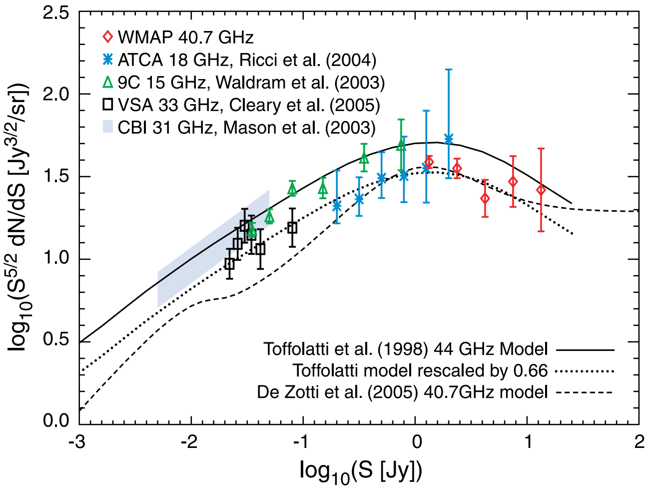

Fig. 11.—Measurement of the source number count distribution dN/dS. *Red diamonds*: From the *WMAP* 3 year point source catalog at 40.7 GHz (Q band); *stars*: from the Australian Telescope Compact Array (ATCA) 18 GHz pilot survey (Ricci et al. 2004); *triangles*: from the 9C survey at 15 GHz (Waldram et al. 2003); *squares*: from the Very Small Array (VSA) at 33 GHz (Cleary et al. 2005). The parallelogram is from the Cosmic Background Imager (CBI) experiment at 31 GHz (Mason et al. 2003). Several models for dN/dS are shown for comparison: the solid curve is the 44 GHz dN/dS model from Toffolatti et al. (1998), the dotted curve is the Toffolatti model rescaled by 0.66 (found to be a good fit to the first-year data), and the dashed curve is an updated 40.7 GHz model from de Zotti et al. (2005).

within a factor of 2 of the true beam width. We cross-correlate detected sources with the GB6, PMN, and Kühr et al. (1981) catalogs to identify 5 GHz counterparts. If a 5 GHz source is within $11'$ of the *WMAP* source position (the *WMAP* source position uncertainty is $4'$), we tag the *WMAP* source. When more than one source lies within the cutoff radius, the brightest one is assumed to be the *WMAP* counterpart.

The catalog of 323 sources obtained from the 3 year maps is listed in Table 6. In the first-year catalog, source ID numbers were assigned on the basis of position (sorted by galactic longitude). Now, rather than assigning new numbers to the newly detected sources, we recommend that WMAP sources be referred to by their coordinates, e.g., WMAP J0006−0622. For reference, we give the first-year source ID in column (3) of Table 6. The 5 GHz IDs are given in the last column. The source count distribution, dN/dS, obtained from the Q-band data is shown in Figure 11.

The first-year catalog contained 208 sources. Given the increased sensitivity in the 3 year maps, the number of new sources detected is consistent with expectations based on differential source count models. By the same token, 6 sources from the first-year catalog were dropped from the 3 year list (numbers 15, 31, 61, 96, 156, and 168). Simulations of the first-year catalog suggested that it contained 5 ± 4 false detections, so the number of dropped sources is consistent with expectations. Five of the 208 sources in the first-year catalog could not be identified with 5 GHz counterparts; now 6 out of 323 cannot be. Of the 6 sources that dropped off the first-year catalog, sources 15 and 61 did not have 5 GHz identifications. The remaining four may have dropped off because of variable (declining) flux density.

Trushkin (2003) has compiled multifrequency radio spectra and high resolution radio maps of the sources in the first-year *WMAP* catalog. Reliable identifications are claimed for 205 of the 208 sources. Of the 203 sources with optical identifications, Trushkin (2003) finds 141 quasars, 29 galaxies, 19 active galactic nuclei, 19 BL Lac–type objects and one planetary nebula, IC 418. Of the sources, 40% are identified as having flat and inverted radio spectra, 13% have GHz-peaked spectra, 8% are classical power-law sources, and 7% have a classical low-frequency power-law combined with a flat or inverted spectrum component (like 3C 84). Trushkin (2003) suggests that *WMAP* source 116 is likely to be spurious, and for source 61 no radio component was found.

6.2. *Sunyaev-Zeldovich* (*SZ*) *Effect*

Hot gas in galaxy clusters produces secondary anisotropy in the CMB via the Sunyaev-Zeldovich effect: a systematic frequency shift of CMB photons produced by Compton scattering off hot electrons in the cluster gas. At frequencies less than 217 GHz, this produces a temperature decrement in the CMB along sight lines that pass through clusters. The effect is relatively small for *WMAP* due to its moderate angular resolution; nevertheless, nearby clusters are large enough to produce a measurable effect in the sky maps. In our first-year analysis we reported detections of an SZ signal from the Coma cluster and from an aggregate sample of X-ray-selected Abell clusters, the XBAC catalog. Since then, there have been numerous additional reports of SZ signal detection in the first-year *WMAP* data (Fosalba & Gaztañaga 2004; Fosalba et al. 2003; Myers et al. 2004; Afshordi et al. 2004, 2005; Hernández-Monteagudo et al. 2004; Hernández-Monteagudo & Rubiño-Martín 2004; Hansen et al. 2005; Atrio-Barandela & Muecket 2006). In this section, we update our results for the Coma cluster and the XBAC catalog; in subsequent cosmological studies, we mask these clusters from the data.

The brightest SZ source is the Coma cluster. For SZ analysis we model its temperature profile with an isothermal β-model of the form

$$\Delta T_{\rm SZ}(\theta) = \Delta T_{\rm SZ}(0)\left[1 + (\theta/\theta_c)^2\right]^{(1-3\beta)/2}, \qquad (28)$$

where $\theta = r/D_A(z)$ is the angular distance from the core, located at $(l, b) = (56.75°,\ 88.05°)$; Briel et al. (1992) give $\theta_c = 10.5' \pm 0.6'$ and $\beta = 0.75 \pm 0.03$. Using these values, we convolve the profile with the *WMAP* beam response at each frequency (Page et al. 2003a; Jarosik et al. 2007) and fit for $\Delta T_{\rm SZ}(0)$ by minimizing

$$\chi^2 = \sum_{ij} [T_i - T_0 - \Delta T_{\rm SZ}(\theta_i)](\boldsymbol{M}^{-1})_{ij} \times \left[T_j - T_0 - \Delta T_{\rm SZ}(\theta_j)\right], \qquad (29)$$

where T_i is the temperature in pixel i, T_0 is a temperature baseline, θ_i is the angular distance of pixel i from the cluster core, and $\boldsymbol{M}_{ij}$ is the pixel-pixel covariance matrix of the sky map. We model $\boldsymbol{M}_{ij}$ as $C(\hat{n}_i \cdot \hat{n}_j) + \sigma_i^2\delta_{ij}$, where $C(\theta)$ is the two-point correlation function of the CMB and σ_i^2 is the variance due to instrument noise in pixel i.

For the W band we find a Coma decrement of $\Delta T_{\rm SZ}(0) = -0.46 \pm 0.16$ mK, with a reduced χ^2 of 1.05 for 196 degrees of freedom. In the V band the decrement is -0.31 ± 0.16 mK. Herbig et al. (1995) measured a Rayleigh-Jeans decrement of -0.51 ± 0.09 mK at 32 GHz. Given the SZ frequency spectrum, their result predicts -0.47 ± 0.08 mK at the V band and -0.42 ± 0.07 mK at the W band, consistent with what we observe.

The XBAC catalog of X-ray clusters produced by Ebeling et al. (1996) is an essentially complete flux-limited sample of 242 Abell clusters selected from the *ROSAT* All-Sky Survey data. We cross-correlate this catalog with the *WMAP* 94 GHz map. Treating the XBAC clusters as point sources, we estimate their flux density at 94 GHz using the expression from Refregier et al. (2000)

$$S_{94} = 11.44\left[\frac{300\ \mathrm{Mpc}}{D(z)}\right]^2\left(\frac{f_{\mathrm{gas}}}{0.11}\right)\left(\frac{kT_e}{1\ \mathrm{keV}}\right)^{5/2}\quad [\mathrm{mJy}], \quad (30)$$

where $D(z)$ is the angular diameter distance to the cluster, $f_{\mathrm{gas}} \equiv M_{\mathrm{gas}}/M$ is the gas mass fraction, and T_e is the electron temperature. The overall normalization of this relation is uncertain due to our ignorance of the correct gas fraction and cluster virialization state. We fix $f_{\mathrm{gas}} = 0.11$. Extended clusters (more than one-third the extent of Coma) are omitted; the remaining fluxes are all <1 Jy. A template map is constructed by convolving the clusters with the *WMAP* W-band beam response (Page et al. 2003a) and fitting the result to the *WMAP* 94 GHz map. We find a template normalization of -0.32 ± 0.14 for the 3 year data (compared to -0.36 ± 0.14 in the first-year data). Since the fluxes used to construct the template are positive, the negative scaling is consistent with a 2.5 σ SZ decrement.

CMB photons that travel to us through the plane of the Milky Way undergo an SZ distortion of $y \approx kn_eT_e\sigma_{\mathrm{T}}L/m_ec^2$, where σ_{T} is the Thomson scattering cross-section and L is the electron-pressure-weighted path length through our Galaxy. Taking $n_eT_e = 10^3$ K cm^{-3} and $L = 50$ kpc, we find $y \approx 2\times10^{-8}$; thus our Galaxy does not significantly affect CMB photons. The SZ effect can safely be ignored as a diffuse contaminating foreground signal.

7. THE ANGULAR POWER SPECTRUM

Full-sky maps provide the most compact record of CMB anisotropy without loss of information. They permit a wide variety of statistics to be computed from the data, the most fundamental of which is the CMB angular power spectrum. Indeed, if the temperature fluctuations are Gaussian distributed, with random phase, the angular power spectrum provides a *complete* description of the statistical properties of the CMB. While there have been a number of papers based on the first-year data that claim evidence of non-Gaussianity and/or nonrandom phases in the fluctuations (see below), it is clear that the fluctuations are not *strongly* deviant from Gaussian, random phase. Thus, the measured power spectrum does provide the primary point of contact between data and cosmological parameters. This section presents the angular power spectrum obtained from the first 3 years of *WMAP* observations.

A sky map $T(\boldsymbol{n})$ defined over the full sky may be decomposed in spherical harmonics as

$$T(\boldsymbol{n}) = \sum_{l=0}^{\infty}\sum_{m=-l}^{l} a_{lm}Y_{lm}(\boldsymbol{n}) \quad (31)$$

with

$$a_{lm} = \int d\boldsymbol{n}\, T(\boldsymbol{n})Y^*_{lm}(\boldsymbol{n}), \quad (32)$$

where $\boldsymbol{n}$ is a unit direction vector. If the CMB anisotropy is Gaussian distributed with random phases, then each a_{lm} is an independent Gaussian deviate with $\langle a_{lm}\rangle = 0$, and

$$\langle a_{lm}a^*_{l'm'}\rangle = \delta_{ll'}\delta_{mm'}C_l, \quad (33)$$

where C_l is the angular power spectrum and δ is the Kronecker symbol. Here C_l is the mean variance per l that would be observed by a hypothetical ensemble of observers distributed throughout the universe. The actual power spectrum observed in *our* sky, by a supposedly typical member of this ensemble, would be

$$C_l^{\mathrm{sky}} = \frac{1}{2l+1}\sum_{m=-l}^{l}|a_{lm}|^2. \quad (34)$$

If we had noiseless CMB data over the full sky, equation (32) could be evaluated exactly and equation (34) would give an unbiased estimate of the true power spectrum, in the sense that $\langle C_l^{\mathrm{sky}}\rangle = C_l$ when averaged over the ensemble. However, we do not have ideal data (see below), and even if we did, since we only measure $2l + 1$ modes per l (per sky), the above estimate of the variance has an intrinsic uncertainty (or "cosmic variance") of

$$\frac{\sigma_l}{C_l} = \sqrt{\frac{2}{2l+1}}. \quad (35)$$

Beyond cosmic variance, there are two effects that preclude using equations (32) and (34) to estimate the power spectrum; (1) real CMB data contains noise and other sources of error that cause the quadratic expression in equation (34) to be biased; and (2) data near the Galactic plane must be masked because Galactic emission cannot be reliably cleaned there. Masking precludes the proper evaluation of the integral in equation (32), so other methods must be found to estimate a_{lm} and C_l.

In the first-year analysis, we addressed problem (1) by adopting a "cross-power" estimator in which we replace $|a_{lm}|^2$ by $(a^i_{lm}a^{j*}_{lm})$, where i and j denote data channels with uncorrelated noise (Hinshaw et al. 2003b; see also Polenta et al. 2005; Patanchon 2003; Tristram et al. 2005). This form removes the noise bias from the estimate of $|a_{lm}|^2$. We addressed problem (2) by using a "pseudo-C_l" estimator (Peebles & Hauser 1974; Hivon et al. 2002) that statistically corrects for the aliasing introduced by nonuniform pixel weights, of which the sky cut is an extreme case.

An alternative approach is to invoke a maximum likelihood estimator that employs Bayes' theorem to relate the likelihood of the power spectrum to the likelihood of the data,

$$L(C_l|\boldsymbol{d}) \propto L(\boldsymbol{d}|C_l)P(C_l). \quad (36)$$

Here $L(C_l|\boldsymbol{d})$ is the likelihood of the model (the underlying power spectrum, C_l) given the data $\boldsymbol{d}$ (usually a sky map, or its transform, the a_{lm} coefficients), $L(\boldsymbol{d}|C_l)$ is the likelihood of the data given the model, and $P(C_l)$ is the prior probability of the power spectrum. It is standard to assume that the data follow a multivariate Gaussian distribution (as predicted by most inflationary models, for example), in which case the likelihood takes the form

$$L(C_l|\boldsymbol{d}) \propto \frac{\exp\left[-(1/2)\boldsymbol{d}^T\boldsymbol{C}^{-1}\boldsymbol{d}\right]}{\sqrt{\det\boldsymbol{C}}}P(C_l), \quad (37)$$

where $\boldsymbol{C}$ is the covariance matrix of the data, including contributions from both signal and noise, $\boldsymbol{C}(C_l) = \boldsymbol{S}(C_l) + \boldsymbol{N}$. Since the covariance matrix includes both terms, the confidence regions on C_l deduced from $L(C_l|\boldsymbol{d})$ automatically incorporate the uncertainty from both cosmic variance and instrument noise. In addition, if the data are restricted to lie outside a Galaxy cut, the confidence regions on C_l will incorporate the uncertainty due to aliasing. Finally, it is also standard to assume a uniform prior distribution for the model, $P(C_l) = 1$, although given sufficiently robust data, this choice will be unimportant. There are many technical challenges one must overcome when evaluating equation (37), and most of these have been well covered in the literature (Peebles 1973; Peebles & Hauser 1974; Hamilton 1997a, 1997b; Tegmark 1997; Bond et al. 1998; Borrill 1999; Oh et al. 1999). See Page et al. (2007) for an extension of this methodology to a simultaneous analysis of the temperature and polarization data.

Since the *WMAP* first-year data release, several authors have rederived the angular power spectrum from the sky maps using a variety of other estimators. Some of these analyses cover the full l range to which *WMAP* is sensitive, while others restrict attention to the low l regime where certain technical issues matter most, and where hints of unusual behavior have been suggested. Of the analyses covering the full l range, Fosalba & Szapudi (2004) employ a pixel-space estimator called SpICE that produces a spectrum that agrees remarkably well with the released *WMAP* spectrum. These authors do find small discrepancies at the very highest l values (where the *WMAP* data are noise-dominated), but these differences do not significantly affect parameter determination. O'Dwyer et al. (2004) and Eriksen et al. (2004c) use a novel method based on Gibbs sampling to undertake a full Bayesian analysis of the power spectrum. This method also produces results that are in good agreement with the *WMAP* spectrum. In addition, the method is able to generate a full conditional likelihood for the spectrum that allows one to rigorously evaluate cosmological models without resorting to likelihood approximations.

Efstathiou (2004b) has surveyed a variety of methods for estimating the power spectrum of large data sets such as *WMAP* and concluded that the best approach is a hybrid one which employs a maximum likelihood estimate at low l and a pseudo-C_l based estimate at high l. We agree with this approach and adopt it for the 3 year analysis, making the transition at $l = 30$. This gives results that agree well with the first-year spectrum for $l > 30$, and reasonably well for low-l, as detailed below. In the original version of this paper, we chose to make the transition at $l = 12$, but a detailed study of the 3 year spectrum by Eriksen et al. (2007) suggested that the transition needed to be at $l \sim 30$ to avoid biasing cosmological parameter estimates, particularly the scalar spectral index, n_s. Eriksen et al. (2007) and Spergel et al. (2007) (see Appendix A) discuss the effect of this choice on the spectral index.

In the following sections we discuss the instrumental properties that are important to know for accurate power spectrum estimation, and assess the ability of the new Galactic foreground models to clean the power spectrum data. We then analyze the low- and high-l power spectrum in detail and compare the result with the previous *WMAP* spectrum and with other contemporary CMB data.

7.1. *Instrumental Properties*

The temperature measured on the sky is modified by the properties of the instrument. The most important properties that affect the angular power spectrum are finite resolution and instrument noise. Let $C_l^{iji'j'}$ denote the auto or cross-power spectrum evaluated from two sky maps, ij and $i'j'$, where ij is a composite DA/year index (i denotes the DA, j the year). Furthermore, we define the shorthand $\boldsymbol{i} \equiv (ij, i'j')$ to denote a pair of composite indices, e.g., (Q1/yr-1, V2/yr-1), (Q1/yr-1, Q1/yr-2), etc. This spectrum will have the form

$$C_l^{\boldsymbol{i}} = w_l^{\boldsymbol{i}} C_l^{\rm sky} + N_l^{\boldsymbol{i}}, \tag{38}$$

where $w_l^{\boldsymbol{i}} \equiv b_l^i b_l^{i'} p_l^2$ is the window function that describes the combined smoothing effects of the beam and the finite sky map pixel size. Here b_l^i is the beam transfer function for DA i, defined by Page et al. (2003a) and updated by Jarosik et al. (2007) [note that we reserve the term "beam window function" for $(b_l^i)^2$], and p_l is the pixel transfer function supplied with the HEALPix package (Gorski et al. 2005). The term $N_l^{\boldsymbol{i}}$ is the noise spectrum realized in this particular measurement. On average, the observed spectrum estimates the underlying power spectrum, C_l,

$$\langle C_l^{\boldsymbol{i}} \rangle = w_l^{\boldsymbol{i}} C_l + \langle N_l^i \rangle \delta_{ii'}, \tag{39}$$

where $\langle N_l^i \rangle$ is the noise bias for differencing assembly i, and the Kronecker symbol indicates that the noise is uncorrelated between differencing assemblies and between years of data. To estimate the underlying power spectrum on the sky, C_l, the effects of the noise bias and beam convolution must be removed. The ability to determine these terms accurately is a critical element of any CMB experiment design.

In § 7.1.1 we summarize the results of Jarosik et al. (2007) on the *WMAP* window functions and their uncertainties. We propagate these uncertainties through to the final Fisher matrix for the angular power spectrum. In § 7.1.2 we present a model of the *WMAP* noise properties appropriate to power spectrum evaluation. For cross-power spectra ($i \neq i'$ above), the noise bias term drops out of the signal estimate if the noise between the two DAs (or between years of data from a single DA) is uncorrelated. However, the noise bias term still enters into the error estimate, even for cross spectra. Therefore, the noise model is used primarily in error propagation.

7.1.1. *Window Functions*

The instrument beam response was mapped in flight using observations of the planet Jupiter (Jarosik et al. 2007; Page et al. 2003a). The beam widths, measured in flight, range from 0.82° (FWHM) at the K band down to 0.20° in some of the W band channels. The S/N is such that the response, relative to the peak of the beam, is measured to approximately −35 dB in the W band. As part of the 3 year analysis, we have produced a physical model of the A-side optics based on simultaneous fits to all 10 A-side beam pattern measurements (Jarosik et al. 2007). We use this model to augment the beam response data at very low S/N (−30 to −38 dB, depending on frequency band), which in turn allows us to better determine the total solid angle and window function of each A-side beam. For the B-side response, we scale the A-side model by fitting it to the B-side Jupiter measurements in the high-S/N regime. We then form similar hybrid response maps by augmenting the B-side data with the scaled model in the low-S/N regime. (We plan to update the A-side model and produce an independent B-side model in the near future.) These hybrid beam response maps are available on LAMBDA as part of the *WMAP* 3 year data release. The radial beam profiles obtained from these maps have been fit to a model consisting of a sum of Hermite polynomials that accurately characterize the main Gaussian lobe and small deviations from it. The model profiles are then Legendre transformed to obtain the beam transfer functions b_l^i for each DA i (Jarosik et al. 2007). These transfer functions are also provided with the 3 year data release.

The constraints imposed by the physical optics model have allowed us to extend the beam analysis out to much larger radii than was possible with the first-year analysis. As a result, we have determined that the beam solid angles were being systematically underestimated by ∼1%. Since we normalize the transfer functions to 1 at $l = 1$, this meant that the normalized functions were being systematically overestimated by a comparable amount for $l \gtrsim 50$. Consequently, as we discuss in § 7.6, the final 3 year power spectrum is ~1%–2% higher than the first-year spectrum for $l \gtrsim 50$. We believe this new determination of the beam response is more accurate than that given in the first-year analysis, but until we can complete the B-side model analysis, we have held the window function uncertainties at the first-year level (Page et al. 2003a). The first-year uncertainties are large enough to encompass the differences between the previous and current estimates of b_l. The propagation of random beam errors through to the power spectrum Fisher matrix is discussed in Appendix A.

An additional source of systematic error in our treatment of the beam response arises from noncircularity of the main beam (Wu et al. 2001; Souradeep & Ratra 2001; Mitra et al. 2004). The effects of noncircularity are mitigated by *WMAP*'s scan strategy, which causes most sky pixels to be observed over a wide range of azimuth angles. However, residual asymmetry in the effective beam response on the sky will, in general, bias estimates of the power spectrum at high l. In Appendix B we compute the bias induced in a cross-power spectrum due to residual beam asymmetry. In principle the formalism is exact, but in order to make the calculation tractable, we make two approximations: (1) that *WMAP*'s scan coverage is independent of ecliptic longitude, and (2) that the azimuthal structure in the *WMAP* beams is adequately described by modes up to azimuthal quantum number $m = 16$. We define the bias as the ratio of the true measured power spectrum to that which would be inferred assuming a perfectly symmetric beam,

$$\alpha_l \equiv \frac{1}{b_l^i b_l^{i'} C_l^{\rm fid}} \sum_{l'} G_{ll'}^{\boldsymbol{i}} C_{l'}^{\rm fid}, \qquad (40)$$

where $C_l^{\rm fid}$ is a fiducial power spectrum, b_l^i is the symmetrized beam transfer function noted above, and $G_{ll'}^{\boldsymbol{i}}$ is the coupling matrix, defined in Appendix B, that accounts for the full beam structure.

Plots of α_l for selected channel combinations are shown in Appendix B. These results assume 3 year sky coverage and beam multipole moments fit to the hybrid beam maps with $l_{\rm max} = 1500$ and $m_{\rm max} = 16$. As shown in the figure, the Q-band cross-power spectra (e.g., Q1 × Q2) require the greatest correction (6.3% at $l = 600$). This arises because the Q-band beams are farthest from the optic axis of the telescope and are thus the most elliptical of the three high-frequency bands; for example, the major and minor axes of the Q2A beam are 0.60° and 0.42° (FWHM), respectively. The corrections to the V- and W-band spectra are all $\lesssim$1% for $l < 1000$. Because of the relatively large bias in the Q band, and because of the potential to confuse it with the frequency-dependent point source correction, Q-band data were excluded from the final 3 year power spectrum. The remaining V- and W-band cross-power spectra were *not* corrected because the bias is already substantially smaller than the random instrument noise in the pertinent l range.

7.1.2. *Instrument Noise Properties*

The noise bias term in equation (39) is the noise per a_{lm} coefficient on the sky. If auto-power spectra are used in the final power spectrum estimate, the noise bias term must be known very accurately, because it exponentially dominates the convolved power spectrum at high l. If only cross-power spectra are used, the noise bias is only required for estimating errors. Our final combined spectrum is based only on cross-power spectra for $l > 30$, while for $l < 30$, the noise bias is negligible compared to the sky signal, so that it need not be known to high precision for the maximum likelihood estimation (see § 7.4).

In the limit that the time-domain instrument noise is white, the noise bias will be a constant, independent of l. If the noise has a $1/f$ component, the bias term will rise at low l. While the *WMAP* radiometer noise is nearly white by design, with 9 out of 10 differencing assemblies having $1/f$ knee frequencies of <10 mHz (Jarosik et al. 2003b), deviations of $\langle N_l^i \rangle$ from a constant must be accounted for, especially for the low-l polarization analysis (Page et al. 2007). In the first-year analysis, we used end-to-end Monte Carlo simulations to generate realizations of the noise bias, then fit the mean of the realizations to a parameterized model. In the present analysis we use two sets of independent single-year sky maps from each DA to form the following estimate of the noise bias,

$$\langle N_l^i \rangle = \frac{1}{2} \sum_{j,j'=1}^{2} \left[C_l^{(ij,ij)} - C_l^{(ij,ij')} \right]. \qquad (41)$$

In words, we take the difference between the auto-power spectra (years $j = j'$) and the cross-power spectra (years $j \neq j'$) for a given DA to estimate the noise bias. We then fit the estimate to a model of the form

$$\langle N_l^i \rangle = N_0 + N_1(450/l), \qquad (42)$$

where N_0 and N_1 are fit coefficients (we enforce $N_1 \geq 0$), and the fit is performed over the range $33 \leq l \leq 1024$. This model is used to compute the weights that enter into the final combined spectrum (§ 7.5) and to estimate its noise properties.

7.1.3. *Systematic Errors*

Jarosik et al. (2007) present limits on systematic errors in the 3 year sky maps. They consider the effects of absolute and relative calibration errors, artifacts induced by environmental disturbances (thermal and electrical), errors from the map-making process, pointing errors, and other miscellaneous effects. The combined uncertainty due to relative calibration errors, environmental effects, and map-making errors are limited to $<29\ \mu{\rm K}^2$ ($2\,\sigma$) in the quadrupole moment C_2 in any of the eight high-frequency DAs. We estimate the absolute calibration uncertainty in the 3 year *WMAP* data to be 0.5%.

The noise in the *WMAP* sky maps is weakly correlated from pixel to pixel due to $1/f$ noise in the radiometers, and to the map-making process that infers pixel temperatures from filtered differential data. Neglecting these correlations is a form of systematic error that must be quantified. As part of the 3 year analysis, we have developed code to compute the pixel-pixel inverse covariance matrix at pixel resolution r4. The resulting information is propagated through the computation of the Fisher matrix to estimate power spectrum uncertainties (Page et al. 2007). Sample C_l uncertainty results for single-year cross-power spectra are shown in Figure 12. The red curves show the result when pixel-pixel noise correlations are ignored. The smooth rise at low l reflects our approximate representation of $1/f$ noise in the noise bias model, equation (42). The black curves account for the full structure of the pixel-pixel inverse covariance matrix, including $1/f$ noise and map-making covariance. For the TT spectrum (left pair of curves in each panel), the noise is negligible compared to the signal ($\sim$1000 $\mu{\rm K}^2$), so this structure can be safely ignored.

Random pointing errors are accounted for in the beam mapping procedure; the beam transfer functions presented in Jarosik et al. (2007) incorporate random pointing errors automatically. A systematic pointing error of $\sim 1'$ at the spin period is suspected in the quaternion solution that defines the spacecraft pointing. This

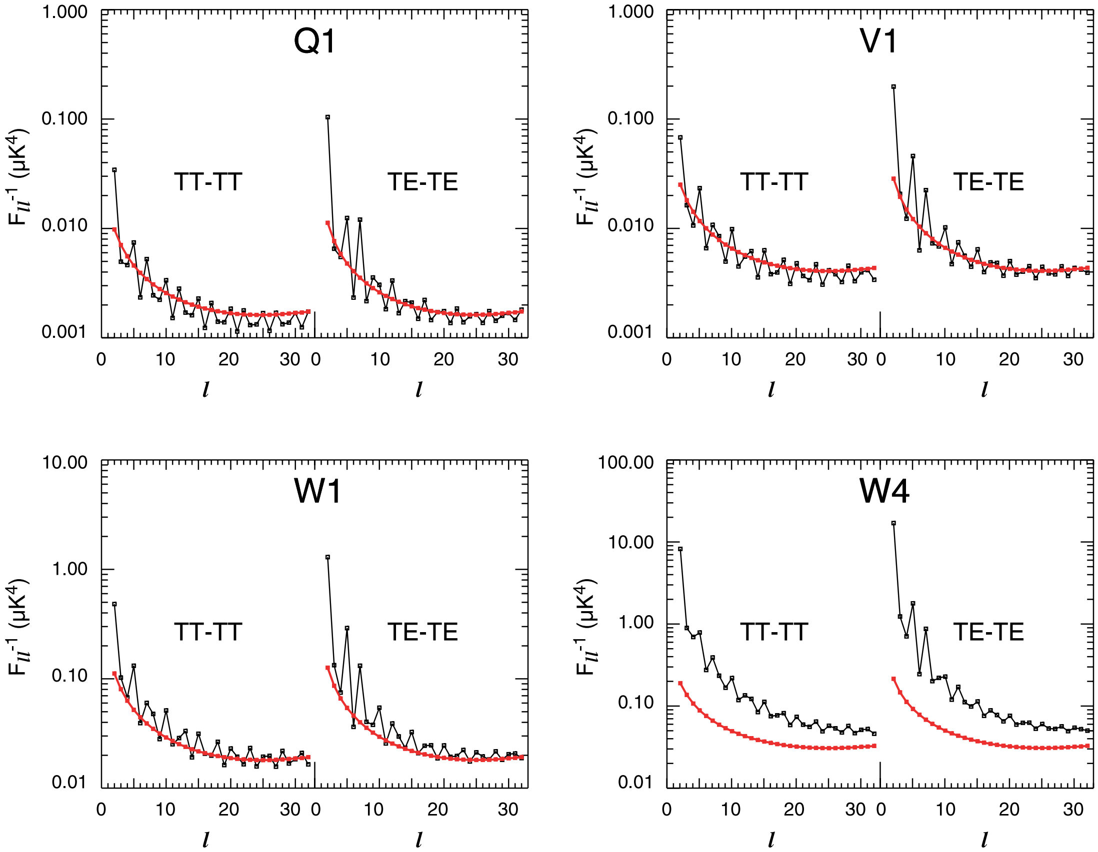

Fig. 12.— Predicted C_l uncertainty (inverse Fisher matrix) at low l, in μK^4. The red curves show the result when pixel-pixel noise correlations are ignored. The smooth rise at low l reflects our approximate representation of 1/f noise in the noise bias model, eq. (42). The black curves account for the full structure of the pixel-pixel inverse covariance matrix, including 1/f noise and map-making covariance. For the TT spectrum (left pair of curves in each panel), the noise is negligible compared to the signal, so this structure can be safely ignored. However, the TE analysis must account for it (Page et al. 2007). See Fig. 16 of Page et al. (2007) for an analogous plot of the EE and BB uncertainties.

is much smaller than the smallest beam width ($\sim 12'$ at the W band), and we estimate that it would produce $<1\%$ error in the angular power spectrum at $l = 1000$; thus we do not attempt to correct for this effect. Barnes et al. (2003) place limits on spurious contributions due to stray light pickup through the far-sidelobes of the instrument. As shown in Figure 4 of that paper, they place limits of $<10\ \mu K^2$ on spurious contributions to $l(l+1)C_l/2\pi$, at the Q through W bands, due to far-sidelobe pickup.

Our template-based approach to Galactic foreground subtraction is detailed in § 5.3; the effect of this frequency-by-frequency cleaning on the power spectra is shown in § 7.2. Diffuse foreground emission is a modest source of contamination at large angular scales ($\gtrsim 2°$). Systematic errors on these angular scales are negligible compared to the (modest) level of foreground emission. On intermediate angular scales ($\lesssim 2°$), the 1%–2% uncertainty in the beam transfer functions is the largest source of uncertainty, while for multipole moments greater than ~ 400, random white noise from the instrument is the largest source of uncertainty.

7.2. *Galactic and Extragalactic Foregrounds*

In this subsection we determine the level of foreground contamination in the angular power spectrum. On large angular scales ($l \lesssim 50$), the primary source of contamination is diffuse emission from the Milky Way, while on small scales ($l \gtrsim 400$) the primary culprit is extragalactic point-source emission. To simplify the discussion, we present foreground results using the pseudo-C_l estimate of the power spectra over the entire l-range under study, despite the fact that we use a maximum likelihood estimate for the final low-l power spectrum. Thus, while the low-l estimates presented in the section may not be optimal, they are consistently applied as a function of frequency, so that the relative foreground contamination is reliably determined.

Figure 13 shows the cross-power spectra obtained from the high-frequency band maps (Q–W) prior to any foreground subtraction. All DA/yr combinations within a band pair were averaged to form these spectra, and the results are color coded by effective frequency, $(\nu^i \nu^{i'})^{1/2}$, where ν^i is the frequency of differencing assembly i. As indicated in the plot legend, the low-frequency data are shown in red, and so forth. To clarify the result, we plot the ratio of each frequency band spectrum to the final combined spectrum (see § 7.5). The red trace in the top panel shows very clearly that the low-frequency data are contaminated by diffuse Galactic emission at low l and by point sources at higher l. The contamination appears to be least at the highest frequencies, as expected in this frequency range. This is consistent with the dominance of synchrotron and free-free emission over thermal dust emission.

Not surprisingly, the most contaminated multipoles are $l = 2$ and 4, which most closely trace the Galactic plane morphology. Specifically, the total quadrupolar emission at the Q band is nearly 10 times brighter (in power units) than the CMB signal, while at the W band it is nearly 5 times brighter. The foreground emission reaches a minimum near the V band, where the total $l = 2$ emission is less than a factor of 2 brighter than the CMB, and even less for $l > 2$. Note also the modest foreground features in the range $l \sim 10$–30.

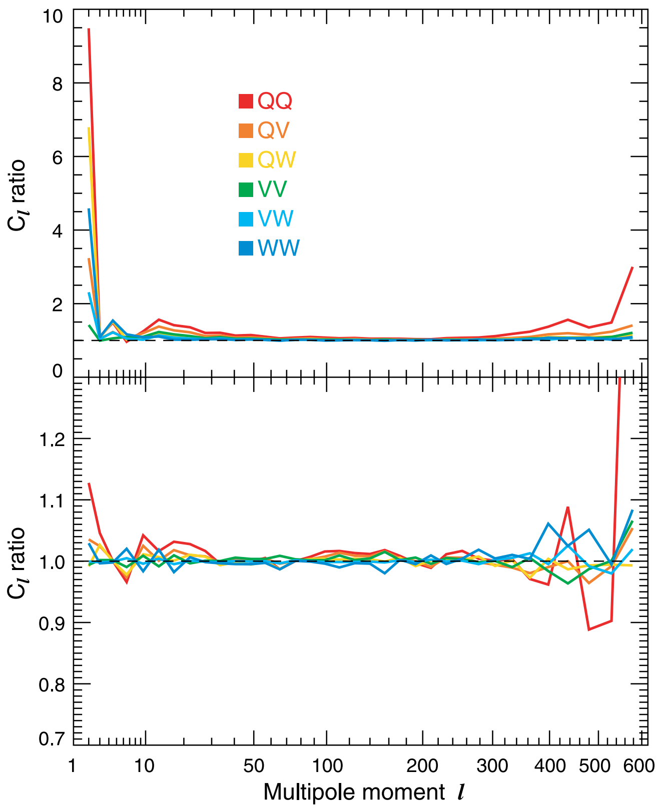

Fig. 13.—*Top*: Q-, V-, and W-band cross-power spectra before foreground subtraction, evaluated outside the Kp2 sky cut, relative to the final combined spectrum. *Bottom*: Same cross-power spectra after subtracting a template-based diffuse foreground model (§ 5.3) and the best-fit residual point source contamination (§ 7.2).

The contribution from extragalactic radio sources can be seen in Figure 13 as excess emission in the Q band at high l. As discussed in § 6.1, we performed a direct search for sources in the *WMAP* data and found 323. Based on this search, we augmented the mask we use for CMB analysis, so the contribution shown in the figure is mostly due to sources just below our detection threshold. In the limit that these sources are not clustered, their contribution to the cross-power spectra has the form

$$C_l^{\boldsymbol{i},\,\mathrm{src}} = A\, g_i g_{i'} \left(\frac{\nu_i}{\nu_{\mathrm{Q}}}\right)^{\beta} \left(\frac{\nu_{i'}}{\nu_{\mathrm{Q}}}\right)^{\beta} w_l^{\boldsymbol{i}}, \tag{43}$$

where A is an overall amplitude, measured antenna temperature, the factors g_i convert the result to thermodynamic temperature, $\nu_{\mathrm{Q}} \equiv 40.7$ GHz (note that this differs from our first-year definition of 45 GHz), and we assume a frequency spectrum $\beta = -2.0$. The amplitude A is determined by fitting to the Q-, V-, and W-band cross-power spectra. Following the procedure outlined in Appendix B of Hinshaw et al. (2003b) we find $A = 0.014 \pm 0.003$ $\mu\mathrm{K}^2$ sr, in antenna temperature. (As discussed below, this value has been revised down from 0.017 ± 0.002 $\mu\mathrm{K}^2$ sr since the original version of this paper appeared.) In the first-year analysis we found $A = 0.022$ $\mu\mathrm{K}^2$ sr (0.015 $\mu\mathrm{K}^2$ sr, referred to 45 GHz). The 3 year source amplitude is expected to be lower than the first-year value due to the enlargement of the 3 year source mask and the consequent lowering of the effective flux cut applied to the source population. Spergel et al. (2007) evaluate the bispectrum of the *WMAP* data and are able to fit a non-Gaussian source component to a particular configuration of the bispectrum data. They find the source model, equation (43), fits that data as well. We thus adopt the model given above with $A = 0.014$ $\mu\mathrm{K}^2$ sr and use the procedure given in Appendix A to marginalize the over the uncertainty in A. At the Q band, the correction to $l(l+1)C_l/2\pi$ is 608 and 2431 $\mu\mathrm{K}^2$ at $l = 500$ and 1000, respectively. At the W band, the correction is only 32 and 128 $\mu\mathrm{K}^2$ at the same l values. For comparison, the CMB power in this l range is $\sim$2000 $\mu\mathrm{K}^2$.

Since the release of the 3 year data, Huffenberger et al. (2006) have reanalyzed the multifrequency spectra for residual sources using a similar methodology. They find a somewhat smaller amplitude of 0.011 ± 0.001 $\mu\mathrm{K}^2$ sr. Differences in the inferred source amplitude at this level affect the final power spectrum by about 1%, which is also about the level at which second-order effects due to beam asymmetry can alter the spectrum. We expect our understanding of these effects to improve significantly with additional years of data. In the meantime, our revised estimate of $A = 0.014 \pm 0.003$ $\mu\mathrm{K}^2$ sr encompasses both our original estimate and the new Huffenberger et al. (2006) estimate. The effect of these estimates on cosmological parameters is discussed in Huffenberger et al. (2006) and in Appendix A of Spergel et al. (2007).

The bottom panel of Figure 13 shows the band-averaged cross-power spectra after subtraction of the template-based Galactic foreground model and the above source model. The Q-band spectra exhibit clear deviations of order 10% from the V- and W-band spectra at low l, while the higher frequency combinations all agree with each other to better than 5%. Also, while subtracting the source model in equation (43) brings the high-l Q-band spectrum into good agreement with the higher frequency results up to $l \sim 400$, beyond this point the 0.48° angular resolution of Q-band limits the sensitivity of this band. This is also the l range where the effects of the Q-band beam asymmetry start to bias our pseudo-C_l-based power spectrum estimates. Since the V- and W-band data alone provide a cosmic variance limited measurement of the power spectrum up to $l = 400$ (see § 7.5) we have decided to omit Q-band data entirely from our final power spectrum estimate. But note that Q band serves a valuable role in fixing the amplitude of the residual point source contribution, and in helping us to assess the quality of the Galactic foreground subtraction.

7.3. *Low-l Moments from the ILC Map* ($l = 1, 2, 3$)

Based on our analysis of the ILC method presented in § 5.2, we conclude that the newly debiased 3 year ILC map is suitable for analysis over the full sky up to $l \lesssim 10$, although we have not performed a full battery of non-Gaussian tests on this map, so we still advise users to exercise caution. Tegmark et al. (2003) arrived at a similar conclusion based on their foreground analysis of the first-year data. In this section we use the ILC map to evaluate the low-l a_{lm} coefficients by direct full-sky integration of equation (32). In § 7.4 we estimate the low-l power spectrum using a maximum likelihood estimate based on the ILC map using only data outside the Kp2 sky cut. We compare the two results, as a cross-check, in the latter section.

Sky maps of the modes from $l = 2$ to 8, derived from the ILC map, are shown in Figure 14. There has been considerable comment on the nonrandom appearance of these modes. We discuss this topic in more detail in § 8, but note here that some nonrandom appearances may be deceiving and that high-fidelity simulations and a critical assessment of posterior bias are very important in assessing significance.

7.3.1. *Dipole* ($l = 1$)

Owing to its large amplitude and its role as a *WMAP* calibration source, the $l = 1$ dipole signal requires special handling in the *WMAP* data processing. The calibration process is described

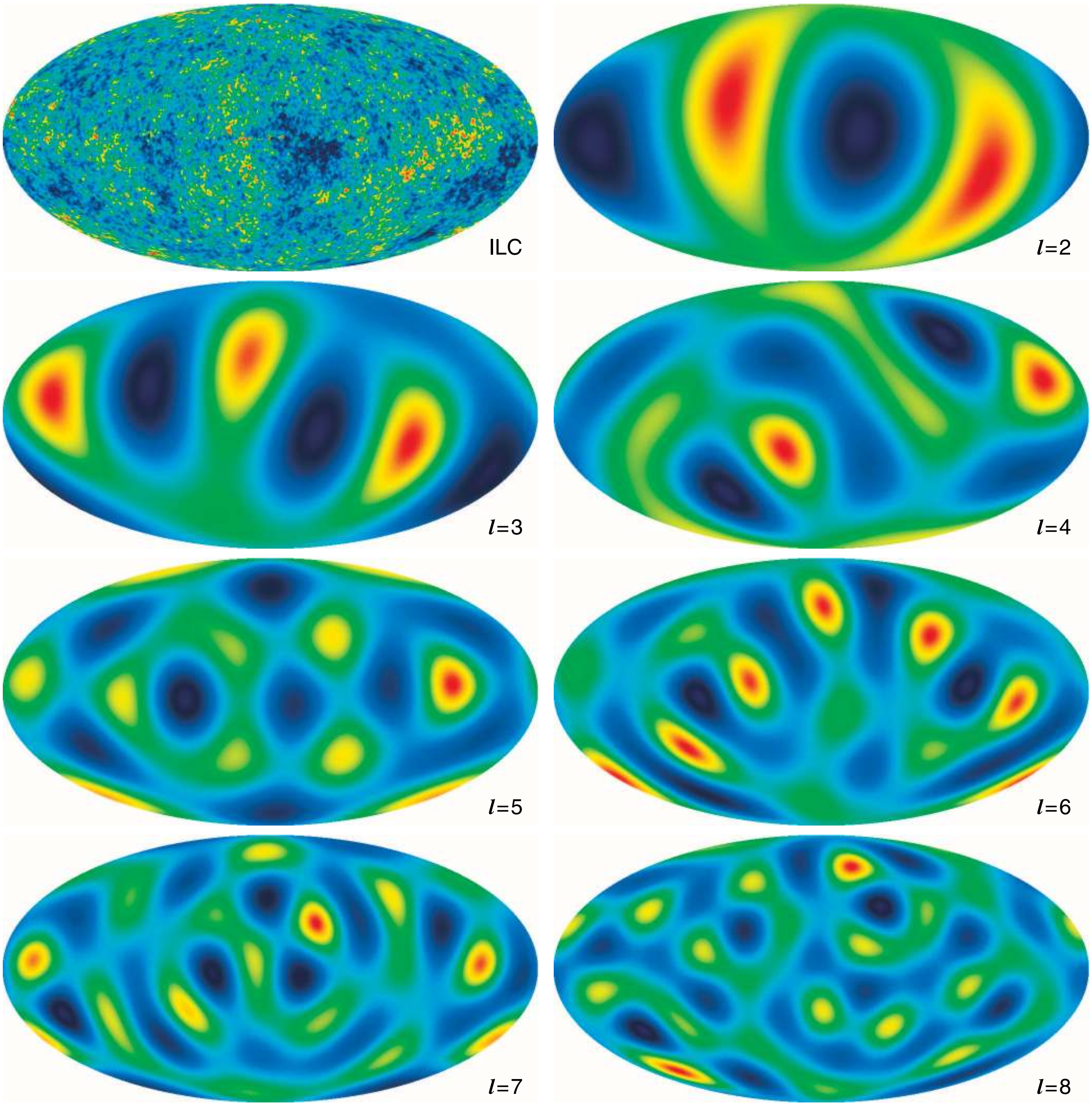

Fig. 14.—Maps of power spectrum modes $l = 2$–8 computed from full-sky fits to the ILC map, shown at top left. Many authors note peculiar patterns in the phase of these modes, and many claim that the behavior is inconsistent with Gaussian random-phase fluctuations, as predicted by inflation. For example, the $l = 5$ mode appears strikingly symmetric (a nonrandom distribution of power in m), while the $l = 2$ and 3 modes appear unusually aligned. The significance of these a posteriori observations is being actively debated. See § 8 for a more detailed discussion.

in detail in Hinshaw et al. (2003b) and in Jarosik et al. (2007). After establishing the calibration, but prior to map-making, we subtract a dipole term from the time-ordered data to minimize signal aliasing that would arise from binning a large differential signal into two finite size pixels. In the first-year analysis we removed the *COBE*-determined dipole from the data, then fit the final maps for a residual dipole. From this, a best-fit *WMAP* dipole was reported, which was limited by the 0.5% calibration uncertainty. For the 3 year data analysis we subtract the *WMAP* first-year dipole from the time-ordered data and fit for a residual dipole in the final ILC map. The results are reported in Table 7. The errors reported for the a_{lm} coefficients in the body of the table are obtained from Monte Carlo simulations of the ILC procedure that attempt to include the effect of Galactic removal uncertainty. In the table end notes we report the dipole direction and magnitude. The direction uncertainty is dominated by Galactic removal errors, while the magnitude uncertainty is dominated by the 0.5% calibration uncertainty.

7.3.2. *Quadrupole* ($l = 2$)

The quadrupole moment computed from the full-sky decomposition of the ILC map is given in Table 7. (The released ILC

TABLE 7
Low-l Multipole Moments (μK)

Moment	$l = 1$[a]	$l = 2$[b]	$l = 3$[c]
$\tilde{a}_{l+3}$	...	...	-11.24 ± 1.48
$\tilde{a}_{l+2}$	...	-14.41 ± 3.13	22.03 ± 0.37
$\tilde{a}_{l+1}$	-239.3 ± 1.2	-0.05 ± 2.62	-13.05 ± 1.55
$\tilde{a}_{l0}$	2505.0 ± 11.1	11.48 ± 3.59	-5.99 ± 0.46
$\tilde{a}_{l-1}$	-2223.6 ± 12.5	4.86 ± 2.62	2.45 ± 0.83
$\tilde{a}_{l-2}$	...	-18.80 ± 2.88	0.70 ± 0.26
$\tilde{a}_{l-3}$	...	...	33.46 ± 1.35

Notes.—Phase convention: the coefficients of the real valued harmonics reported here, $\tilde{a}_{lm}$, are related to the complex coefficients by $\tilde{a}_{lm} = \sqrt{2}\,\mathrm{Im}\,a_{lm}$ for $l < 0$, $\tilde{a}_{lm} = a_{lm}$ for $l = 0$, and $\tilde{a}_{lm} = \sqrt{2}\,\mathrm{Re}\,a_{lm}$ for $l > 0$. Also $\sum_m |\tilde{a}_{lm}|^2 = \sum_m |a_{lm}|^2$.

[a] The dipole components in Galactic rectilinear coordinates are $(x, y, z) = (\tilde{a}_{1+1}, \tilde{a}_{1-1}, \tilde{a}_{10})$; in Galactic polar coordinates the components are $(d, l, b) = (3.358 \pm 0.017$ mK, $263.86° \pm 0.04°$, $48.24° \pm 0.10°)$. The uncertainty in the dipole magnitude is dominated by the 0.5% calibration uncertainty.

[b] Uncertainties from a quadrature sum of calibration error (Jarosik et al. 2007) and Galaxy subtraction error (§ 5.2).

[c] Uncertainties from Galaxy subtraction (§ 5.2).

map and the quadrupole moment reported here have *not* been corrected for the 1.2 μK "kinematic" quadrupole, the second-order Doppler term.) As with the dipole components, the errors reported for the a_{lm} coefficients are obtained from Monte Carlo simulations that attempt to include the effect of Galactic removal uncertainty. The magnitude of this quadrupole moment, computed using equation (34), is $\Delta T_2^2 = 249\ \mu\mathrm{K}^2$ [$\Delta T_l^2 \equiv l(l+1)C_l/2\pi$]. Here, we do not attempt to correct for the bias associated with this estimate, and we postpone a more complete error analysis of ΔT_2^2 to § 7.4. However, we note that this estimate is quite consistent with the maximum likelihood estimate presented in § 7.4.

A corresponding analysis of the first-year ILC map gives $\Delta T_2^2 = 196\ \mu\mathrm{K}^2$. The increase in the 3 year amplitude relative to this value comes mostly from the ILC bias correction and, to a lesser degree, from the improved 3 year gain model. When our new ILC algorithm is applied to the first-year sky maps, we get $\Delta T_2^2 = 237\ \mu\mathrm{K}^2$. While this 41 $\mu\mathrm{K}^2$ bias correction is small in absolute terms, it produces a relatively large *fractional* correction to the small quadrupole. Further discussion of the low quadrupole amplitude is deferred to § 7.4.

7.3.3. *Octopole* ($l = 3$)

The octopole moment computed from the full-sky decomposition of the ILC map is given in Table 7. The reported errors attempt to include the uncertainty due to Galactic foreground removal errors. The magnitude of this octopole moment, computed using equation (34), is $\Delta T_3^2 = 1051\ \mu\mathrm{K}^2$. As above, we do not attempt to correct for the bias associated with this estimate, but again we note that it is quite consistent with the maximum likelihood estimate presented in § 7.4.

It has been noted by several authors that the orientation of the quadrupole and octopole are closely aligned (e.g., de Oliveira-Costa et al. 2005) and that the distribution of power among the a_{lm} coefficients is possibly nonrandom. We discuss these results in more detail in § 8, but we note here that the basic structure of the low-l modes is largely unchanged from the first-year data. Thus we expect that most, if not all, of the "odd" features claimed to exist in the first-year maps will survive.

7.4. *Low-l Spectrum from Maximum Likelihood Estimate* ($l = 2$–30)

If the temperature fluctuations are Gaussian, random phase, and the a priori probability of a given set of cosmological parameters is uniform, the power spectrum may be optimally estimated by maximizing the multivariate Gaussian likelihood function, equation (37). This approach to spectrum estimation gives the optimal (minimum variance) estimate for a given data set, and a means for assessing confidence intervals in a rigorous way. Unfortunately, the approach is computationally expensive for large data sets, and for $l \gtrsim 30$, the results do not significantly improve on the quadratic pseudo-C_l based estimate used in § 7.5 (Efstathiou 2004b; Eriksen et al. 2007). In this section we present the results of a pixel-space approach to spectrum estimation for the multipole range $l = 2$–30 and compare the results with the pseudo-C_l based estimate. In Appendix C we discuss several aspects of maximum likelihood estimation in the limit that instrument noise may be ignored (a very good approximation for the low-l *WMAP* data). In this case, several simple results can be derived analytically and used as a guide to a more complete analysis.

We begin with equation (37) and work in pixel space, where the data, $\boldsymbol{d} = \boldsymbol{t}$, is a sky map. As in Slosar et al. (2004) we account for residual Galactic uncertainty by marginalizing the likelihood over one or more Galactic template fit coefficient(s). That is, we compute the joint likelihood

$$L(C_l, \alpha|\boldsymbol{t}) \propto \frac{\exp\left[-(1/2)(\boldsymbol{t} - \alpha \cdot \boldsymbol{t}_f)^T \boldsymbol{C}^{-1}(\boldsymbol{t} - \alpha \cdot \boldsymbol{t}_f)\right]}{\sqrt{\det \boldsymbol{C}}}, \quad (44)$$

where $\boldsymbol{t}_f$ is one or more foreground emission templates, and α is the corresponding set of fit coefficients, and we marginalize over α

$$L(C_l|\boldsymbol{t}) = \int d\alpha\, L(C_l, \alpha|\boldsymbol{t}). \quad (45)$$

This can be evaluated analytically, as in Appendix B of Hinshaw et al. (2003b).

In practice, we start with the r9 ILC map, we further smooth it with a Gaussian kernel of width 9.183° (FWHM), degrade the map to pixel resolution r4, mask it with a degraded Kp2 mask (accepting all r4 pixels that have more than 50% of its r9 pixels outside the original Kp2 cut), and then add 1 μK rms of white noise to each pixel to aid numerical regularization of the likelihood evaluation. (See Appendix A of Eriksen et al. [2007] for a complete discussion of the numerical aspects of likelihood evaluation.) We evaluate the marginalized likelihood function with the following expression for the covariance matrix:

$$\boldsymbol{C}(\boldsymbol{n}_i, \boldsymbol{n}_j) = \frac{(2l+1)}{4\pi}\sum_l C_l w_l^2 P_l(\boldsymbol{n}_i \cdot \boldsymbol{n}_j) + \boldsymbol{N}. \quad (46)$$

Here w_l^2 is the effective window function of the smoothed map evaluated at low pixel resolution, $P_l(\cos\theta)$ is the Legendre polynomial of order l, and $\boldsymbol{N}$ is a diagonal matrix that describes the 1 μK rms white noise that was added to the map. This expression is evaluated to the Nyquist sampling limit of an r4 map, namely $l_{\max} = 47$. The foreground template we marginalize over is the map $T_{\mathrm{V1}} - T_{\mathrm{ILC}}$, where T_{V1} is the V1 sky map and T_{ILC} is the ILC map. As discussed below, we have tried using numerous other combinations of data and sky cut and obtain consistent estimates of C_l. Eriksen et al. (2007) have also studied this question and obtain similar results using a variety of data combinations and likelihood estimation methodologies.

The full likelihood curves, $L(C_l)$ for $l = 2$–10, are shown in Figure 15 and listed in Table 8. (Note that the likelihood code delivered with the 3 year data release employs the above method up to $l = 30$, then uses the quadratic form employed in the first-year

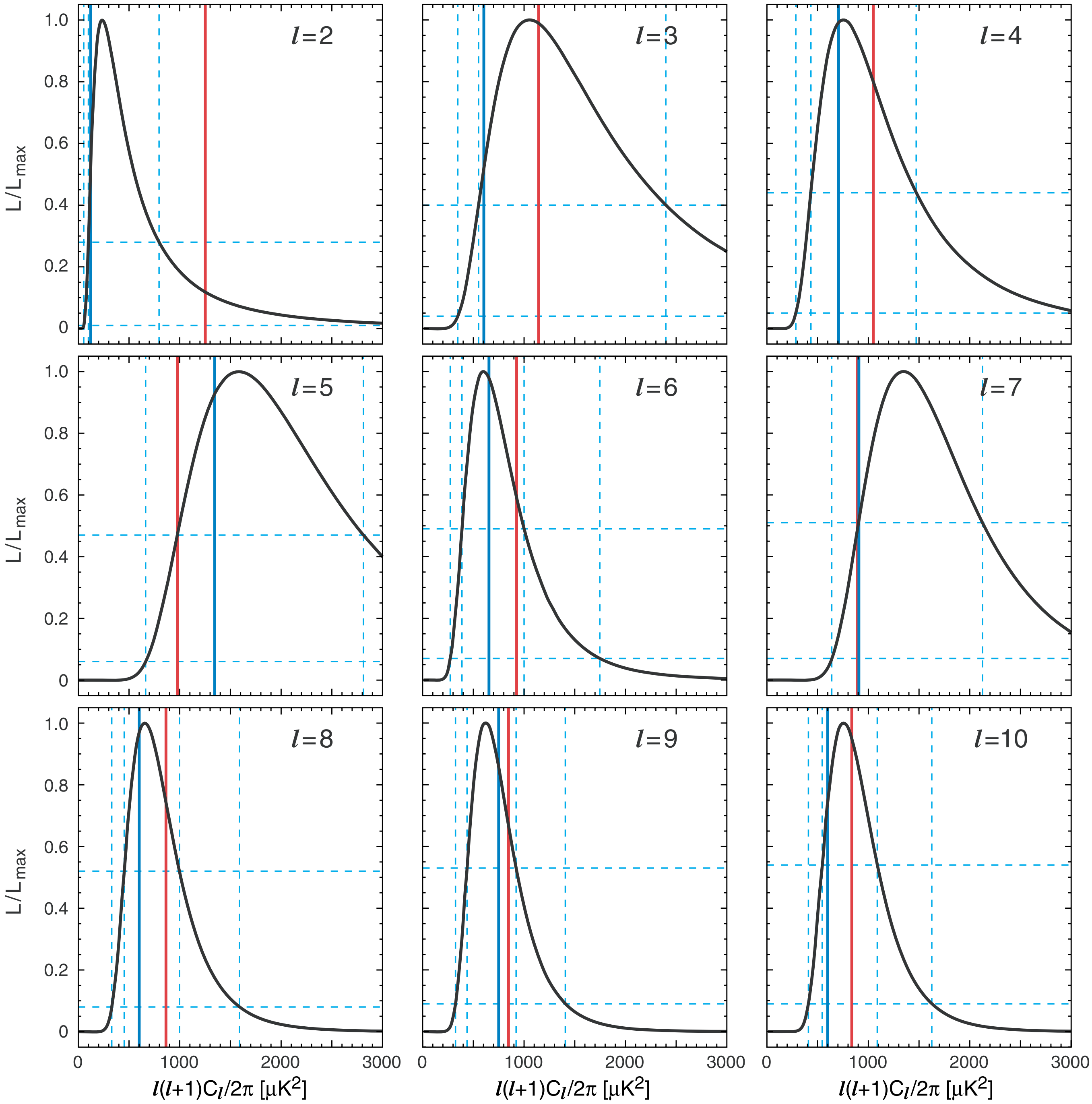

FIG. 15.—Posterior likelihood of $l(l+1)C_l/2\pi$ given the *WMAP* data, for $l = 2$–10. The curves are computed using data from the ILC map evaluated outside the Kp2 sky cut. The vertical blue lines show the values inferred using the pseudo-C_l estimate. These values are well within the posterior likelihood distribution, but there is a tendency for them to be lower than the peak, especially for $l = 2$, 3, and 7. The vertical red lines show the predicted power spectrum from the best-fit ΛCDM model (fit to *WMAP* data). These points are well within the posterior likelihood in all cases; the lighter dashed lines indicate the 68% and 95% confidence regions of the distribution (see § 7.4). Note that the curves approach a Gaussian distribution as l increases.

analysis [Verde et al. 2003] for $l > 30$.) The predicted C_l values from the best-fit ΛCDM model (fit to *WMAP* data only) are shown as vertical red lines, while the values derived from the pseudo-C_l estimate (§ 7.5) are shown as vertical blue lines. Maximum likelihood estimates from the ILC map with and without a sky cut are also shown, as indicated in the figure. There are several comments to be made in connection with these results:

1. All of the maximum likelihood estimates (the black curve and the vertical dot-dashed lines in Fig. 15) are all consistent with each other, in the sense that they all cluster in a range that is much smaller than the overall 68% confidence interval, which is largely set by cosmic variance. We conclude from this that foreground removal errors and the effects of masking are not limiting factors in cosmological model inference from the low-l power spectrum. However, they may still play an important role in determining the significance of low-l features beyond the power spectrum.

2. The C_l values based on the pseudo-C_l estimates (shown in blue) are generally consistent with the maximum likelihood estimates. However, the results for $l = 2$, 3, and 7 are all nearly a

TABLE 8
Maximum Likelihood Spectrum ($l = 2$–10)

l	ΔT_l^2	−95%	−68%	+68%	+95%
2	236	54	99	796	3827
3	1053	347	552	2398	6036
4	752	285	434	1472	3131
5	1582	664	977	2811	5338
6	601	272	388	1000	1747
7	1345	639	904	2126	3591
8	655	330	453	998	1589
9	621	324	438	922	1407
10	755	409	545	1088	1626

factor of 2 lower than the ML values, and lie where the likelihood function is roughly half of its peak value. This discrepancy may be related to the different assumptions the two methods make regarding the distribution of power in the a_{lm} when faced with cut-sky data. Both methods have been demonstrated to be unbiased as long as the noise properties of the data are correctly specified, but the maximum likelihood estimate has a smaller variance. In addition, we note that the two methods are identical in the limit of uniformly weighted, full-sky data; and the maximum likelihood estimate based on cut-sky data is consistent with the full-sky estimate. In light of this, we adopt the maximum likelihood estimate of C_l for $l = 2$–30.

3. The best-fit ΛCDM model lies well within the 95% confidence interval of $L(C_l)$ for all $l \leq 10$, including the quadrupole. Indeed, while the observed quadrupole amplitude is still low compared to the best-fit ΛCDM prediction (236 μK^2 vs. 1252 μK^2, for ΔT_2^2) the probability that the ensemble-average value of ΔT_2^2 is as large or larger than the model value is 16%. This relatively high probability is due to the long tail in the posterior distribution, which reflects the χ_ν^2 distribution ($\nu = 2l+1$) that Gaussian models predict the C_l will follow. Clearly, the residual uncertainty associated with the exact location of the maximum likelihood peak in Figure 15 will not fundamentally change this situation.

There have been several other focused studies of the low-l power spectrum in the first-year maps, especially $l = 2$ and 3, owing to their somewhat peculiar behavior and their special nature as the largest observable structure in the universe (Efstathiou 2003, 2004a; Gaztanaga et al. 2003; Bielewicz et al. 2004; Slosar et al. 2004). These authors agree that the quadrupole amplitude is indeed low, but not low enough to rule out ΛCDM.

7.5. *High-l Spectrum from Combined Pseudo-C_l Estimate* ($l = 30$–1000)

The final spectrum for $l > 30$ is obtained by forming a weighted average of the individual cross-power spectra, equation (38), computed as per Appendix A in Hinshaw et al. (2003b). For the 3 year analysis, we evaluate the constituent pseudo-a_{lm} data using uniform pixel weights for $l < 500$ and $N_{\rm obs}$ weights for $l > 500$. For the latter we use the high-resolution r10 maps to reduce pixelization smearing. Given the pseudo-a_{lm} data, we evaluate cross-power spectra for all 153 independent combinations of V- and W-band data (§ 7.1).

The weights used to average the spectra are obtained as follows. First, the diagonal elements of a Fisher matrix, F_l^{ii}, are computed for each DA i, following the method outlined in Appendix D of Hinshaw et al. (2003b). Since the sky coverage is so similar from year to year (see Fig. 2), we compute only one set of F_l^{ii} for all 3 years using the year 1 $N_{\rm obs}$ data. To account for $1/f$ noise, the low-l elements of each Fisher matrix are decreased according to the noise bias model described in § 7.1.2. Then F_l^{ii} gives the relative noise per DA (as measured by the noise bias) and the relative beam response at each l. We weight the cross-power spectra using the product $F_l^{ij} = (F_l^{ii} F_l^{jj})^{1/2}$.

The noise bias model, equation (42), is propagated through the averaging to produce an effective noise bias

$$N_l^{\rm eff} = \sqrt{\frac{1}{\sum_{ij} (N_l^i)^{-1} (N_l^j)^{-1}}}, \tag{47}$$

where N_l^i is the noise bias model for DA i, and the sum is over all DA pairs used in the final spectrum. In the end, the noise error in the combined spectrum is expressed as

$$\Delta C_l = \sqrt{\frac{a}{2l+1}} \frac{N_l^{\rm eff}}{f_l^{\rm sky}}. \tag{48}$$

Here, $f_l^{\rm sky}$ is the effective sky fraction observed, which we calibrate using Monte Carlo simulations (Verde et al. 2003). The factor a is 1 for TE, TB, and EB spectra, and 2 for TT, EE, and BB spectra. Note that the final error estimates are independent of the original Fisher elements, F_l^{ii}, which are only used as relative weights. Note also that $N_l^{\rm eff}$ is separately calibrated for both regimes of pixel weighting, uniform and $N_{\rm obs}$.

The full covariance matrix for the final spectrum includes contributions from cosmic variance, instrument noise, mode coupling, and beam and point-source uncertainties. We have revised our handling of beam and source errors in the 3 year analysis, as discussed in Appendix A. However, the remaining contributions are treated as we did in the first-year analysis (Hinshaw et al. 2003b; Verde et al. 2003). A good estimate of the uncertainty per C_l is given by

$$\Delta C_l = \frac{1}{f_l^{\rm sky}} \sqrt{\frac{2}{2l+1}} (C_l^{\rm fid} + N_l^{\rm eff}), \tag{49}$$

where $C_l^{\rm fid}$ is a fiducial model spectrum. This estimate includes the effects of cosmic variance, instrument noise, and mode coupling, but not beam and point-source uncertainties. However, these effects are accounted for in the likelihood code delivered with the 3 year release.

7.6. *The Full Power Spectrum*

To construct the final power spectrum, we combine the maximum likelihood results from Table 8 for $l \leq 30$ with the pseudo-C_l based cross-power spectra, discussed above, for $l > 30$. The results are shown in Figure 16, where the *WMAP* data are shown in black with noise-only errors, the best-fit ΛCDM model, fit to the 3 year data, is shown in red, and the 1 σ error band due to cosmic variance shown in lighter red. The data have been averaged in l bands of increasing width, and the cosmic variance band has been binned accordingly. To see the effect that binning has on the model prediction, we average the model curve in the same l bins as the data and show the results as dark red diamonds. For the most part, the binned model is indistinguishable from the unbinned model except in the vicinity of the second acoustic peak and trough.

Based on the noise estimates presented in § 7.1.2, we determine that the 3 year spectrum is cosmic variance limited to $l = 400$. The S/N per l-mode exceeds unity up to $l = 850$, and for bins of width $\Delta l/l = 3\%$, the S/N exceeds unity up to $l = 1000$. In the noise-dominated, high-l portion of the spectrum, the 3 year data

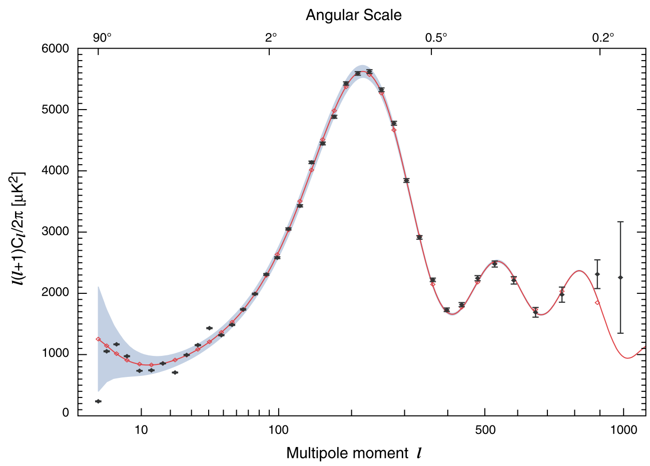

FIG. 16.—Binned 3 year angular power spectrum (in black) from $l = 2$–1000, where it provides a cosmic variance limited measurement of the first acoustic peak, a robust measurement of the second peak, and clear evidence for a rise to the third peak. The points are plotted with noise errors only (see text). Note that these errors decrease linearly with continued observing time. The red curve is the best-fit ΛCDM model, fit to *WMAP* data only (Spergel et al. 2007), and the band is the binned 1 σ cosmic variance error. The red diamonds show the model points when binned in the same way as the data.

are more than 3 times quieter than the first-year data due to (1) the additional years of data and (2) the use of finer pixels in the V and W band sky maps, which reduces pixel smearing at high l. The χ^2_ν of the full power spectrum relative to the best-fit ΛCDM model is 1.068 for 988 degrees of freedom ($13 < l < 1000$) (Spergel et al. 2007). The distribution of χ^2 versus l is shown in Figure 17, and is discussed further below.

The first two acoustic peaks are now measured with high precision in the 3 year spectrum. The second trough and the subsequent rise to a third peak are also well established. To quantify these results, we repeat the model-independent peak and trough fits that were applied to the first-year data by Page et al. (2003b). The results of this analysis are listed in Table 9. We note here that the first two acoustic peaks are seen at $l = 220.8 \pm 0.7$ and $l = 530.9 \pm 3.8$, respectively, while in the first-year spectrum, they were located at $l = 220.1 \pm 0.8$ and $l = 546 \pm 10$. Table 9 also shows that the second trough is now well measured and that the rise to the third peak is unambiguous, but the position and

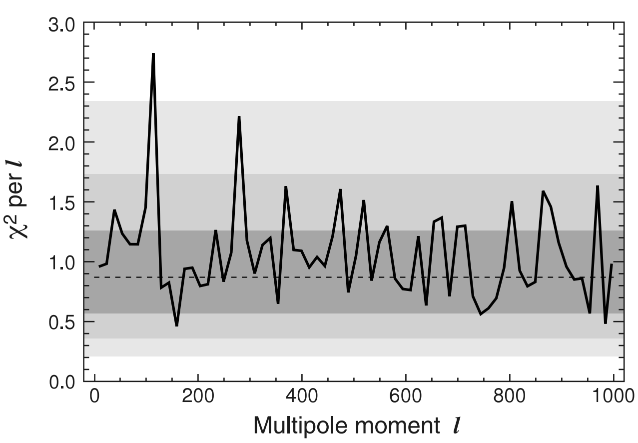

FIG. 17.—χ^2 vs. l for the full power spectrum relative to the best-fit ΛCDM model, fit to *WMAP* data only. The χ^2 per l has been averaged in l-bands of width $\Delta l = 15$. The dark to light gray shading indicates the 1, 2, and 3 σ confidence intervals for this distribution, respectively. The dashed line indicates the mode.

TABLE 9

WMAP POWER SPECTRUM PEAK AND TROUGH DATA

Quantity	l	ΔT_l^2 (μK^2)
First peak	220.8 ± 0.7	5624 ± 30
First trough	412.4 ± 1.9	1716 ± 28
Second peak	530.9 ± 3.8	2485 ± 44
Second trough	675.2 ± 11.1	1688 ± 81

amplitude of the third peak are not yet well constrained by *WMAP* data alone.

Figure 18 shows the 3 year *WMAP* spectrum compared to a set of recent balloon and ground-based measurements that were selected to most complement the *WMAP* data in terms of frequency coverage and l range. The non-*WMAP* data points are plotted with errors that include both measurement uncertainty and cosmic variance, while the *WMAP* data in this l range are largely noise-dominated, so the effective error is comparable. When the *WMAP* data are combined with these higher resolution CMB measurements, the existence of a third acoustic peak is well established, as is the onset of Silk damping beyond the third peak.

The 3 year spectrum is compared to the first-year spectrum in Figure 19. We show the new spectrum in black and the old one in red. The best-fit ΛCDM model, fit to the 3 year data, is shown in gray. In the top panel, the as-published first-year spectrum is shown. The most noticeable differences between the two spectra are (1) the change at low-l due to the adoption of the maximum likelihood estimate for $l \leq 30$, (2) the smaller uncertainties in the noise-dominated high-l regime, discussed further below, and (3) a small but systematic difference in the mid-l range due to improvements in our determination of the beam window functions (§ 7.1.1). The middle panel shows the ratio of the new spectrum to the old. For comparison, the red curve shows the (inverse) ratio of the 3 year and first-year window functions, which differ by up to 2%. The spectrum ratio tracks the window function ratio well up to $l \sim 500$, at which point the sensitivity of the first-year spectrum starts to diminish. For $l \leq 30$ in this panel, we have

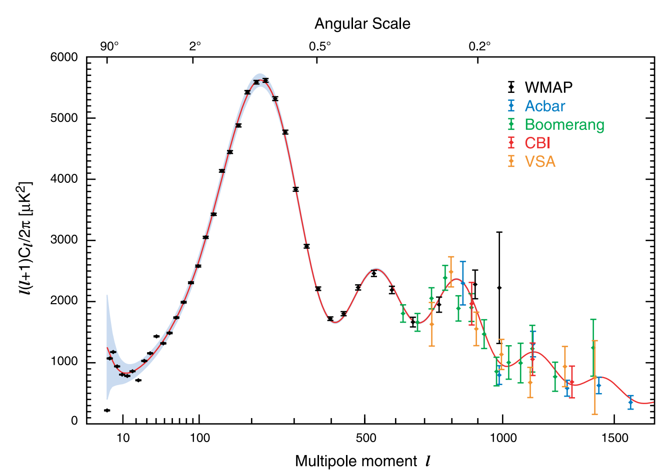

FIG. 18.—*WMAP* 3 year power spectrum (in black) compared to other recent measurements of the CMB angular power spectrum, including Boomerang (Jones et al. 2005), Acbar (Kuo et al. 2004), CBI (Readhead et al. 2004), and VSA (Dickinson et al. 2004). For clarity, the $l < 600$ data from Boomerang and VSA are omitted, as the measurements are consistent with *WMAP*, but with lower weight. These data impressively confirm the turnover in the third acoustic peak and probe the onset of Silk damping. With improved sensitivity on subdegree scales, the *WMAP* data are becoming an increasingly important calibration source for high-resolution experiments.

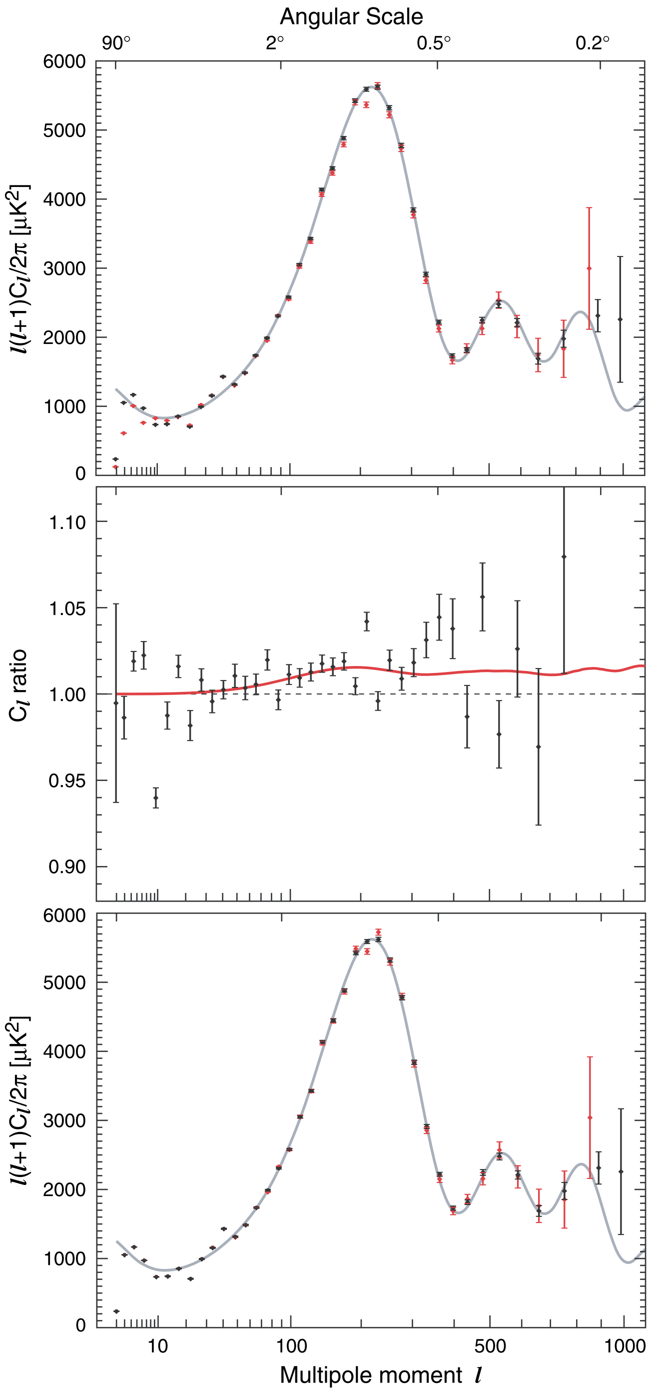

FIG. 19.—Comparison of the 3 year angular power spectrum with the first-year result. *Top*: The 3 year combined spectrum, in black, is shown with the first-year spectrum, as published, in red. The best-fit 3 year ΛCDM model is shown in gray for comparison. For $l < 30$, the difference is due to a change in estimation methodology: the 3 year spectrum is based on a maximum likelihood estimate, while the first-year results is based on a pseudo-C_l estimate. For $l > 100$ the difference is due primarily to (1) an improved determination of the *WMAP* beam response, and (2) the improved sensitivity of the 3 year data. *Middle*: Ratio of the 3 year spectrum to the first-year spectrum. For $l < 30$ we plot the ratio of the two pseudo-C_l-based spectra to show the consistency of the underlying data. The red curve is the ratio of the first-year window function to the 3 year window function. *Bottom*: Same as top panel, except that the first-year spectrum has been multiplied by the window function ratio depicted in the middle panel, and the maximum likelihood estimate has been substituted for $l < 30$.

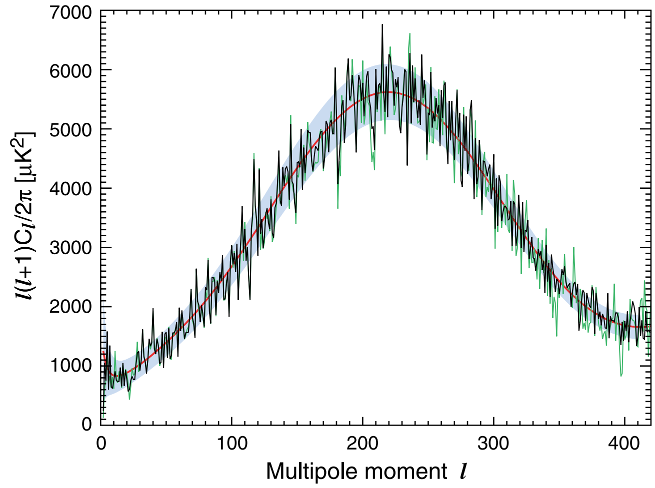

FIG. 20.—Unbinned 3 year angular power spectrum (in black) from $l = 2$–400, where it provides a cosmic variance limited measurement of the first acoustic peak. The first-year spectrum is shown in green for comparison. The red curve with the gray band is the best-fit ΛCDM model and 1 σ error band per l. The width of the band is dominated by cosmic variance to $l = 400$. One feature that was singled out in the first-year spectrum was the "bite" at $l \sim 208$. The feature is still visible in the 3 year spectrum, but not prominently. We believe that this feature was predominantly a noise fluctuation in the first-year data.

substituted the pseudo-C_l based spectrum from the 3 year data into this ratio to show the stability of the underlying sky map data. When based on the same estimation method, the two spectra agree to within ~2%, despite changes in the gain model and in the details of the Galactic foreground subtraction, both of which affect the low-l data. (The gain model changes *are* important for the polarization data, while the temperature-based foreground model has no direct bearing on polarization.) The bottom panel shows the 3 year and first-year spectra again, but this time the first-year data have been deconvolved with the 3 year window functions and we have substituted the maximum likelihood estimate into the first-year spectrum. The agreement between the two is now excellent.

As noted above, the power spectrum is now measured with cosmic variance limited sensitivity to $l = 400$, which happens to coincide with the measured position of the first trough in the acoustic spectrum (Table 9). Figure 20 shows the measurement of the first acoustic peak with no binning in l. The black trace shows the 3 year measurement, while the gray trace shows the first-year result for comparison. The background error band gives the 1 σ uncertainty per l for the 3 year data, including the effects of Galaxy masking and a minimal contribution from instrument noise at the high- l limit. In the first-year power spectrum there were several localized features, which have become known, technically, as "glitches." The most visible was a "bite" near the top of the first acoustic peak, from $l = 205$ to 210. Figure 20 shows that the feature still exists in the 3 year data, but it is not nearly as prominent, and it disappears almost entirely from the binned spectrum. In this l range, the pixel weights used to evaluate the pseudo-C_l data changed from "transitional" in the first-year analysis (see Appendix A of Hinshaw et al. 2003b) to uniform in the 3 year analysis. This reduces the effective level of cosmic variance in this l range, while increasing the small noise contribution somewhat. We conclude that the feature was likely a noise fluctuation superposed on a moderate signal fluctuation.

Several other glitches remain in the low-l power spectrum, perhaps including the low quadrupole. Several authors have commented on the significance of these features (Efstathiou 2003; Lewis 2004; Bielewicz et al. 2004; Slosar et al. 2004), and several more have used the C_l data to search for features in the underlying primordial spectrum, $P(k)$ (Shafieloo & Souradeep 2004; Martin & Ringeval 2004, 2005; Tocchini-Valentini et al. 2006; see also Spergel et al. 2007). Figure 17 shows that the binned χ^2 per l-band is slightly elevated at low l, but not to a compelling degree. In the absence of an established theoretical framework in which to interpret these glitches (beyond the Gaussian, random phase paradigm), they will likely remain curiosities.

8. BEYOND THE ANGULAR POWER SPECTRUM: LARGE-SCALE FEATURES

The low l CMB modes trace the largest structure observable in the universe today. In an inflationary scenario, these modes were the first to leave the horizon and the most recent to re-enter. Since they are largely unaffected by sub-horizon-scale acoustic evolution, they also present us with the cleanest remnant of primordial physics available today. Unusual behavior in these modes would be of potentially great and unique importance.

Indeed, there do appear to be some intriguing features in the data, but their significance is difficult to ascertain and has been a topic of much debate. In this section we briefly review the claims that have been made to date and comment on them in light of the 3 year *WMAP* data. These features include: low power, especially in the quadrupole moment; alignment of modes, particularly along an "axis of evil"; unequal fluctuation power in the northern and southern sky; a surprisingly low three-point correlation function in the northern sky; an unusually deep/large cold spot in the southern sky; and various "ringing" features, "glitches," and/or "bites" in the power spectrum. Of course, one expects to encounter low-probability features with any a posteriori data analysis, and there are no clear-cut rules for assigning the degree of posterior bias to any given observation, so some amount of judgment is called for. Ultimately, the most scientifically compelling development would be the introduction of a new model that explains a number of currently disparate phenomena in cosmology (such as the behavior of the low-l modes and the nature of the dark energy), while also making testable predictions of new phenomena.

8.1. *Summary of First-Year Results*

The two-point correlation function computed from the first-year *WMAP* data showed a notable lack of signal on large angular scales (Spergel et al. 2003). Similar behavior was also seen in the *COBE* DMR data (Hinshaw et al. 1996), making unidentified experimental systematic effects an unlikely cause. Because the two-point function is the Legendre transform of the angular power spectrum, the large-scale behavior of $C(\theta)$ is dominated by the lowest l modes, especially the quadrupole. So this signature is at least partially a reflection of the low quadrupole amplitude.

To study this further, Spergel et al. (2003) characterized the feature by an integral, $S = \int_{-1}^{+1/2} C^2(\theta) d\cos\theta$, which measures the power in $C(\theta)$ for $\theta > 60°$. In a Monte Carlo simulation, only 0.15% of the realizations produced a value of S as small as did the *WMAP* data. It remains to assess the degree to which Galactic errors and posterior bias (the selection of the 60° integration limit) affect this result. Niarchou et al. (2004) concluded that the evidence for measurement error was at least as likely as the evidence for a cutoff in the primordial power spectrum, but that both in both cases the evidence was weak.

Tegmark et al. (2003) produced a high-resolution full-sky CMB map by using a variant of the foreground cleaning approach developed by Tegmark & Efstathiou (1996). They cautiously quote a quadrupole amplitude of 202 μK^2, evaluated over the full sky. They further remark that the quadrupole and octopole phases are notably aligned with each other and that the octupole is unusually "planar," with most of its power aligned approximately with the Galactic plane. De Oliveira-Costa et al. (2004b) estimate the a priori chance of observing both the low quadrupole, the $l = 2$ and 3 alignment, and the $l = 3$ planarity to be $\sim$1 in 24,000. Note that this estimate does not formally attempt to account for Galactic modeling uncertainty, which will tend to reduce the significance of the noted features. Bielewicz et al. (2004) confirmed the above result, and they further conclude that the $l = 3$ properties are stable with respect to the applied mask and the level of foreground correction, but that the quadrupole is much less so.

Schwarz et al. (2004) claimed that the quadrupole and octopole are even more correlated (99.97% CL), with the quadrupole plane and the three octopole planes "remarkably aligned." Furthermore, they claimed that three of these planes are orthogonal to the ecliptic and that the normals to these planes are aligned with the direction of the cosmological dipole and with the equinoxes. This had led to speculation that the low-l signal is not cosmological in origin. Copi et al. (2004) use "multipole vectors" to characterize the geometry of the l modes. They conclude that the "oriented area of planes defined by these vectors. . .is inconsistent with the isotropic Gaussian hypothesis at the 99.4% level for the ILC map." (See also Katz & Weeks 2004.)

Eriksen et al. (2004a), in their study of the ILC method, confirm that the quadrupole and octopole are strongly aligned. They also note that the $l = 5$ mode is "spherically symmetric" at $\sim 3\ \sigma$, and the $l = 6$ mode is planar at $\sim 2\ \sigma$ confidence (see Fig. 14). But they add that the first-year ILC map is probably not clean enough to use for cosmological analyses of this type. Land & Magueijo (2005) point out that the $l = 3$ and 5 modes are aligned in both direction and azimuth, thereby "rejecting statistical isotropy with a probability in excess of 99.9%."

Hansen et al. (2004a) fit cosmological parameters to the *WMAP* data separately in the northern and southern hemispheres in three coordinate systems. They conclude that "it may be necessary to question the assumption of cosmological isotropy." Eriksen et al. (2004b) evaluate the ratio of low-l power between two hemispheres and conclude that only 0.3% of simulated skies have as low a ratio as observed, even when allowing the (simulated) data to define the direction. Hansen et al. (2004b) reach a similar conclusion and note that it is "hard to explain in terms of residual foregrounds and known systematic effects."

Faced with so many apparently unlikely features in the data, our foremost priority is to re-evaluate potential sources of systematic error in the maps. Indeed, a by-product of the exhaustive 3 year polarization analysis is enhanced confidence in the accuracy of the temperature signal. Figure 3 shows that, even after all of the processing changes outlined in § 2, the 3 year maps are consistent with the first-year maps up to a small quadrupole difference (Table 3) that is well within the first-year error budget (Hinshaw et al. 2003a). Furthermore, the improvements applied to the ILC processing to reduce Galactic foreground residuals did not visibly alter the low-l phase structure in the 3 year ILC map (Fig. 14), nor the north-south asymmetry that is plainly visible in Figure 21. We have made no attempt to evaluate the above-noted statistics using the 3 year maps, so the degree to which they persist remains to be seen.

9. SUMMARY AND CONCLUSIONS

For the 3 year *WMAP* data release, we have made improvements in nearly every aspect of the data-processing pipeline, many of which were driven by the need to successfully characterize the instrument noise to the level required to measure the polarization signal, $\sim 0.1\ \mu K$. The improvements are spelled out in detail here and in the companion papers by Jarosik et al. (2007), Page et al. (2007), and Spergel et al. (2007). The key points follow.

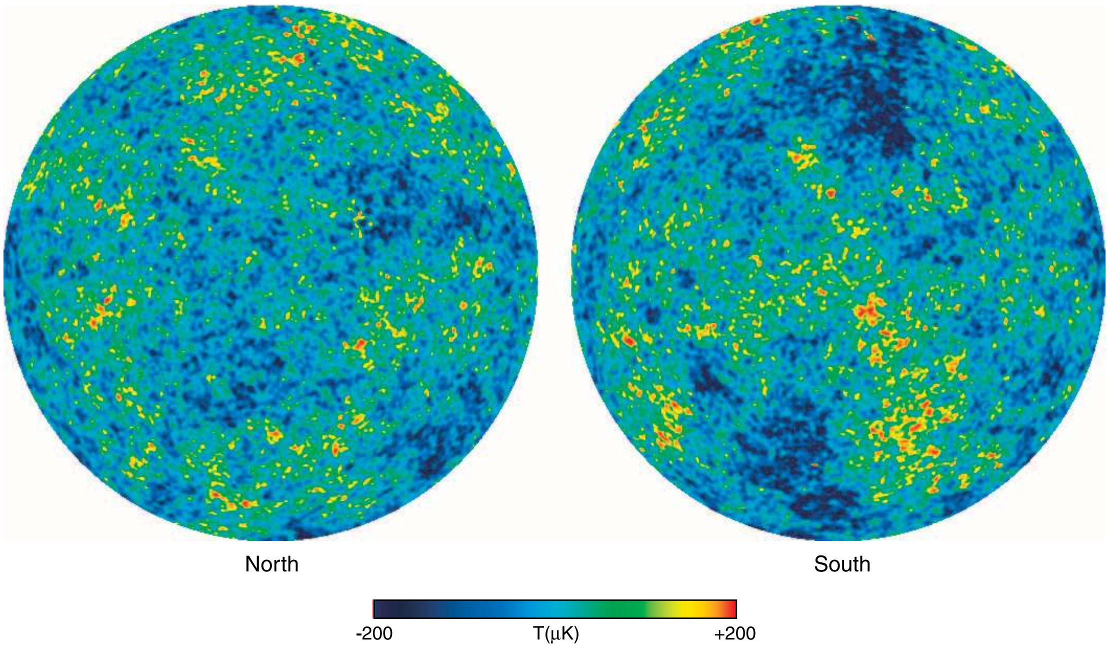

Fig. 21.—Full-sky maps in ecliptic coordinates smoothed to 1° resolution, shown in Lambert azimuthal equal-area projection. *Top*: 3 year ILC map; *bottom*: 3 year W-band map with the Kp2 Galaxy mask superposed, but no other foreground removal applied. Note the qualitative differences in large-scale power between the two hemispheres, as has been noted by several authors (see text). The statistical significance of this difference continues to be an area of active study.

1. Improved models of the instrument gain and beam response are now accurate to better than 1% and do not currently limit the scientific conclusions that can be drawn from the data. Polarization-specific effects such as spurious pickup from radiometer bandpass mismatch have also been accounted for in the data processing, and do not limit the data.

2. The map-making procedure has been overhauled to produce genuine maximum likelihood maps of the temperature and polarization signal. In concert with this, we have produced code to evaluate the corresponding pixel-pixel weight matrix (inverse covariance matrix) at pixel resolution r4. This was required to adequately characterize the noise for the polarization analysis (Jarosik et al. 2007).

3. The 3 year temperature maps are consistent with the first-year maps (§ 3) and, to a good approximation, have 3 times lower variance. A by-product of the exhaustive polarization analysis is enhanced confidence in the accuracy of the temperature signal.

4. We have updated the MEM, ILC, and template-based temperature foreground emission models and assessed their uncertainties. We have developed new models of the polarized foreground emission that allow us to extract the cosmological reionization signal and that pave the way for future studies of CMB polarization (Page et al. 2007).

5. Our analysis of the temperature power spectrum is improved at low l by employing a maximum likelihood estimate. At high l, the spectrum is >3 times more sensitive due to the additional years of data and the use of r10 sky maps to reduce the effects of pixel smoothing. We have also placed new limits on systematic effects in the power spectrum due to beam ellipticity.

6. We have updated the *WMAP* point-source catalog. The contribution of unresolved sources to the power spectrum has been updated and subtracted.

7. We have developed new methods to evaluate polarization power spectra from sky map data. Our approach accounts for the following key issues: (1) sky cuts, (2) low signal amplitude, (3) correlated noise from $1/f$ and scan-related effects, and (4) other polarization-specific effects, such as baseline sensitivity, and bandpass

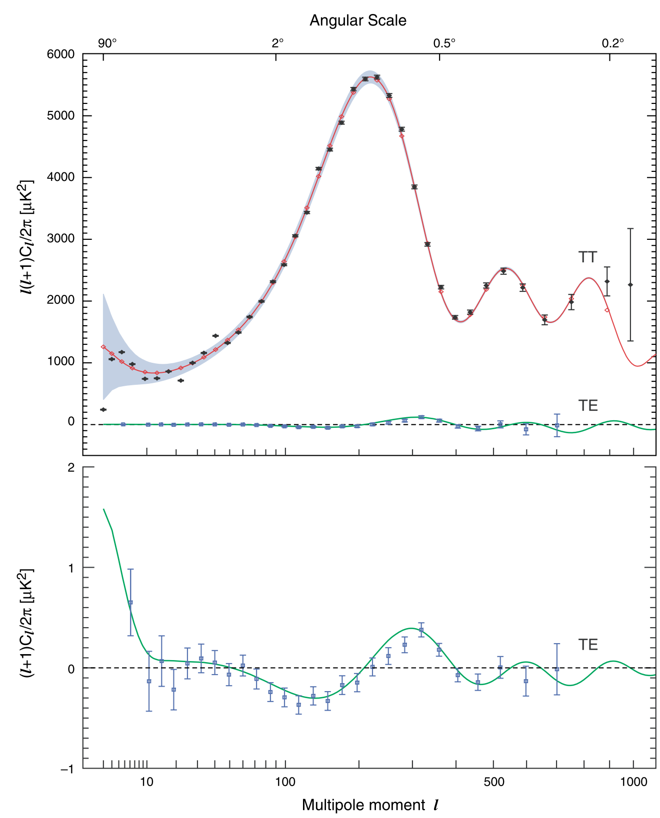

Fig. 22.—Angular power spectra $C_l^{\rm TT}$ & $C_l^{\rm TE}$ from the 3 year *WMAP* data. *Top*: The TT data are as shown in Fig. 16. The TE data are shown in units of $l(l+1)C_l/2\pi$, on the same scale as the TT signal for comparison. *Bottom*: The TE data, in units of $(l+1)C_l/2\pi$. This updates Fig. 12 of Bennett et al. (2003b).

mismatch. This effort was developed in conjunction with the processing of polarization sky maps (Page et al. 2007).

8. Figure 22, which updates Figure 12 from Bennett et al. (2003b), shows the 3 year TT and TE power spectra (§ 7.6 and Page et al. 2007). The TT measurement is cosmic variance limited up to $l = 400$, and has a S/N > 1 up to $l = 1000$, in l bands of width 3%. The high-l TE signal is consistent with the first-year result, while for $l < 6$ the signal is reduced. A detailed comparison of the 3 year TE signal to the first-year is shown in Figure 24 of Page et al. (2007). The implications for the inferred optical depth, τ, are shown in their Figure 26, which includes a detailed comparison of the 3 year results with the first-year.

9. We have refined the evaluation of the likelihood function used to infer cosmological parameters. The new approach uses pixel-space inputs for the low-l temperature and polarization data and correctly accounts for the joint probability of the temperature and polarization signal (Page et al. 2007). We use this to infer cosmological parameters from the 3 year data. Many parameter degeneracies that existed in the first-year results are greatly reduced by having new EE data and more sensitive high-l TT data. Figure 1 of Spergel et al. (2007) illustrates this for the parameter pairs (n_s,τ) and (n_s,$\Omega_b h^2$). A cosmological model with only six parameters still provides an excellent fit to *WMAP* and other cosmological data.

10. With new constraints on τ from the EE data, we get correspondingly tighter constraints on the scalar spectral index, n_s. Using *WMAP* data only, we now find $n_s = 0.960 \pm 0.016$, while combining *WMAP* data with other data gives $n_s = 0.947 \pm 0.015$ (Spergel et al. 2007). Joint limits on n_s and the tensor to scalar ratio, r, are shown in Figure 14 of Spergel et al. (2007).

11. The *WMAP* observatory continues to operate flawlessly, and many results that are currently measured at 2–3 σ confidence, such as the apparent deviation from scale invariance, hints of a running spectral index, and the details of the reionization history, will be significantly clarified by additional years of data.

10. DATA PRODUCTS

All of the 3 year *WMAP* data products are being made available through the Legacy Archive for Microwave Background Data Analysis (LAMBDA),[16] NASA's CMB Thematic Data Center. The low-level products include the time-ordered data (calibrated and raw), the functions used to filter the time-ordered data, and the beam response data. The processed temperature and polarization maps in both 1 year and 3 year forms, with and without foreground subtraction, are supplied at pixel resolutions r4, r9, and r10. Full pixel-pixel inverse covariance matrices are supplied for analyzing the r4 polarization maps. The processed foreground products include the MEM component maps, the ILC map, and the temperature and polarization templates used for foreground subtraction. The analyzed CMB products include the angular power spectra, the likelihood used in the 3 year parameter analysis, and a complete Web-based set of parameter results for every combination of data set and cosmological model that was run for the 3 year analysis. For each of the model/data combinations, we also supply the best-fit model spectra and the full Markov chains. The products are described in detail in the *WMAP* Explanatory Supplement (Limon et al. 2006).

[16] The LAMBDA Web site is http://www.lambda.gsfc.nasa.gov/.

We thank Jim Condon, Kevin Huffenberger, Dominik Schwarz, Sergei Trushkin, and the anonymous referee for comments that helped to improve the accuracy and clarity of the material in this paper. We especially thank Hans Kristian Eriksen for helpful comments and for providing us with very thorough cross-checks of our low-l likelihood results. This work led us to adopt a full maximum likelihood evaluation of the spectrum for multipoles up to $l = 30$.

The *WMAP* mission is made possible by support from the Science Mission Directorate at NASA Headquarters and by the hard and capable work of scores of scientists, engineers, technicians, machinists, data analysts, budget analysts, managers, administrative staff, and reviewers. This research was additionally supported by NASA grants LTSA 03-000-0090 and ATP NNG04GK55G. E. K. acknowledges support from an Alfred P. Sloan Research Fellowship. H. V. P. is supported by NASA through Hubble Fellowship grant HF-01177.01-A awarded by the Space Telescope Science Institute, which is operated by the Association of Universities for Research in Astronomy, Inc., for NASA, under contract NAS 5-26555. L. V. is supported by NASA ADP03-0000-0092 and NASA ADP04-0000-0093. We acknowledge use of the HEALPix and CAMB packages.

APPENDIX A

IMPLEMENTATION OF BEAM AND POINT SOURCE ERRORS

In this Appendix we discuss our simplified handling of beam deconvolution uncertainties and point source subtraction errors. Since both of these errors primarily affect the high-l spectrum, we adopt the approximation that the likelihood is Gaussian and develop methodology for computing the change in the likelihood induced by these errors.

A1. LIKELIHOOD DECOMPOSITION

At all but the lowest multipoles, l, the likelihood of the data, $\boldsymbol{d} = \hat{C}_l$, given a theoretical model, $\boldsymbol{m} = C_l$, is well approximated by treating the power spectrum as Guassian distributed,

$$\mathcal{L} \equiv -2 \ln L(\boldsymbol{d}|\boldsymbol{m}) = \sum_{ll'} (\hat{C}_l - C_l)\Sigma^{-1}_{ll'}(\hat{C}_{l'} - C_{l'}) + \ln \det \Sigma \tag{A1}$$

where Σ is the covariance matrix of the data, $\Sigma_{ll'} = \langle \Delta\hat{C}_l \Delta\hat{C}_{l'} \rangle$. As discussed in Hinshaw et al. (2003b), the full covariance matrix may be decomposed into its constituent contributions

$$\Sigma = \Sigma_{\rm cv} + \Sigma_{\rm noise} + \Sigma_{\rm mask} + \Sigma_{\rm beam} + \Sigma_{\rm src}. \tag{A2}$$

Since we are only interested in the final two terms in this Appendix, we introduce a simplified notation whereby

$$\Sigma \equiv \Sigma_0 + \Sigma_1, \tag{A3}$$

where Σ_0 consists of the first three terms: cosmic variance, instrument noise, and mode coupling due to the sky mask; while Σ_1 consists of the last two terms, the beam decovolution and point-source subtraction uncertainties. With this decomposition of the covariance matrix, the likelihood becomes

$$\mathcal{L} = \sum_{ll'} (\hat{C}_l - C_l)(\Sigma_0 + \Sigma_1)^{-1}_{ll'}(\hat{C}_{l'} - C_{l'}) + \ln\det(\Sigma_0 + \Sigma_1). \tag{A4}$$

The key point in the new treatment is that the beam and point-source uncertainties have a very restricted form in l space. The source model has the form given in equation (43), in which we treat A as uncertain, while the beam deconvolution uncertainty may be described by only a handful of modes. As discussed in detail below, this allows us to decompose Σ_1 in the form

$$\Sigma_1 \approx \boldsymbol{U}\boldsymbol{U}^T, \tag{A5}$$

where $\boldsymbol{U}$ is an $N_l \times M$ matrix with $M \ll N_l$ (typically $M \sim 10$). This approximation allows us to efficiently compute Σ^{-1} using the Sherman-Morrison-Woodbury formula,

$$(\Sigma_0 + \Sigma_1)^{-1} \approx (\Sigma_0 + \boldsymbol{U}\boldsymbol{U}^T)^{-1} \tag{A6}$$

$$= \Sigma_0^{-1} - \Sigma_0^{-1}\boldsymbol{U}\left(\boldsymbol{I} + \boldsymbol{U}^T\Sigma_0^{-1}\boldsymbol{U}\right)^{-1}\boldsymbol{U}^T\Sigma_0^{-1}. \tag{A7}$$

With this result the likelihood decomposes into $\mathcal{L} = \mathcal{L}_0 + \mathcal{L}_1$, where

$$\mathcal{L}_0 = \sum_{ll'} (\hat{C}_l - C_l)(\Sigma_0)^{-1}_{ll'}(\hat{C}_{l'} - C_{l'}) + \ln\det\Sigma_0, \tag{A8}$$

and

$$\mathcal{L}_1 = -\sum_{ll'} (\hat{C}_l - C_l)\left[\Sigma_0^{-1}\boldsymbol{U}\left(\boldsymbol{I} + \boldsymbol{U}^T\Sigma_0^{-1}\boldsymbol{U}\right)^{-1}\boldsymbol{U}^T\Sigma_0^{-1}\right]_{ll'}(\hat{C}_{l'} - C_{l'}) + \ln\det(\boldsymbol{I} + \boldsymbol{U}^T\Sigma_0^{-1}\boldsymbol{U}). \tag{A9}$$

Note that we have rewritten the ln det term,

$$\ln\det(\boldsymbol{I} + \Sigma_0^{-1}\boldsymbol{U}\boldsymbol{U}^T) = \ln\det(\boldsymbol{I} + \boldsymbol{U}^T\Sigma_0^{-1}\boldsymbol{U}), \tag{A10}$$

to reduce the dimensionality of the matrix in the determinant from $N_l \times N_l$ to $M \times M$. As a further simplification, we take Σ_0 to be diagonal when evaluating $\mathcal{L}_1$. We have checked that this has a negligible effect on the accuracy of the expression.

A2. BEAM DECONVOLUTION UNCERTAINTY

The detailed form of the covariance matrix due to beam uncertainties was discussed in Hinshaw et al. (2003b), but we review the salient features here. For a pair of cross-power spectra, $C_l^{\boldsymbol{i}}$ and $C_l^{\boldsymbol{j}}$, the beam covariance has the form

$$(\Sigma_b)^{\boldsymbol{ij}}_{ll'} = C_l(\boldsymbol{S}_b)^{\boldsymbol{ij}}_{ll'}C_{l'}, \tag{A11}$$

where

$$(\boldsymbol{S}_b)^{\boldsymbol{ij}}_{ll'} = B^i_{ll'}(\delta_{ij} + \delta_{ij'}) + B^{i'}_{ll'}(\delta_{i'j} + \delta_{i'j'}). \tag{A12}$$

Here i, i' denote the pair of DA's in the spectrum $C_l^{\boldsymbol{i}}$, and similarly for j, j'; $B^i_{ll'}$ is the fractional covariance matrix, $B^i_{ll'} = \langle u^i_l u^i_{l'}\rangle$, where $u^i_l = \Delta b^i_l / b^i_l$ is the fractional error in the beam transfer function b^i_l. The complete beam covariance matrix for the final combined spectrum is

$$(\Sigma_b)_{ll'} = C_l(\boldsymbol{S}_b)_{ll'}C_{l'} = \sum_{\boldsymbol{ij}} C_l w^{\boldsymbol{i}}_l(\boldsymbol{S}_b)^{\boldsymbol{ij}}_{ll'}w^{\boldsymbol{j}}_{l'}C_{l'}, \tag{A13}$$

where the $w^{\boldsymbol{i}}_l$ are the weights used to form the combined spectrum, $\hat{C}_l = \sum_{\boldsymbol{i}} w^{\boldsymbol{i}}_l C^{\boldsymbol{i}}_l$ (see § 7.5).

The beam covariance matrix is dominated by a small number of modes. We take its singular value decomposition, $\boldsymbol{S}_b = \boldsymbol{P}\boldsymbol{w}\boldsymbol{Q}^T$, where $\boldsymbol{P}$ and $\boldsymbol{Q}$ are orthogonal matrices ($\boldsymbol{P} = \boldsymbol{Q}$, since $\boldsymbol{S}_b$ is symmetric), and $\boldsymbol{w} = \mathrm{diag}(w_1, \ldots, w_{N_l})$ is diagonal with singular values $w_1 > \ldots > w_{N_l}$. Only 10 modes have $w_i/w_1 > 10^{-3}$, and only 18 have $w_i/w_1 > 10^{-6}$. Thus we can approximate Σ_b as

$$(\Sigma_b)_{ll'} \approx \sum_{i=1}^{M} C_l\, P_{li} w_i P_{il'}^T\, C_{l'}, \tag{A14}$$

where $M \ll N_l$ is the number of modes used in the approximation. Then, defining an $N_l \times M$ matrix $U_{lk} = C_l P_{li} w_i^{1/2}$, we have $\Sigma_b \approx \boldsymbol{U}\boldsymbol{U}^T$. For the 3 year analysis we use $M = 9$; tests with additional modes changed the TT likelihood by $\Delta\chi^2 < 0.01$.

A3. POINT-SOURCE SUBTRACTION UNCERTAINTY

The amplitude of the point-source correction is uncertain at the 20% level. To include this uncertainty in the likelihood evaluation, we simply add another mode to the matrix $\boldsymbol{U}$ defined above. Specifically, $U_{l(M+1)} = \sigma_A C_l^{\mathrm{src}}$, where $C_l^{\mathrm{src}} = \sum_{\boldsymbol{i}} w_l^{\boldsymbol{i}} C_l^{\boldsymbol{i},\,\mathrm{src}}$ is the point-source model defined in equation (43), and $\sigma_A = 0.21$ is the fractional uncertainty of the point-source amplitude A.

APPENDIX B

BEAM ASYMMETRIES

In Jarosik et al. (2007) we outline our approach to determining the beam transfer functions from flight observations of Jupiter. This method implicitly assumes that the effective beam response is equivalent to the azimuthal average of the response, which is appropriate in the limit that each sky map pixel is observed with equal weight over a full range of azimuth. In practice this is a good approximation near the ecliptic poles, but is less so near the ecliptic plane. In this Appendix we quantify how *WMAP*'s beam asymmetry distorts our estimate of the angular power spectrum by taking into account (1) the intrinsic shape of the beam response in spacecraft-fixed coordinates, (2) the map-making algorithm, including the spacecraft scan strategy, and (3) the form of the estimator used to measure the cross-power spectra.

Wu et al. (2001) treated the MAXIMA beams using an effective symmetric beam. Wandelt & Górski (2001) developed a fast method of convolving two arbitrary band-limited functions on the sphere by transforming it into a three-dimensional Fourier transform.

B1. FORMALISM

The calibrated, differential time-ordered data, $\boldsymbol{d}$, is related to the sky map, $\boldsymbol{t}$, via

$$\boldsymbol{d} = \boldsymbol{M}\boldsymbol{t} + \boldsymbol{n}, \tag{B1}$$

where $\boldsymbol{M}$ is the mapping function and $\boldsymbol{n}$ is the noise, which we assume to have zero mean, $\langle \boldsymbol{n} \rangle = 0$ (Hinshaw et al. 2003a). The maximum likelihood estimate for $\boldsymbol{t}$ is $\hat{\boldsymbol{t}} = \boldsymbol{W}\boldsymbol{d}$, where $\boldsymbol{W} = (\boldsymbol{M}^T\boldsymbol{N}^{-1}\boldsymbol{M})^{-1}\boldsymbol{M}^T\boldsymbol{N}^{-1}$, and $\boldsymbol{N} = \langle \boldsymbol{n}\boldsymbol{n}^T \rangle$ is the noise covariance matrix of the time-ordered data. Using the fact that $\boldsymbol{W}\boldsymbol{M} = \boldsymbol{I}$, where $\boldsymbol{I}$ is the identity matrix, it follows that $\hat{\boldsymbol{t}} = \boldsymbol{W}\boldsymbol{d} = \boldsymbol{t} + \boldsymbol{W}\boldsymbol{n}$. The maximum likelihood map is unbiased because the sky map noise, $\boldsymbol{W}\boldsymbol{n}$, has zero mean.

For a differential instrument like *WMAP* that observes temperature differences between two sides A and B, the mapping function $\boldsymbol{M}$ can be decomposed into two pieces, $\boldsymbol{M}_{\mathrm{A}} - \boldsymbol{M}_{\mathrm{B}}$, which denote the A- and B-side contributions, respectively. For a given side, the matrix elements $\boldsymbol{M}_{ip}$ have the form $g_i(p)\Omega_p$, where $g_i(p)$ is the beam response in pixel p for the ith observation, and Ω_p is the pixel solid angle. The normalization is such that $\int d\Omega\, g_i(p) \rightarrow \sum_p g_i(p)\Omega_p = 1$.

In practice, the solution $\hat{\boldsymbol{t}} = \boldsymbol{W}\boldsymbol{d}$ is too costly to evaluate exactly given the properties of $\boldsymbol{M}$ and $\boldsymbol{N}^{-1}$. Rather, we adopt approximate forms for these quantities, $\boldsymbol{M}'$ and $\boldsymbol{N}'^{-1}$, and estimate the sky map using $\boldsymbol{t}' = \boldsymbol{W}'\boldsymbol{d}$, where $\boldsymbol{W}' = (\boldsymbol{M}'^T\boldsymbol{N}'^{-1}\boldsymbol{M}')^{-1}\boldsymbol{M}'^T\boldsymbol{N}'^{-1}$. The resulting sky map is biased relative to the true sky according to

$$\boldsymbol{t}' = \boldsymbol{W}'\boldsymbol{M}\boldsymbol{t} \equiv \boldsymbol{J}\boldsymbol{t}, \tag{B2}$$

where $\boldsymbol{J} \equiv \boldsymbol{W}'\boldsymbol{M}$. (The distorted sky map noise, $\boldsymbol{W}'\boldsymbol{n}$, still has zero mean.) The map-making algorithm used by *WMAP* assumes that the beams are circularly symmetric with infinite resolution. That is, each row (observation) of $\boldsymbol{M}'$ contains a +1 in the column (pixel) seen by the A-side beam and a -1 in the column (pixel) seen by the B-side beam. In addition, since the *WMAP* instrument noise is nearly white ($\boldsymbol{N} \approx \sigma_0^2\boldsymbol{I}$), the algorithm solves for $\boldsymbol{t}'$ using $\boldsymbol{W}' = (\boldsymbol{M}'^T\boldsymbol{M}')^{-1}\boldsymbol{M}'^T$. The matrix $\boldsymbol{M}'^T\boldsymbol{M}'$ is diagonally dominant, with diagonal elements $N_p = N_p^{\mathrm{A}} + N_p^{\mathrm{B}}$ equal to the number of times pixel p has been observed by either the A- or B-side beam. The action of $\boldsymbol{W}'$ on $\boldsymbol{d}$ is thus approximately

$$\boldsymbol{W}'_{pi} \approx \frac{1}{N_p}(\delta_{pi}^{\mathrm{A}} - \delta_{pi}^{\mathrm{B}}), \tag{B3}$$

where δ_{pi}^{A} is one if the A-side beam is in pixel p and zero otherwise, and likewise for δ_{pi}^{B}. Combining equations (B8) and (B3), we obtain the following expression for the distortion matrix $\boldsymbol{J}$:

$$\boldsymbol{J}_{pp'} \approx \frac{\Omega_p}{N_p}\left(\sum_{i|\mathrm{A}\in p} g_i^{\mathrm{A}}(p') + \sum_{i|\mathrm{B}\in p} g_i^{\mathrm{B}}(p')\right) \equiv \boldsymbol{J}_{pp'}^{\mathrm{A}} + \boldsymbol{J}_{pp'}^{\mathrm{B}}. \tag{B4}$$

Here "$i|\mathrm{A} \in p$" denotes summation over all observations i where the A-side beam observes pixel p. This algorithm produces a sky map in which the effective beam response is an average of the A- and B-side responses convolved with the scan pattern at each pixel.

At small angular scales, where beam asymmetries may become important, a pseudo-C_l method is used to estimate the *WMAP* angular power spectrum from these maps (Hauser & Peebles 1973; Wandelt et al. 2001; Hivon et al. 2002; Hinshaw et al. 2003b). This method estimates the power spectrum C_l by first transforming a weighted map $\boldsymbol{Qt}'$, where $\boldsymbol{Q}$ is a weight matrix used to mask regions of strong foreground contamination and/or high instrument noise. This produces the pseudo-C_l spectrum, $\tilde{C}_l$, which is then corrected for the statistical bias induced by $\boldsymbol{Q}$ under the assumption that the underlying signal is statistically isotropic.

In the present context we wish to correct the power spectrum for the biases induced by both $\boldsymbol{Q}$ and $\boldsymbol{J}$. We transform the distorted map into the spherical harmonic basis, $\boldsymbol{a}' = \Omega_p \boldsymbol{Y}^\dagger \boldsymbol{Qt}' = \Omega_p \boldsymbol{Y}^\dagger \boldsymbol{QJt} = \Omega_p \boldsymbol{Y}^\dagger \boldsymbol{QJYa}$, where $\boldsymbol{a}$ is the (full-sky) spherical harmonic transform of $\boldsymbol{t}$.[17] The covariance matrix of $\boldsymbol{a}'$ is then related to the underlying signal covariance by $\langle \boldsymbol{a}'\boldsymbol{a}'^\dagger \rangle = \mathcal{J}\boldsymbol{S}\mathcal{J}^\dagger$, where $\mathcal{J} = \Omega_p \boldsymbol{Y}^\dagger \boldsymbol{QJY}$ and $\boldsymbol{S}$ is the undistorted CMB signal matrix $\boldsymbol{S} = \langle \boldsymbol{aa}^\dagger \rangle = C_l \delta_{(lm)(l'm')}$. The distorted pseudo-$C_l$ spectrum is thus related to the true power spectrum, in ensemble-average, by

$$\langle \tilde{C}'_l \rangle = \frac{1}{2l+1} \sum_m \left\langle \left| a'_{lm} \right|^2 \right\rangle \equiv \sum_{l'} G_{ll'} \langle C_{l'} \rangle, \tag{B5}$$

where

$$G_{ll'} \equiv \frac{1}{2l+1} \sum_{mm'} \left| \mathcal{J}_{(lm)(l'm')} \right|^2 \tag{B6}$$

is the mode-coupling matrix. For cross-power spectra $\langle \boldsymbol{a}_1 \boldsymbol{a}_2^\dagger \rangle$, $|\mathcal{J}|^2$ is replaced by $\mathcal{J}_1 \mathcal{J}_2^*$, where $\mathcal{J}_1$ is evaluated with the weights and beam properties appropriate to channel 1, and so on. The unbiased power spectrum estimate is then $\sum_{l'} G_{ll'}^{-1} \tilde{C}'_{l'}$.

We now turn to the explicit evaluation of the distortion matrix $\mathcal{J}$. First, we assume that the time dependence of the beam response on the sky is due only to changes in the spacecraft orientation. That is, $g_i(p') = g(p_i, \alpha_i; p')$ where p_i is the pixel observed by the beam centroid during the ith observation, and α_i is the azimuth angle of the observation at that time. If we expand the spacecraft-fixed beam response in spherical harmonics,

$$g(\hat{z}, 0; p) = \sum_{lm} g_{lm} Y_{lm}(p), \tag{B7}$$

then the response on the sky may be expressed as

$$g_i(p') = \sum_{lmm'} D^l_{mm'}(p_i, \alpha_i) g_{lm'} Y_{lm}(p'), \tag{B8}$$

where the $D^l_{mm'}$ are the Wigner D-functions.

Since $\mathcal{J}$ is a linear function of $\boldsymbol{J}$, it follows that $\mathcal{J}(\boldsymbol{J}^\mathrm{A} + \boldsymbol{J}^\mathrm{B}) = \mathcal{J}^\mathrm{A} + \mathcal{J}^\mathrm{B}$. Furthermore, if $\boldsymbol{Q}$ is diagonal, we can write $\boldsymbol{J}^S$ (with S = A, B) as

$$\boldsymbol{J}^S_{pp'} = \frac{\Omega_p}{N_p} \sum_{i|S \in p} g^S_i(p') = \Omega_p \int \frac{d\alpha}{2\pi} w^S(p, \alpha) g^S(p, \alpha; p'), \tag{B9}$$

where

$$w^S(p, \alpha) = \boldsymbol{Q}_{pp} \frac{2\pi}{N_p} \sum_{i|S \in p} \delta(\alpha - \alpha_i). \tag{B10}$$

The Wigner D-functions form an orthogonal basis for functions defined over the three-dimensional rotation group, SO(3); thus we can expand $w^S(p, \alpha)$ as

$$w^S(p, \alpha) = \sum_{lmm'} w^{S,l}_{mm'} D^l_{mm'}(p, \alpha), \tag{B11}$$

where the sum is over all integral values of l, m, m'. Then, using the product rule

$$D^{l_1}_{m_1 m'_1}(p, \alpha) D^{l_2}_{m_2 m'_2}(p, \alpha) = \sum_{lmm'} C^{lm}_{l_1 m_1 l_2 m_2} C^{lm'}_{l_1 m'_1 l_2 m'_2} D^l_{mm'}(p, \alpha), \tag{B12}$$

[17] Here $\boldsymbol{Y}$ is the pixelized spherical harmonic transform matrix with elements $\boldsymbol{Y}_{p(lm)} = Y_{lm}(p)$, where p is the pixel index. It obeys $\boldsymbol{YY}^\dagger = \delta_{pp'}/\Omega_p$ and $\boldsymbol{Y}^\dagger \boldsymbol{Y} = \delta_{(lm)(l'm')}/\Omega_p$, where Ω_p is the pixel solid angle.

where the $C^{lm}_{l_1 m_1 l_2 m_2}$ are the Clebsch-Gordon coefficients, along with the fact that

$$\int \frac{d\alpha}{2\pi} D^l_{mm'}(p, \alpha) = \sqrt{\frac{4\pi}{2l+1}} Y^*_{lm}(p)\delta_{m'0}, \tag{B13}$$

we find

$$\boldsymbol{Q}_{pp}\boldsymbol{J}^S_{pp'} = \Omega_p \sum_{lm, l_1 m_1 m_1', l_2 m_2 m_2'} b^S_{l_1 m_1'} w^{S, l_2}_{m_2 m_2'} C^{lm}_{l_1 m_1 l_2 m_2} C^{l0}_{l_1 m_1' l_2 m_2'} \sqrt{\frac{2l_1+1}{2l+1}} Y^*_{lm}(p) Y_{l_1 m_1}(p'). \tag{B14}$$

Here we have defined $b_{lm} \equiv \sqrt{4\pi/(2l+1)}\, g_{lm}$, and we note that when the beams are circular $b_{lm} = b_l \delta_{m0}$, where b_l is the beam transfer function defined in Page et al. (2003a). Now, recalling that $\mathcal{J} = \Omega_p \boldsymbol{Y}^\dagger \boldsymbol{QJY}$, we have

$$\mathcal{J}^S_{(lm)(l_1 m_1)} = \sum_{m_1', l_2 m_2 m_2'} b^{S*}_{l_1 m_1'} w^{S, l_2 *}_{m_2 m_2'} C^{lm}_{l_1 m_1 l_2 m_2} C^{l0}_{l_1 m_1' l_2 m_2'} \sqrt{\frac{2l_1+1}{2l+1}}. \tag{B15}$$

Note that the sums over m_2 and m_2' effectively drop out of equation (B15), since the Clebsch-Gordon coefficients are zero unless $m_1 + m_2 = m$ and $m_1' + m_2' = 0$.

Calculating $G_{ll'}$ is now straightforward; for cross-power spectra, $\langle \boldsymbol{a}_1 \boldsymbol{a}_2^\dagger \rangle$, we can expand it as

$$G_{ll'} = G^{\mathrm{A_1 A_2}}_{ll'} + G^{\mathrm{A_1 B_2}}_{ll'} + G^{\mathrm{B_1 A_2}}_{ll'} + G^{\mathrm{B_1 B_2}}_{ll'}, \tag{B16}$$

where $\mathrm{A_1}$ refers to side A of channel 1, and so forth. Then, using

$$\sum_{mm_1} C^{lm}_{l_1 m_1 l_2 m_2} C^{lm}_{l_1 m_1 l_2' m_2'} = \delta_{l_2 l_2'} \delta_{m_2 m_2'} (2l+1)/(2l_2+1), \tag{B17}$$

we can write

$$G^{S_1 S_2}_{ll'} = \sum_{l_1 m_1} \frac{(\boldsymbol{I}^{S_1})^{ll'}_{l_1 m_1} (\boldsymbol{I}^{S_2 *})^{ll'}_{l_1 m_1}}{2l_1+1}, \tag{B18}$$

where

$$(\boldsymbol{I}^S)^{ll'}_{l_1 m_1} \equiv \sum_{m' m_1'} b^S_{l' m'} w^{S, l_1}_{m_1 m_1'} C^{l0}_{l' m' l_1 m_1'} \sqrt{\frac{2l'+1}{2l+1}}. \tag{B19}$$

In the case of uniform sky coverage, equation (B18) reduces to a familiar limit. Specifically, if all pixels are observed for the same length of time with a uniform distribution of azimuth angles, then $w(p, \alpha) = 1$, which gives $w^l_{mm'} = \delta_{l0}\delta_{m0}\delta_{m'0}$. This result, along with the identity $C^{lm}_{l'm'00} = \delta_{ll'}\delta_{mm'}$, gives $G_{ll'} = b^2_{l0}\delta_{ll'}$. Thus, even if the beams are not circularly symmetric, the full azimuthal coverage effectively symmetrizes the response.

If we retain full azimuthal coverage but introduce a mask, $w(p, \alpha) = q(p)$, we have

$$w^l_{mm'} = \frac{2l+1}{8\pi^2} \int d\Omega\, d\alpha\, q(p) D^{l*}_{mm'}(p, \alpha) \tag{B20}$$

$$= \sqrt{\frac{2l+1}{4\pi}} q_{lm}\, \delta_{m'0}, \tag{B21}$$

where the q_{lm} are the spherical harmonic coefficients of $q(p)$. Then, expressing the Clebsch-Gordon coefficients in terms of the Wigner 3j symbols,

$$C^{lm}_{l'm'l''m''} = (-1)^{m+l'+l''} \sqrt{2l+1} \begin{pmatrix} l' & l'' & l \\ m' & m'' & -m \end{pmatrix}, \tag{B22}$$

we can write

$$I^{ll'}_{l''m''} = b_{l'0} q_{l''m''} (-1)^{l'+l''} \begin{pmatrix} l' & l'' & l \\ 0 & 0 & 0 \end{pmatrix} \sqrt{\frac{(2l'+1)(2l''+1)}{4\pi}}, \tag{B23}$$

which gives the standard result for the coupling matrix (Hivon et al. 2002)

$$G_{ll'} = \sum_{l''m''} \frac{2l'+1}{4\pi} b_{l'0}^2 |q_{l''m''}|^2 \begin{pmatrix} l' & l'' & l \\ 0 & 0 & 0 \end{pmatrix}^2. \tag{B24}$$

Note that the beam window function is naturally incorporated in this expression, because of the way the mapping matrix was defined. This result also generalizes to the case of nonuniform noise per pixel by allowing the mask function, $q(p)$, to become a weight map. Finally, if the beams are circularly symmetric, we can drop the requirement that pixels be observed with uniform azimuthal weight and derive the same result.

B2. RESULTS

Evaluating equation (B18) requires $\mathcal{O}(l_{\max}^5)$ operations and is thus impractical when $l_{\max} \sim 10^3$. However, if we ignore sky cuts and apply a uniform sky weight, $\boldsymbol{Q} = \boldsymbol{I}$, we can exploit an approximate symmetry of the *WMAP* scan pattern to significantly speed up the calculation. Specifically, the *WMAP* scan strategy is approximately independent of ecliptic longitude, implying $w^S(\theta, \phi, \alpha) \approx w^S(\theta, 0, \alpha)$ where θ and ϕ are ecliptic latitude and longitude, respectively. This eliminates the sum over m_1 in equation (B18).

The weight coefficients are

$$w_{mm'}^{S,l} = \frac{2l+1}{8\pi^2} \int d\Omega\, d\alpha\, w^S(\theta, \phi, \alpha) D_{mm'}^{l*}(\theta, \phi, \alpha), \tag{B25}$$

and since

$$D_{0m'}^{l*}(\theta, \phi, \alpha) = \sqrt{\frac{4\pi}{2l+1}} Y_{l,-m'}^*(\theta, \alpha), \tag{B26}$$

the weight coefficients simplify to

$$w_{mm'}^{S,l} = \delta_{m0} \sqrt{\frac{2l+1}{4\pi}} \tilde{w}_{l,-m'}^S \tag{B27}$$

where

$$\tilde{w}_{lm'}^S = \int d(\cos\theta)\, d\alpha\, w^S(\theta, \alpha) Y_{lm}^*(\theta, \alpha) \tag{B28}$$

is a standard spherical harmonic transform. Then

$$(\boldsymbol{I}^S)_{l''m''}^{ll'} = \delta_{m''0} \sqrt{\frac{(2l'+1)(2l''+1)}{4\pi}} \sum_{m'} b_{l'm'}^S \tilde{w}_{l''m'}^S \begin{pmatrix} l' & l'' & l \\ m' & -m' & 0 \end{pmatrix} (-1)^{l'+l''}, \tag{B29}$$

and

$$G_{ll'}^{S_1 S_2} = \frac{2l'+1}{4\pi} \sum_{l''m'm''} b_{l'm'}^{S_1} \tilde{w}_{l''m'}^{S_1} b_{l'm''}^{S_2 *} \tilde{w}_{l''m''}^{S_2 *} \begin{pmatrix} l' & l'' & l \\ m' & -m' & 0 \end{pmatrix} \begin{pmatrix} l' & l'' & l \\ m'' & -m'' & 0 \end{pmatrix}. \tag{B30}$$

If the sums over m', m'' are truncated at $m_{\max}$, this requires $\mathcal{O}(m_{\max} l_{\max}^3)$ operations. For elliptical beams, b_{lm} falls off rapidly with m, becoming negligible for $m \gtrsim 6$.

To quantify how beam asymmetry distorts the power spectrum, we compute the ratio

$$\alpha_l \equiv \frac{1}{b_l^i b_l^{i'} C_l^{\text{fid}}} \sum_{l'} G_{ll'}^{\boldsymbol{i}} C_{l'}^{\text{fid}}, \tag{B31}$$

where C_l^{fid} is a fiducial power spectrum, b_l^i is the symmetrized beam transfer function noted above, and $G_{ll'}^{\boldsymbol{i}}$ is the coupling matrix appropriate to cross-power spectrum $\boldsymbol{i}$ (this index notation is defined in § 7.1). The matrices $G_{ll'}$ were computed using the 3 year sky coverage with beam transforms derived from the hybrid beam maps (Jarosik et al. 2007), and with $l_{\max} = 1500$, $m_{\max} = 16$. The asymmetry corrections for each of the Q-, V-, and W-band auto- and cross-power spectra are shown in Figure 23. The QQ spectrum show the largest effect (6.3% at $l = 600$), because the Q-band beams are relatively elliptical. For example, the FWHM along the major and minor axes of the Q2A beam are 0.60° and 0.42°, respectively. The rise of α_l at high l indicates that the symmetric window underestimates the power in the beam, and thus overestimates the power spectrum. Because of the magnitude of this effect in the Q-band data, and because

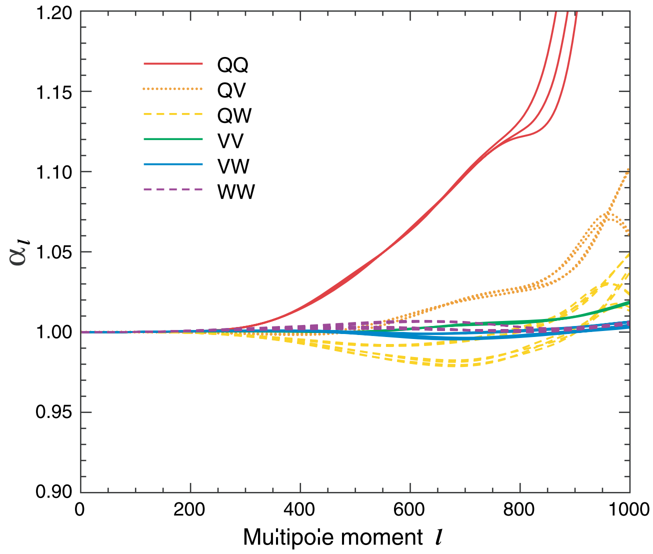

FIG. 23.—Estimate of the multiplicative error introduced in the angular power spectrum, C_l, due to the effects of beam asymmetry. See § 7.1.1 and Appendix B for details on how this estimate was obtained. Note that the final power spectrum does not include data from the Q band.

of the large foreground correction needed at low-l, Q-band were excluded from the final combined power spectrum. The corrections to the V- and W-band spectra are all $\lesssim 1\%$ for $l < 1000$.

APPENDIX C

MAXIMUM LIKELIHOOD NOTES

C1. THE GENERAL CASE WITHOUT NOISE

The log of the likelihood function has the form

$$-2 \ln L(\boldsymbol{d}|\boldsymbol{m}) = \chi^2 + \ln \det \boldsymbol{C}, \tag{C1}$$

where $\boldsymbol{d}$ is the data, which is assumed to be drawn from a multivariate Gaussian distribution, $\boldsymbol{m}$ is a set of model parameters, and $\boldsymbol{C}$ is the covariance matrix of the data. In the limit of no noise and full sky coverage, it is convenient to represent the data in terms of the spherical harmonic coefficients, $\boldsymbol{d} = \boldsymbol{a} \equiv a_{lm}$, in which case

$$\boldsymbol{C} = \mathrm{diag}[C_0, C_1, \ldots, C_2, \ldots] \tag{C2}$$

and

$$\chi^2 = \boldsymbol{a}^T \cdot \boldsymbol{C}^{-1} \cdot \boldsymbol{a} = \sum_{lm} \frac{|a_{lm}|^2}{C_l}, \tag{C3}$$

where C_l is the power spectrum that encodes the variance of the a_{lm} coefficients,

$$\langle a_{lm} a^*_{lm} \rangle = C_l \delta_{ll'} \delta_{mm'}. \tag{C4}$$

It is straightforward to show that the maximum likelihood estimate of the power spectrum, C_l^{ML}, is given by

$$C_l^{\mathrm{ML}} = \sum_{m=-l}^{l} \frac{|a_{lm}|^2}{2l+1}. \tag{C5}$$

To set up the case of incomplete sky coverage, consider a new representation of the data which is related to $\boldsymbol{a}$ by a simple linear transformation

$$\boldsymbol{d} = \boldsymbol{L} \cdot \boldsymbol{a}, \tag{C6}$$

where $\boldsymbol{L}$ is an $N_d \times (l_{\max} + 1)^2$ matrix, N_d is the number of points in $\boldsymbol{d}$, and $l_{\max}$ is the maximum spherical harmonic order being analyzed. For example, if $\boldsymbol{d} = \boldsymbol{t}$ is a sky map, the matrix $\boldsymbol{L} = \boldsymbol{Y}$ is the matrix of spherical harmonics evaluated at each pixel i. (We need not assume that $\boldsymbol{t}$ covers the full sky.)

The likelihood of $\boldsymbol{d}$, given the model spectrum, C_l, is

$$-2 \ln L(\boldsymbol{d}|\boldsymbol{m}) = \boldsymbol{d}^T \cdot \tilde{\boldsymbol{C}}^{-1} \cdot \boldsymbol{d} + \ln \det \tilde{\boldsymbol{C}}, \tag{C7}$$

where $\tilde{\boldsymbol{C}}$ is is the covariance matrix of $\boldsymbol{d}$, which has the form

$$\tilde{\boldsymbol{C}} = \langle \boldsymbol{d}\boldsymbol{d}^T \rangle = \boldsymbol{L} \cdot \langle \boldsymbol{a}\boldsymbol{a}^T \rangle \cdot \boldsymbol{L}^T = \boldsymbol{L} \cdot \boldsymbol{C} \cdot \boldsymbol{L}^T, \tag{C8}$$

with

$$\tilde{\boldsymbol{C}}^{-1} = (\boldsymbol{L}^T)^{-1} \cdot \boldsymbol{C}^{-1} \cdot \boldsymbol{L}^{-1}. \tag{C9}$$

The determinant of $\tilde{\boldsymbol{C}}$ factors as

$$\ln \det \tilde{\boldsymbol{C}} = \ln (\det \boldsymbol{L} \det \boldsymbol{C} \det \boldsymbol{L}^T) = \ln \det \boldsymbol{C} + \ln (\det \boldsymbol{L})^2, \tag{C10}$$

and since $\boldsymbol{C}$ is diagonal and $\boldsymbol{L}$ is independent of C_l, this reduces to

$$\ln \det \tilde{\boldsymbol{C}} = \sum_{lm} \ln C_l + \text{const.} \tag{C11}$$

Thus we can rewrite the likelihood as

$$-2 \ln L(\boldsymbol{d}|\boldsymbol{m}) = (\boldsymbol{L}^{-1}\boldsymbol{d})^T \cdot \boldsymbol{C}^{-1} \cdot (\boldsymbol{L}^{-1}\boldsymbol{d}) + \ln \det \boldsymbol{C} + \text{const.} \tag{C12}$$

This form is a trivial recasting of the original form of L in terms of $\boldsymbol{L}^{-1}\boldsymbol{d}$. By the same argument that led to equation (C5), we have the following expression for the maximum likelihood estimate of C_l:

$$C_l^{\text{ML}} = \sum_{m=-l}^{l} \frac{|(\boldsymbol{L}^{-1}\boldsymbol{d})_{lm}|^2}{2l+1}. \tag{C13}$$

So, in the limit of no noise, a complete maximum likelihood estimate of the low-l spectrum requires only a single matrix inversion to evaluate $\boldsymbol{L}^{-1}$. This enables very rapid computation of the likelihood, and it isolates the source of systematic errors to the form of $\boldsymbol{L}$ and its inverse.

C2. THE PSEUDO-a_{lm} CASE

One representation of the data are the pseudo-a_{lm} coefficients, $\tilde{a}_{lm}$, which are obtained by transforming the data on the cut sky

$$\tilde{a}_{lm} = \sum_i w_i \, Y_{lm}^*(\hat{n}_i) t_i, \tag{C14}$$

where the sum is over all pixels i, w_i is the weight per pixel, which includes any mask applied, $Y_{lm}^*(\hat{n}_i)$ is the spherical harmonic in the direction of pixel i, and t_i is the temperature in pixel i. If we expand the temperature in spherical harmonics, we can express the $\tilde{a}_{lm}$ in terms of the true a_{lm} coefficients as

$$\tilde{a}_{lm} = \sum_i w_i \, Y_{lm}^*(\hat{n}_i) \sum_{l'm'} a_{l'm'} Y_{l'm'}(\hat{n}_i) = \sum_{l'm'} M_{(lm)(lm)'} a_{l'm'}, \tag{C15}$$

where the coupling matrix is defined as

$$M_{(lm)(lm)'} \equiv \sum_i w_i \, Y_{lm}^*(\hat{n}_i) Y_{l'm'}(\hat{n}_i), \tag{C16}$$

which depends only on the weight array, $\boldsymbol{w}$. (If one expands $\boldsymbol{w}$ in spherical harmonics, the coupling matrix can be expressed in terms of the Wigner $3j$ symbols, but this form is not especially useful in this context.) We express the pseudo-a_{lm} in matrix notation as $\tilde{\boldsymbol{a}} = \boldsymbol{M} \cdot \boldsymbol{a}$, which has the same form as equation (C6). It follows that the maximum likelihood solution for C_l is then

$$C_l^{\text{ML}} = \sum_{m=-l}^{l} \frac{|(\boldsymbol{M}^{-1}\tilde{\boldsymbol{a}})_{lm}|^2}{2l+1}. \tag{C17}$$

In practice, the coupling matrix depends on both $l_{\rm max}$ and $l'_{\rm max}$, the harmonic orders to which the true and pseudo-a_{lm} are analyzed, respectively. In general $\boldsymbol{M}$ need not be square. It is instructive to look at the structure of $\boldsymbol{M}$ using SVD,

$$\tilde{\boldsymbol{a}} = \boldsymbol{M} \cdot \boldsymbol{a} = \boldsymbol{u}\boldsymbol{w}\boldsymbol{v}^T \cdot \boldsymbol{a}. \tag{C18}$$

Since $\boldsymbol{u}$ and $\boldsymbol{v}$ are orthogonal, the values of $\boldsymbol{w}$ encode the level of deprojection that occurs when solving for $\boldsymbol{a} = \boldsymbol{M}^{-1} \cdot \tilde{\boldsymbol{a}}$. Specifically, since

$$\boldsymbol{M}^{-1} = \boldsymbol{v}\boldsymbol{w}^{-1}\boldsymbol{u}^T, \tag{C19}$$

it follows that pseudo-a_{lm} modes corresponding to small values of $\boldsymbol{w}$ will be greatly amplified in the recovery of the true a_{lm}. Thus small errors in the $\tilde{a}_{lm}$ can be also be greatly magnified. In the case of full sky, $\boldsymbol{w} = 1$, while for the Kp2 cut sky and $l_{\rm max} = l'_{\rm max} = 10$, we find $0.05 < \boldsymbol{w} < 1$. Note also that any error in the $\tilde{a}_{lm}$ will bias the estimate of C_l obtained with this method, since the estimator for $C_l^{\rm ML}$ is quadratic.

C3. THE PIXEL-SPACE CASE

As noted above, the data may be represented as a (cut) sky map, $\boldsymbol{t}$, which can be expanded in spherical harmonics, $\boldsymbol{t} = \boldsymbol{Y} \cdot \boldsymbol{a}$. Here $\boldsymbol{Y}$ is an $N_{\rm pix} \times (l_{\rm max} + 1)^2$ matrix of spherical harmonic functions evaluated at each pixel i that survives the sky cut.

The likelihood of $\boldsymbol{t}$, given the model spectrum, C_l, is

$$-2 \ln L(\boldsymbol{t}|\boldsymbol{m}) = \boldsymbol{t}^T \cdot \hat{\boldsymbol{C}}^{-1} \cdot \boldsymbol{t} + \ln \det \hat{\boldsymbol{C}}, \tag{C20}$$

where $\hat{\boldsymbol{C}}$ is the covariance matrix of $\boldsymbol{t}$ which has the form

$$\hat{\boldsymbol{C}} = \langle \boldsymbol{t}\boldsymbol{t}^T \rangle = \boldsymbol{Y} \cdot \langle \boldsymbol{a}\boldsymbol{a}^T \rangle \cdot \boldsymbol{Y}^T = \boldsymbol{Y} \cdot \boldsymbol{C} \cdot \boldsymbol{Y}^T. \tag{C21}$$

This may be expressed in the more familiar form of the two-point correlation function, $C(\theta_{ij})$

$$\hat{\boldsymbol{C}}_{ij} = C(\theta_{ij}) = \sum_l \frac{2l+1}{4\pi} C_l P_l(\cos\theta_{ij}) = \sum_{lm} C_l\, Y^*_{lm}(\hat{n}_i) Y_{lm}(\hat{n}_j). \tag{C22}$$

where the last equality follows from the addition theorem for spherical harmonics. The inverse of $\hat{\boldsymbol{C}}$ has the form

$$\hat{\boldsymbol{C}}^{-1} = (\boldsymbol{Y}^T)^{-1} \cdot \boldsymbol{C}^{-1} \cdot \boldsymbol{Y}^{-1}, \tag{C23}$$

and the determinant of $\hat{\boldsymbol{C}}$ factors as

$$\ln \det \hat{\boldsymbol{C}} = \ln(\det \boldsymbol{Y} \det \boldsymbol{C} \det \boldsymbol{Y}^T) = \ln \det \boldsymbol{C} + \ln(\det \boldsymbol{Y})^2 = \ln \det \boldsymbol{C} + \text{const}. \tag{C24}$$

Thus

$$-2 \ln L(\boldsymbol{t}|\boldsymbol{m}) = (\boldsymbol{Y}^{-1}\boldsymbol{t})^T \cdot \boldsymbol{C}^{-1} \cdot (\boldsymbol{Y}^{-1}\boldsymbol{t}) + \ln \det \boldsymbol{C} + \text{const}, \tag{C25}$$

and

$$C_l^{\rm ML} = \sum_{m=-l}^{l} \frac{|(\boldsymbol{Y}^{-1}\boldsymbol{t})_{lm}|^2}{2l+1}. \tag{C26}$$

What is the nature of $\boldsymbol{Y}^{-1}$? In the limit of full sky coverage the spherical harmonics form an orthonormal basis,

$$\sum_i Y^*_{lm}(\hat{n}_i) Y_{l'm'}(\hat{n}_i) = \delta_{ll'}\delta_{mm'}, \tag{C27}$$

or $\boldsymbol{Y}^T \cdot \boldsymbol{Y} = \boldsymbol{I}$, where $\boldsymbol{I}$ is the identity matrix. In this limit $\boldsymbol{Y}$ is orthogonal, $\boldsymbol{Y}^{-1} = \boldsymbol{Y}^T$, and $\boldsymbol{Y}^{-1}\boldsymbol{t} = \boldsymbol{Y}^T\boldsymbol{t}$ is just the spherical harmonic transform of $\boldsymbol{t}$.

More generally, in the presence of a sky cut, we can relate the pixel space formalism to the pseudo-a_{lm} formalism as follows. The pseudo-a_{lm} coefficients may be written as

$$\tilde{\boldsymbol{a}} = \boldsymbol{Y}^T \cdot \boldsymbol{t} = \boldsymbol{Y}^T\boldsymbol{Y} \cdot \boldsymbol{a} = \boldsymbol{M} \cdot \boldsymbol{a}, \tag{C28}$$

where $\boldsymbol{M} = \boldsymbol{Y}^T\boldsymbol{Y}$ is the coupling matrix defined in equation (C16). Note that we are now implicitly assuming that the sky mask, $\boldsymbol{w}$, is sharp, in the sense that it consists of only 1's or 0's. The case of an apodized mask needs to be studied further. It follows that

$$\boldsymbol{a} = \boldsymbol{M}^{-1} \cdot \tilde{\boldsymbol{a}} = (\boldsymbol{Y}^T\boldsymbol{Y})^{-1}\boldsymbol{Y}^T \cdot \boldsymbol{t} = \boldsymbol{Y}^{-1}(\boldsymbol{Y}^T)^{-1}\boldsymbol{Y}^T \cdot \boldsymbol{t} = \boldsymbol{Y}^{-1} \cdot \boldsymbol{t}, \tag{C29}$$

thus $\boldsymbol{Y}^{-1} = \boldsymbol{M}^{-1}\boldsymbol{Y}^T$ (this reduces to $\boldsymbol{Y}^{-1} = \boldsymbol{Y}^T$ in the limit of full sky coverage). The relations in equation (C29) establish the equivalence of equation (C17) and equation (C26) in the case of a sharp mask. Note also that equation (C26) is the same expression one would get by least-squares fitting the a_{lm} coefficients on the cut sky (with uniform weight outside the cut) and summing them to get the power spectrum.

Since $\boldsymbol{Y}^{-1} = \boldsymbol{M}^{-1}\boldsymbol{Y}^T$, the essential numerical features of the maximum likelihood estimates are encoded in the coupling matrix $\boldsymbol{M}$. Specifically, one must ensure that $\boldsymbol{M}^{-1}$ has sufficient range to adequately capture the harmonic content in the pseudo-a_{lm} data.

REFERENCES

Afshordi, N., Lin, Y.-T., & Sanderson, A. J. R. 2005, ApJ, 629, 1
Afshordi, N., Loh, Y.-S., & Strauss, M. A. 2004, Phys. Rev. D, 69, 083524
Arendt, R., et al. 1998, ApJ, 508, 74
Atrio-Barandela, F., & Muecket, J. P. 2006, ApJ, 643, 1
Barnes, C., et al. 2002, ApJS, 143, 567
———. 2003, ApJS, 148, 51
Beck, R., & Golla, G. 1988, A&A, 191, L9
Bennett, C. L., et al. 2003a, ApJ, 583, 1
———. 2003b, ApJS, 148, 1
———. 2003c, ApJS, 148, 97
Bicay, M. D., Helou, G., & Condon, J. J. 1989, ApJ, 338, L53
Bielewicz, P., Gorski, K. M., & Banday, A. J. 2004, MNRAS, 355, 1283
Biermann, P. 1976, A&A, 53, 295
Bond, J. R., Jaffe, A. H., & Knox, L. 1998, Phys. Rev. D, 57, 2117
Borrill, J. 1999, Phys. Rev. D, 59, 27302
Boughn, S. P., Cheng, E. S., Cottingham, D. A., & Fixsen, D. J. 1992, ApJ, 391, L49
Bressan, A., Silva, L., & Granato, G. L. 2002, A&A, 392, 377
Briel, U. G., Henry, J. P., & Boehringer, H. 1992, A&A, 259, L31
Casassus, S., Readhead, A. C. S., Pearson, T. J., Nyman, L.-Å., Shepherd, M. C., & Bronfman, L. 2004, ApJ, 603, 599
Chi, X., & Wolfendale, A. W. 1990, MNRAS, 245, 101
Cleary, K. A., et al. 2005, MNRAS, 360, 340
Condon, J. J. 1992, ARA&A, 30, 575
Copi, C. J., Huterer, D., & Starkman, G. D. 2004, Phys. Rev. D, 70, 043515
de Jong, T., Klein, U., Wielebinski, R., & Wunderlich, E. 1985, A&A, 147, L6
de Oliveira-Costa, A., Kogut, A., Devlin, M. J., Netterfield, C. B., Page, L. A., & Wollack, E. J. 1997, ApJ, 482, L17
de Oliveira-Costa, A., Tegmark, M., Davies, R. D., Gutiérrez, C. M., Lasenby, A. N., Rebolo, R., & Watson, R. A. 2004a, ApJ, 606, L89
de Oliveira-Costa, A., Tegmark, M., Devlin, M. J., Page, L., Miller, A. D., Netterfield, C. B., & Xu, Y. 2005, Phys. Rev. D, 71, 043004
de Oliveira-Costa, A., Tegmark, M., Page, L., & Boughn, S. 1998, ApJ, 509, L9
de Oliveira-Costa, A., Tegmark, M., Zaldarriaga, M., & Hamilton, A. 2004b, Phys. Rev. D, 69, 063516
de Oliveira-Costa, A., et al. 1999, ApJ, 527, L9
———. 2002, ApJ, 567, 363
———. 2004c, ApJ, 606, L89
de Zotti, G., Ricci, R., Mesa, D., Silva, L., Mazzotta, P., Toffolatti, L., & González-Nuevo, J. 2005, A&A, 431, 893
Dennison, B., Simonetti, J. H., & Topasna, G. A. 1998, Publ. Astron. Soc. Australia, 15, 147
Devereux, N. A., & Eales, S. A. 1989, ApJ, 340, 708
Dickey, J. M., & Salpeter, E. E. 1984, ApJ, 284, 461
Dickinson, C., et al. 2004, MNRAS, 353, 732
Draine, B. T., & Lazarian, A. 1998, ApJ, 494, L19
———. 1999, ApJ, 512, 740
Ebeling, H., Voges, W., Bohringer, H., Edge, A. C., Huchra, J. P., & Briel, U. G. 1996, MNRAS, 281, 799
Efstathiou, G. 2003, MNRAS, 346, L26
———. 2004a, MNRAS, 348, 885
———. 2004b, MNRAS, 349, 603
Erickson, W. C. 1957, ApJ, 126, 480
Eriksen, H. K., Banday, A. J., Górski, K. M., & Lilje, P. B. 2004a, ApJ, 612, 633
Eriksen, H. K., Hansen, F. K., Banday, A. J., Gorski, K. M., & Lilje, P. B. 2004b, ApJ, 605, 14
Eriksen, H. K., et al. 2004c, ApJS, 155, 227
———. 2007, ApJ, 656, 641
Fernandez-Cerezo, S., Gutierrez, C. M., Rebolo, R., Watson, R. A., Hoyland, R. J., Hildebrandt, S., Rubiño-Martín, J. A., Macias-Perez, J. F., & Sosa Molina, P. 2006, MNRAS, 370, 15
Finkbeiner, D. P. 2003, ApJS, 146, 407
Finkbeiner, D. P., Davis, M., & Schlegel, D. J. 1999, ApJ, 524, 867 (FDS99)
Finkbeiner, D. P., Schlegel, D. J., Frank, C., & Heiles, C. 2002, ApJ, 566, 898
Fitt, A. J., Alexander, P., & Cox, M. J. 1988, MNRAS, 233, 907
Fosalba, P., & Gaztañaga, E. 2004, MNRAS, 350, L37
Fosalba, P., Gaztanaga, E., & Castander, F. 2003, ApJ, 597, L89
Fosalba, P., & Szapudi, I. 2004, ApJ, 617, L95
Gaustad, J. E., McCullough, P. R., Rosing, W., & Buren, D. V. 2001, PASP, 113, 1326
Gavazzi, G., Cocito, A., & Vettolani, G. 1986, ApJ, 305, L15
Gaztanaga, E., Wagg, J., Multamaki, T., Montana, A., & Hughes, D. H. 2003, MNRAS, 346, 47
Gorski, K. M., Hivon, E., Banday, A. J., Wandelt, B. D., Hansen, F. K., Reinecke, M., & Bartlemann, M. 2005, ApJ, 622, 759
Gregory, P. C., Scott, W. K., Douglas, K., & Condon, J. J. 1996, ApJS, 103, 427
Griffith, M. R., Wright, A. E., Burke, B. F., & Ekers, R. D. 1994, ApJS, 90, 179
———. 1995, ApJS, 97, 347
Gutiérrez, C. M., et al. 2000, ApJ, 529, 47
Haffner, L. M., et al. 2003, ApJS, 149, 405
Hamilton, A. J. S. 1997a, MNRAS, 289, 285
———. 1997b, MNRAS, 289, 295
Hansen, F. K., Balbi, A., Banday, A. J., & Gorski, K. M. 2004a, MNRAS, 354, 905
Hansen, F. K., Banday, A. J., & Gorski, K. M. 2004b, MNRAS, 354, 641
Hansen, F. K., Branchini, E., Mazzotta, P., Cabella, P., & Dolag, K. 2005, MNRAS, 361, 753
Haslam, C. G. T., Klein, U., Salter, C. J., Stoffel, H., Wilson, W. E., Cleary, M. N., Cooke, D. J., & Thomasson, P. 1981, A&A, 100, 209
Hauser, M. G., & Peebles, P. J. E. 1973, ApJ, 185, 757
Helou, G., Soifer, B. T., & Rowan-Robinson, M. 1985, ApJ, 298, L7
Herbig, T., Lawrence, C. R., Readhead, A. C. S., & Gulkis, S. 1995, ApJ, 449, L5
Hernández-Monteagudo, C., & Rubiño-Martín, J. A. 2004, MNRAS, 347, 403
Hernández-Monteagudo, C., Genova-Santos, R., & Atrio-Barandela, F. 2004, ApJ, 613, L89
Hinshaw, G., Branday, A. J., Bennett, C. L., Górski, K. M., Kogut, A., Lineweaver, C. H., Smoot, G. F., & Wright, E. L. 1996, ApJ, 464, L25
Hinshaw, G., et al. 2003a, ApJS, 148, 63
———. 2003b, ApJS, 148, 135
Hirabayashi, H., et al. 2000, PASJ, 52, 997
Hivon, E., Górski, K. M., Netterfield, C. B., Crill, B. P., Prunet, S., & Hansen, F. 2002, ApJ, 567, 2
Huffenberger, K. M., Eriksen, H. K., & Hansen, F. K. 2006, ApJ, 651, L81
Hummel, E. 1986, A&A, 160, L4
Hummel, E., Dahlem, M., van der Hulst, J. M., & Sukumar, S. 1991, A&A, 246, 10
Hummel, E., Davies, R. D., Pedlar, A., Wolstencroft, R. D., & van der Hulst, J. M. 1988, A&A, 199, 91
Jarosik, N., et al. 2003a, ApJS, 148, 29
———. 2003b, ApJS, 145, 413
———. 2007, ApJS, 170, 263
Jones, W. C., et al. 2006, ApJ, 647, 823
Katz, G., & Weeks, J. 2004, Phys. Rev. D, 70, 063527
Kogut, A., Banday, A. J., Bennett, C. L., Górski, K. M., Hinshaw, G., & Reach, W. T. 1996a, ApJ, 460, 1
Kogut, A., Banday, A. J., Bennett, C. L., Górski, K. M., Hinshaw, G., Smoot, G. F., & Wright, E. I. 1996b, ApJ, 464, L5
Kogut, A., et al. 2003, ApJS, 148, 161
Komatsu, E., & Seljak, U. 2002, MNRAS, 336, 1256
Komatsu, E., et al. 2003, ApJS, 148, 119
Kühr, H., Witzel, A., Pauliny-Toth, I. I. K., & Nauber, U. 1981, A&AS, 45, 367
Kuo, C. L., et al. 2004, ApJ, 600, 32

Land, K., & Magueijo, J. 2005, Phys. Rev. Lett., 95, 071301
Landt, H., Padovani, P., Perlman, E. S., Giommi, P., Bignall, H., & Tzioumis, A. 2001, MNRAS, 323, 757
Lawson, K. D., Mayer, C. J., Osborne, J. L., & Parkinson, M. L. 1987, MNRAS, 225, 307
Leitch, E. M. 1998, Ph.D. thesis, California Inst. Technology
Leitch, E. M., Readhead, A. C. S., Pearson, T. J., & Myers, S. T. 1997, ApJ, 486, L23
Leitch, E. M., Readhead, A. C. S., Pearson, T. J., Myers, S. T., Gulkis, S., & Lawrence, C. R. 2000, ApJ, 532, 37
Lewis, A. 2004, in Observing, Thinking and Mining the Universe, ed. G. Miele & G. Longo (Singapore: World Scientific), 217
Lewis, A., Challinor, A., & Lasenby, A. 2000, ApJ, 538, 473
Limon, M., et al. 2003, *Wilkinson Microwave Anisotropy Probe* (*WMAP*): Explanatory Supplement (Baltimore: GSFC), http://lambda.gsfc.nasa.gov/product/map/dr2/map_bibliography.cfm
———. 2006, *Wilkinson Microwave Anisotropy Probe* (*WMAP*): Explanatory Supplement (Baltimore: GSFC), http://lambda.gsfc.nasa.gov/product/map/dr2/map_bibliography.cfm
Lisenfeld, U., & Völk, H. J. 2000, A&A, 354, 423
Martin, J., & Ringeval, C. 2004, Phys. Rev. D, 69, 083515
———. 2005, J. Cosmol. Astropart. Phys., 1, 7
Mason, B. S., et al. 2003, ApJ, 591, 540
Mather, J. C., Fixsen, D. J., Shafer, R. A., Mosier, C., & Wilkinson, D. T. 1999, ApJ, 512, 511
McCullough, P. R., & Chen, R. R. 2002, ApJ, 566, L45
Mirabel, I. F., & Sanders, D. B. 1988, ApJ, 335, 104
Mitra, S., Sengupta, A. S., & Souradeep, T. 2004, Phys. Rev. D, 70, 103002
Myers, A. D., Shanks, T., Outram, P. J., Frith, W. J., & Wolfendale, A. W. 2004, MNRAS, 347, L67
Niarchou, A., Jaffe, A. H., & Pogosian, L. 2004, Phys. Rev. D, 69, 063515
Nolta, M. R., et al. 2004, ApJ, 608, 10
O'Dwyer, I. J., et al. 2004, ApJ, 617, L99
Oh, S. P., Spergel, D. N., & Hinshaw, G. 1999, ApJ, 510, 551
Page, L., et al. 2003a, ApJS, 148, 39
———. 2003b, ApJ, 585, 566
———. 2003c, ApJS, 148, 233
———. 2007, ApJS, 170, 335
Patanchon, G. 2003, NewA Rev., 47, 871
Peebles, P. J. E. 1973, ApJ, 185, 413
Peebles, P. J. E., & Hauser, M. G. 1974, ApJS, 28, 19
Peiris, H. V., et al. 2003, ApJS, 148, 213
Perlman, E. S., Padovani, P., Giommi, P., Sambruna, R., Jones, L. R., Tzioumis, A., & Reynolds, J. 1998, AJ, 115, 1253
Polenta, G., Marinucci, D., Balbi, A., de Bernardis, P., Hivon, E., Masi, S., Natoli, P., & Vittorio, N. 2005, J. Cosmol. Astropart. Phys., 11, 1
Press, W. H., Teukolsky, S. A., Vetterling, W. T., & Flannery, B. P. 1992, Numerical Recipes in C (2nd ed.; Cambridge: Cambridge Univ. Press)
Readhead, A. C. S., et al. 2004, ApJ, 609, 498
Refregier, A., Spergel, D. N., & Herbig, T. 2000, ApJ, 531, 31
Rengelink, R. B., et al. 1997, A&AS, 124, 259
Reynolds, R. J., Haffner, L. M., & Madsen, G. J. 2002, in ASP Conf. Ser. 282, Galaxies: The Third Dimension, ed. M. Rosado, L. Binette, & L. Arias (San Francisco: ASP), 31
Ricci, R., Sadler, E. M., Ekers, R. D., Staveley-Smith, L., Wilson, W. E., Kesteven, M. J., Subrahmanyan, R., Walker, M. A., Jackson, C. A., & De Zotti, G. 2004, MNRAS, 354, 305
Sanders, D. B., & Mirabel, I. F. 1985, ApJ, 298, L31
Schlegel, D. J., Finkbeiner, D. P., & Davis, M. 1998, ApJ, 500, 525 (SFD)
Schwarz, D. J., Starkman, G. D., Huterer, D., & Copi, C. J. 2004, Phys. Rev. Lett., 93, 221301
Seljak, U., & Zaldarriaga, M. 1996, ApJ, 469, 437
Shafieloo, A., & Souradeep, T. 2004, Phys. Rev. D, 70, 043523
Slosar, A., Seljak, U., & Makarov, A. 2004, Phys. Rev. D, 69, 123003
Souradeep, T., & Ratra, B. 2001, ApJ, 560, 28
Spergel, D. N., et al. 2003, ApJS, 148, 175
———. 2007, ApJS, 170, 377
Stickel, M., Meisenheimer, K., & Kühr, H. 1994, A&AS, 105, 211
Tegmark, M. 1997, Phys. Rev. D, 55, 5895
Tegmark, M., & de Oliveira-Costa, A. 1998, ApJ, 500, L83
Tegmark, M., de Oliveira-Costa, A., & Hamilton, A. J. 2003, Phys. Rev. D, 68, 123523
Tegmark, M., & Efstathiou, G. 1996, MNRAS, 281, 1297
Teräsranta, H., Urpo, S., Wiren, S., & Valtonen, M. 2001, A&A, 368, 431
Tocchini-Valentini, D., Hoffman, Y., & Silk, J. 2006, MNRAS, 367, 1095
Toffolatti, L., Argueso Gomez, F., de Zotti, G., Mazzei, P., Franceschini, A., Danese, L., & Burigana, C. 1998, MNRAS, 297, 117
Tristram, M., Macias-Perez, J. F., Renault, C., & Santos, D. 2005, MNRAS, 358, 833
Trushkin, S. A. 2003, Bull. Spec. Astrophys. Obs. N. Caucasus, 55, 90
Ulvestad, J. S. 1982, ApJ, 259, 96
Unger, S. W., Wolstencroft, R. D., Pedlar, A., Savage, A., Clowes, R. G., Leggett, S. K., & Parker, Q. A. 1989, MNRAS, 236, 425
Verde, L., et al. 2003, ApJS, 148, 195
Voelk, H. J. 1989, A&A, 218, 67
Waldram, E. M., Pooley, G. G., Grainge, K. J. B., Jones, M. E., Saunders, R. D. E., Scott, P. F., & Taylor, A. C. 2003, MNRAS, 342, 915
Wandelt, B. D., & Górski, K. M. 2001, Phys. Rev. D, 63, 123002
Wandelt, B. D., Hivon, E., & Górski, K. M. 2001, Phys. Rev. D, 64, 083003
Wright, A. E., Griffith, M. R., Burke, B. F., & Ekers, R. D. 1994, ApJS, 91, 111
Wright, A. E., Griffith, M. R., Hunt, A. J., Troup, E., Burke, B. F., & Ekers, R. D. 1996, ApJS, 103, 145
Wu, J. H. P., Balbi, A., Borrill, J., Ferreira, P. G., Hanany, S., Jaffe, A. H., Lee, A. T., Oh, S., Rabii, B., Richards, P. L., Smoot, G. F., Stompor, R., & Winant, C. D. 2001, ApJS, 132, 1
Wunderlich, E., & Klein, U. 1988, A&A, 206, 47
———. 1991, A&AS, 87, 247
Wunderlich, E., Wielebinski, R., & Klein, U. 1987, A&AS, 69, 487